**Springer Theses**
Recognizing Outstanding Ph.D. Research

Jie Ren

# Secondary Instabilities of Görtler Vortices in High-Speed Boundary Layers

## Mechanisms and Flow Control on Laminar-Turbulent Transition

Springer

## Springer Theses

Recognizing Outstanding Ph.D. Research

## Aims and Scope

The series "Springer Theses" brings together a selection of the very best Ph.D. theses from around the world and across the physical sciences. Nominated and endorsed by two recognized specialists, each published volume has been selected for its scientific excellence and the high impact of its contents for the pertinent field of research. For greater accessibility to non-specialists, the published versions include an extended introduction, as well as a foreword by the student's supervisor explaining the special relevance of the work for the field. As a whole, the series will provide a valuable resource both for newcomers to the research fields described, and for other scientists seeking detailed background information on special questions. Finally, it provides an accredited documentation of the valuable contributions made by today's younger generation of scientists.

## Theses are accepted into the series by invited nomination only and must fulfill all of the following criteria

- They must be written in good English.
- The topic should fall within the confines of Chemistry, Physics, Earth Sciences, Engineering and related interdisciplinary fields such as Materials, Nanoscience, Chemical Engineering, Complex Systems and Biophysics.
- The work reported in the thesis must represent a significant scientific advance.
- If the thesis includes previously published material, permission to reproduce this must be gained from the respective copyright holder.
- They must have been examined and passed during the 12 months prior to nomination.
- Each thesis should include a foreword by the supervisor outlining the significance of its content.
- The theses should have a clearly defined structure including an introduction accessible to scientists not expert in that particular field.

More information about this series at http://www.springer.com/series/8790

Jie Ren

# Secondary Instabilities of Görtler Vortices in High-Speed Boundary Layers

## Mechanisms and Flow Control on Laminar-Turbulent Transition

Doctoral Thesis accepted by
Tsinghua University, Beijing, China

Springer

*Author*
Dr. Jie Ren
Tsinghua University
Beijing
China

*Supervisor*
Prof. Song Fu
Tsinghua University
Beijing
China

ISSN 2190-5053 ISSN 2190-5061 (electronic)
Springer Theses
ISBN 978-981-10-6831-7 ISBN 978-981-10-6832-4 (eBook)
https://doi.org/10.1007/978-981-10-6832-4

Library of Congress Control Number: 2017955639



Printed on acid-free paper

This Springer imprint is published by Springer Nature
The registered company is Springer Nature Singapore Pte Ltd.
The registered company address is: 152 Beach Road, #21-01/04 Gateway East, Singapore 189721, Singapore

*To Chunyan*

# Supervisor's Foreword

To many supervisors of Ph.D. students, the most fortunate is having a talented, capable, and productive student. I certainly feel fortunate and happy to have Jie Ren as one of my Ph.D. students from September 2011 to December 2015. Jie devoted himself totally to his research, very focused. In fact, he came to our laboratory LAST in the summer at the end of his second year in undergraduate study. I quickly noticed Jie's difference from many others in his quality of study. Jie's diligence finally rewarded him in his Ph.D. work. He finished his Ph.D. degree in shortest time in my group in recent years and published five journal articles in JFM, PoF, FTaC, and SCPMA and many conference papers. He received Best Ph.D. Thesis Award at our university and Top Ph.D. Thesis Award from the Chinese Society of Theoretical and Applied Mechanics.

Dr. Jie Ren started his research on flow instability in hypersonic flows. In particular, he was concerned with the high-speed flows over a concave surface or a surface with a compression angle. Thus, Jie is first led to focus on the problem of Görtler instability. This is the key to flow transition when concave surface is present. He further studied the spectrum, nonlinear development, and secondary instabilities of Görtler vortices. For the first time, he did a comprehensive study on such problems in hypersonic flows. Görtler instability is the primary phenomenon to the understanding of flow transition on hypersonic vehicles. With a clear view of Görtler vortices, Jie extended his study to the control of the hypersonic flow transition. He showed that finite-amplitude streaks could be used to stabilize the flow as well as to the design of roughness elements to enhance flow transition. His study created new ideas to the manipulation of hypersonic flows.

Dr. Jie Ren's book illustrated clearly the mathematics and flow physics of the Görtler instability at hypersonic flow conditions. The book started from an introduction of the current understanding of instabilities in hypersonic boundary layers. Of which, the up-to-date research on the spatial development and secondary instability of Görtler vortices were reviewed. In Chap. 2, Jie shared with the readers a complete formulation of the stability equation (LSE, PSE, the adjoint equations) and the related numerical methods. In the chapters that follow, the readers will read

the interesting stories on linear instability, secondary instability of Görtler vortices, and the stabilization of the hypersonic boundary layer with finite-amplitude streaks.

This book provides thus not only Dr. Jie Ren's research, but it is also an excellent presentation of the knowledge of flow transition at hypersonic speed. I recommend this book to related researchers and graduate students also for its writing style in simple and clear English.

Beijing, China
September 2017

Prof. Song Fu

## Parts of this thesis have been published in the following articles:

Ren, J., Fu, S., & Hanifi, A. (2016). Stabilization of the hypersonic boundary layer by finite-amplitude streaks. Physics of Fluids, 28(2), 024110.

Ren, J., & Fu, S. (2015). Secondary instabilities of Görtler vortices in high-speed boundary layer flows. Journal of Fluid Mechanics, 781, 388–421.

Ren, J., & Fu, S. (2015). Study of the discrete spectrum in a Mach 4.5 Görtler flow. Flow, Turbulence and Combustion, 94(2), 339–357.

Ren, J., & Fu, S. (2014). Competition of the multiple Görtler modes in hypersonic boundary layer flows. Science China Physics, Mechanics and Astronomy, 57(6), 1178–1193.

Ren, J., & Fu, S. (2014). Floquet analysis of fundamental, subharmonic and detuned secondary instabilities of Görtler vortices. Science China Physics, Mechanics and Astronomy, 57(3), 555–561.

# Preface

*spirits of independence, thoughts of freedom*

The study dedicates to the understanding and controlling of flow transition from mild laminar to fully turbulent flows at high speed. This is the necessary condition and critically important to the beginning of an incredible era when hypersonic cruise vehicles become available for humanity.

This study, consisting of three major parts, first reveals the mechanism of the Görtler instability, and then a comprehensive investigation of the secondary instability is performed. With the understanding of Görtler vortices, they are used to control flow transition. Together with the Klebanoff mode (as a result of optimal disturbances), the study showed that both low-speed and high-speed flows can be either stabilized (suppress transition) or destabilized (promote transition) with finite-amplitude Klebanoff mode or Görtler vortices.

Beijing, China Dr. Jie Ren

# Acknowledgements

I want to express my greatest gratitude to my supervisor Prof. Song Fu for his dedication, kind guidance, and generous support. I feel lucky to have the chance to start working with Prof. Fu in the summer of 2009 when I was then a second-year undergraduate. From the study on "car aerodynamic" at that time to the present Ph.D. thesis, Prof. Fu has devoted a lot. His insights and encouragement instilled a constant source of inspiration in me.

I am very grateful to Dr. Guoliang Xu (China Aerodynamics Research and Development Center) and Dr. Jianxin Liu (Tianjin University) for their guidance and discussion when I started working on this exciting topic.

I am very thankful to the LAST group (Laboratory for Advanced Simulation of Turbulence). Thanks to Prof. Qibing Li, and I really appreciate the range of our conversations. Thanks to Prof. Haixin Chen, Zhixiang Xiao, Yufei Zhang, and Liang Wang.

Thanks to all the "LASTers" with whom I worked, discussed, learned, and played with during the past years, and they are Jingbo Huang, Ke Shi, Ming Zhao, Lianghua Xiao, Zhiwei Duan, Yuan Xue, Zhe Jiao, Shuang Tan, Ruyun Hu, Siya Jiang, Zhefu Wang, Doudou Ye, Liying Li, Youcheng Xi, and Yifei Xue.

I want to express my gratitude to Prof. Ardeshir Hanifi, who is my supervisor when I became a joint Ph.D. student in KTH mechanics. Ardeshir provided me not only part of the funding support but also great inspiration. His optimism and hearty laughter are definitely my precious memories in Linné Flow Centre.

A special thank goes to Prof. Shia-hui Peng, who is much obliged for the care and hospitality during my stay in Sweden.

I also want to thank Prof. Dan Henningson for letting me be a member of his group. Thanks to Luca Brandt and Shervin Bagheri for fruitful discussions. I am very grateful to Alessandro Bottaro and Jan Pralits of Università di Genova for the discussions on adjoint equations.

I want to thank the group members in KTH mechanics—Alexandra, Armin, Carolina, Chenyang, Clio, Iman, Jacopo, Lim, Mattias, Mehdi, Nicolas, Nima, Wei, Walter, Yukinori—for creating an enjoyable and friendly atmosphere.

Financial supports by the National Natural Science Foundation of China (Grant Nos. 11272183, 11572176, 11602127), China Scholarship Council (No. 201406210236), and China Postdoctoral Science Foundation (Nos. 2016M590091, 2017T100067) are gratefully acknowledged.

*To my parents*

Delft, the Netherlands Dr. Jie Ren
September 2017

# Contents

# Nomenclature

## Abbreviations

| | |
|---|---|
| DNS | Direct Numerical Simulation |
| G-type streak | Streaks generated by Görtler modes |
| K-type streak | Streaks generated by Klebanoff modes |
| LST | Linear Stability Theory |
| Mode F | Fast mode (stem from the fast acoustic waves) |
| Mode S | Slow mode (stem from the slow acoustic waves) |
| Mode S-I | Sinuous-I mode of secondary instability of Görtler vortices |
| Mode S-II | Sinuous-II mode of secondary instability of Görtler vortices |
| Mode T | Trapped-layer (temperature-adjustment-layer) Görtler mode |
| Mode V | Varicose mode of secondary instability of Görtler vortices |
| Mode W | Wall-layer Görtler mode |
| MVG | Miniature Vortex Generator |
| N-S | Navier-Stokes |
| PSE | Parabolized Stability Equations |
| T-S | Tollmien-Schlichting |

## Subscript, Superscript, Overstrike, Other Notations

| | |
|---|---|
| $\|\|q\|\|_E$ | Energy norm, $q$ denotes any physical quantities (same as below) |
| $q_\infty$ | Freestream quantities |
| $q_w$ | Quantities at the wall |
| $q_0$ | Quantities at $x = x_0$ |
| $q^*$ | Dimensional quantities |
| $c.c.$ | Complex conjugate |

| | |
|---|---|
| $q^\dagger$ | Complex conjugate |
| $\bar{q}$ | Average (temporal or spatial) of physical quantities |
| $\tilde{q}$ | Perturbation in physical space |
| $\hat{q}$ | Perturbation in spectral space |

## Dimensionless Quantities

| | |
|---|---|
| $Re$ | Reynolds number |
| $Pr$ | Prandtl number |
| $Ma$ | Mach number |
| $G$ | Görtler number |

## Geometry and Flow Parameters

| | |
|---|---|
| $x, y, z$ | Coordinate in the streamwise, normal to the wall and spanwise directions (orthogonal curvilinear coordinates) |
| $h_1$, $h_2$, $h_3$ | Lamé coefficients in $x$, $y$, and $z$ |
| $k$ | Local streamwise curvature |
| $u, v, w$ | Velocity in $x$, $y$, and $z$ |
| $c$ | Speed of sound |
| $t$ | Time |
| $\rho$, $T$, $p$ | Density, temperature, and pressure of the fluid |
| $\mu$, $\nu$, $\kappa$ | Dynamic viscosity, kinetic viscosity, and coefficient of thermal conductivity |
| $R_{air}$ | Specific gas constant for air |
| $\gamma$ | Specific heat ratio |
| $\delta$ | Boundary layer thickness scale $\delta = \sqrt{\nu^* x^* / U_\infty^*}$ |

## Perturbations

| | |
|---|---|
| $\tilde{\boldsymbol{q}}$ | Perturbation vector $\tilde{\boldsymbol{q}} = (\tilde{\rho}, \tilde{u}, \tilde{v}, \tilde{w}, \tilde{T})^T$ |
| $\tilde{\boldsymbol{p}}$ | Adjoint of the perturbation vector |
| $\alpha$, $\beta$, $\omega$ | Streamwise wavenumber, spanwise wavenumber, and angular frequency of the perturbation |
| $\lambda$ | Spanwise wavelength of the perturbation |
| $B$, $F$ | Global spanwise wavenumber and frequency of the perturbation |
| $J$ | Objective function of the optimal perturbations |

# Chapter 1
# Introduction

## 1.1 Backgroud

The flow transition has a critical impact on aerodynamic heating, drag, and vehicle operation because turbulent flows generate tremendously higher friction and heating to the vehicles than laminar ones. It also affects engine performance and operability, as well as the structure and weight of the vehicles.

The success of transition prediction and control relies on a fundamental understanding of the relevant physical mechanisms leading to transition. Despite considerable efforts in experimental, theoretical, and numerical studies, many critical physical mechanisms underlying the hypersonic boundary-layer transition are still poorly understood. Actually, the Görtler instability has been used to promote flow transition on hypersonic vehicles. However, how Görtler instabilities get excited and how they evolve in hypersonic flows remain open to be answered.

## 1.2 Receptivity and Spectrum of Hypersonic Boundary Layers

The linear stability analysis on the high-speed boundary layers by Mack [1, 2] led to a remarkable extension of the hydrodynamic stability theory to compressible boundary layer flows. Mack showed the existence of the multiple stability modes in the compressible boundary layer flows. The higher modes belong to the trapped acoustic waves with higher frequencies. The second mode was known to be the most dangerous one at hypersonic boundary layers at, for instance, $Ma \approx 5$. The Mack modes did not however coincide exactly with the normal modes proposed by Fedorov and Tumin [3]. In fact, the spectrum changed significantly when viscous effect was considered. The causes of the discrete modes emphasized with the normal mode analysis are now favored by a number of researchers [4, 5].



J. Ren, *Secondary Instabilities of Görtler Vortices in High-Speed Boundary Layers*, Springer Theses, https://doi.org/10.1007/978-981-10-6832-4_1

The boundary layer flow is regarded as the local stability problem when the parallel flow assumption can be adopted. Considering the disturbances in a steady basic flow, the linear stability theory (LST) gives a well-accepted and compact description of the possible disturbances in the boundary layer. Generally, a Global (BiGlobal or TriGlobal) [6, 7] or Local stability problem [8] may be formulated in accordance with the number of dimensions of the prescribed basic flow. The LST, in a different aspect, helps to build the transition model for engineering applications [9].

For the natural transition in a low disturbance environment, the receptivity is the process through which the disturbances obtain the modal shapes. Research on the receptivity problem has received increasing attention due to its practical importance. The various types of the external disturbances include freestream turbulence (FST) [10–13], surface roughness [14], solid particulates [15], wall vibrations [16], etc. Recent reviews can be found in Fedorov [4] and Zhong and Wang [5]. The FST consists of the (fast and slow) acoustic, vortical and entropy modes [17]. How these external disturbances affecting the curved high-speed boundary layer is to be studied in Sect. 3.1.

The normal mode analysis, as presented by Ma and Zhong [18], gives the phase velocity and the growth rate of the discrete normal modes as functions of the angular frequency $\omega$ shown in Fig. 1.1. Three synchronization regions could be summarized in the following manner [4]:

(1) The fast and slow acoustic waves of the continuous spectrum give rise to the discrete fast and slow modes (mode F and mode S) respectively in the leading edge;

(2) The mode F is then synchronized with the entropy/vorticity waves with a discontinuity in the growth rate [19];

(3) The unstable second mode finally appears as a result of the synchronization between the mode F and the mode S.

In connection with Mack's terminology, the first mode is actually the unstable mode S while the second and higher modes belong to different sections of the mode F or mode S depending on the pattern of the branching. When the oblique mode (3-D disturbances) is considered [18], the increase in the spanwise wavenumber $\beta$ (or the wave angle $\psi = \arctan(\beta/\alpha_r)$) leads to the decrease of the growth rate of the Mack mode. It is thus consistent with Mack's analysis that the most unstable second mode corresponds to the 2-D disturbances.

As shown in Fig. 1.1, the constant phase velocity $c = 1 + 1/Ma$ represents the fast acoustic wave, $c = 1$ the vorticity/entropy wave and $c = 1 - 1/Ma$ the slow acoustic wave. A series of discrete modes arise from the continuous spectrum of the fast acoustic wave, i.e. mode $F^{(1)}$, $F^{(2)}$, $F^{(3)}$ etc. The second and higher Mack modes correspond to the synchronization between these modes and the mode S. To make a distinction, the subscripts $+$ and $-$ refer to the F modes which have or have not, respectively, synchronized with the continuous spectrum of the vorticity/entropy wave [3]. The synchronization between the mode F and the vorticity/entropy waves is studied in [20]. In this region of synchronization, as shown in Figs. 1.2 and 1.3, a discontinuity of the growth rate is observed and the boundary layer is sensitive to thermal and freestream turbulence.

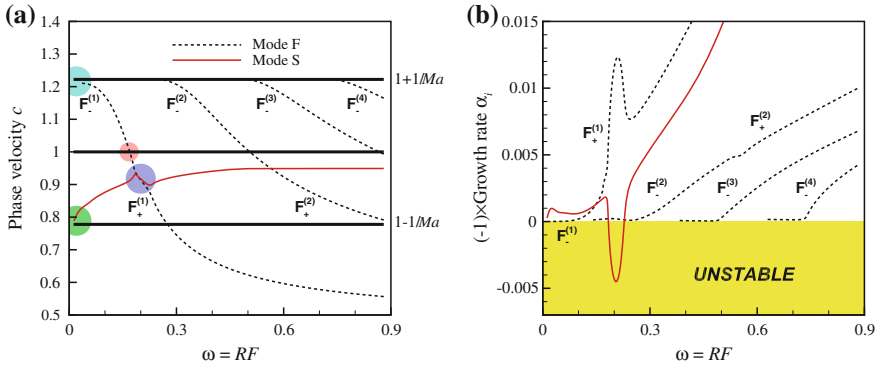


**Fig. 1.1** The phase velocity **a** and growth rate **b** of the discrete spectrum as a function of the angular frequency $\omega$; $M = 4.5$, $T_\infty^* = 65.15K$, $Pr = 0.72$, $F = 2.2 \times 10^{-4}$ and $Re \in [10, 4000]$

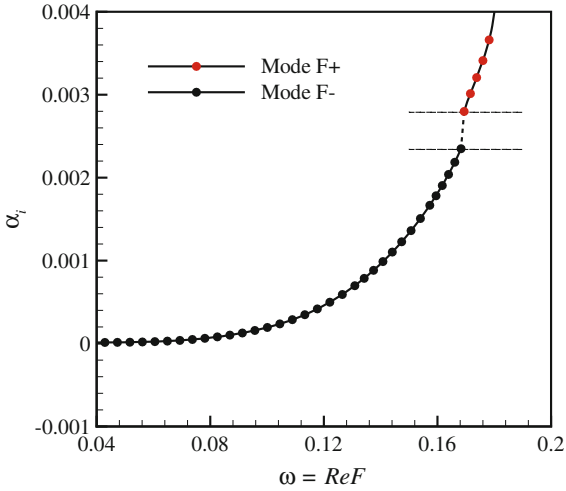


**Fig. 1.2** Growth rate of the Mode F when synchronizing with the vorticity/entropy waves where the phase velocity is around 1.0

Different branching patterns of the discrete spectrum are shown in Gushchin and Fedorov [21]. When the mode F is synchronized with the mode S, a minor variation in the basic flow may result in a totally different pattern of branching. Besides, the normal mode analysis leads to singularity in the vicinity of the branching points [3]. The evolution of the velocity disturbance of $\hat{u}_r$ is given in Fig. 1.4 where eleven profiles are uniformly distributed within $\omega \in [0.155, 0.265]$. The profiles are normalized so that the maximum values equal to one. The synchronization lies in the region $\omega \in [0.183, 0.227]$ and are labeled in the top of the figure. Abrupt changes are observed at the start and the end of the synchronization region for mode F and mode S respectively. This is an evidence of the singularity in the normal mode formulation on both ends of the synchronization. The singularity behavior disappears when the

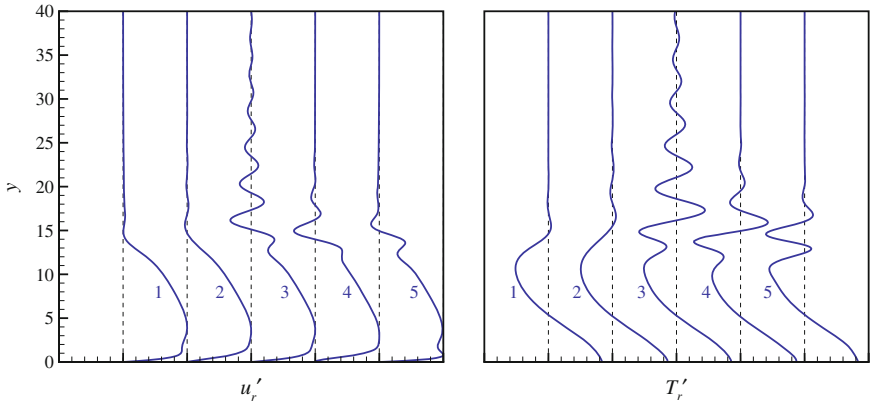


**Fig. 1.3** Evolution of the streamwise velocity disturbance $\hat{u}_r$ and temperature perturbation $\hat{T}_r$ for Mode F aroud phase velocity $c = 1.0$ (labeled 3 in the plots)

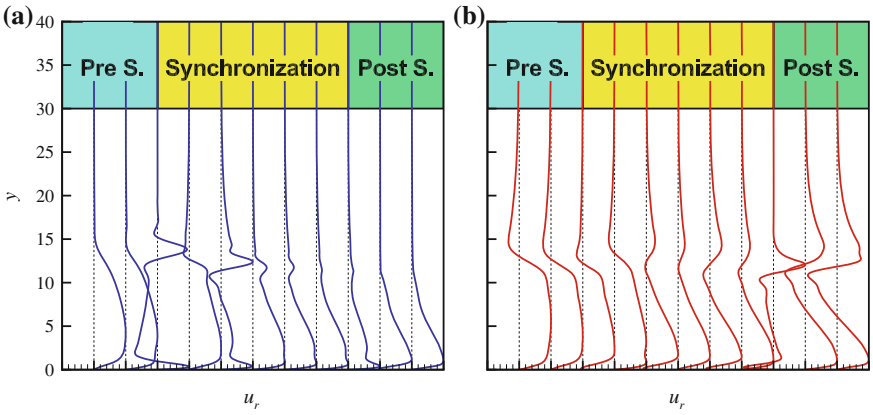


**Fig. 1.4** Evolution of the streamwise velocity disturbance $\hat{u}_r$ for **a** Mode F and **b** Mode S; $\omega \in [0.155, 0.265]$

Parabolized Stability Equation (PSE) approach is applied and the results are shown to be consistent with the Direct Numerical Simulation (DNS) results [22].

## 1.3 Görtler Instability

Görtler instability [23], known as the centrifugal instability of a boundary layer over a concave wall, arises due to the imbalance between the centrifugal force and the wall-normal pressure gradient. Streamwise-oriented, counter-rotating vortices (Görtler vortices) are consequently generated, maintained and can be significantly intensified

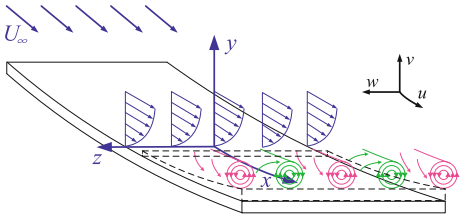


**Fig. 1.5** Sketch of the counter-rotating Görtler vortices encountered on a slightly concave wall. The orthogonal curvilinear coordinates $x$, $y$ and $z$ denote streamwise, wall-normal and spanwise directions. Velocity components $u$, $v$ and $w$ are defined in the above directions. The near wall area (dashed lines) indicates the undisturbed region due to the dominance of trapped-layer modes (mode T) in hypersonic boundary layers

downstream promoting flow transition. Most of early studies were conducted within the framework of incompressible flows (see Reviews by Herbert [24], Hall [25], Floryan [26] and Saric [27]).

Görtler instability can be studied in the coordinates defined in Fig. 1.5, axes $x$, $y$ and $z$ are along streamwise, wall-normal and spanwise directions respectively. The corresponding lame coefficients are $h_1 = 1 + ky$, $h_2 = h_3 = 1$ with $k$ representing the streamwise curvature (negative).

Concerning the receptivity problem (see [25, 28] for early reviews), Görtler vortices can be excited through surface roughness [29–32] or/and FST [31–33]. Recent DNS study indicates that zero or low frequency free stream vortices most effectively excite the Görtler vortices [32].

Görtler instabilities have been formerly studied with normal mode analysis locally in order to obtain the so-called neutral curve [24] (see Fig. 1.6). The parallel flow assumption was often adopted. In fact, Görtler instabilities exhibit crucial differences compared to conventional TollmienSchlichting (T-S) waves. Görtler instability is governed by parabolic equations [25]. The initial conditions and the non-parallel nature of the boundary layer can exert a critical influence. Therefore, a unique neutral curve is no longer tenable [34, 35]. The recent study by Wu et.al. [33] has fully uncovered the different regimes of the excitation and spatial development of Görtler vortices. Local normal mode analysis is mathematically justified when the streamwise coordinate is large enough (where the inviscid regime is reached). From a numerical point of view, the eigenvalue problem (EVP) is valid only when the Görtler number $G = Re\sqrt{\delta_x^*/R^*}$ is large. Here $R^*$ is the local radius of curvature and $x^*$ is the streamwise coordinate. Typically, $G > 7$ is satisfactory for applying the normal mode approach [36]. Discussions on the validity of the local eigenvalue problem can also be found in Day et.al. [37] and Goulpié [38]. Similar restrictions exist for compressible flows with $O(1)$ $Ma$ number [39, 40].

For hypersonic Görtler flows, the most significant flow feature is the existence of the temperature adjustment layer near the upper edge of the boundary layer which gives rise to the trapped-layer mode (mode T, disturbances rest in the layer near the upper edge of boundary layer) [41, 42]. This mode becomes the most dangerous

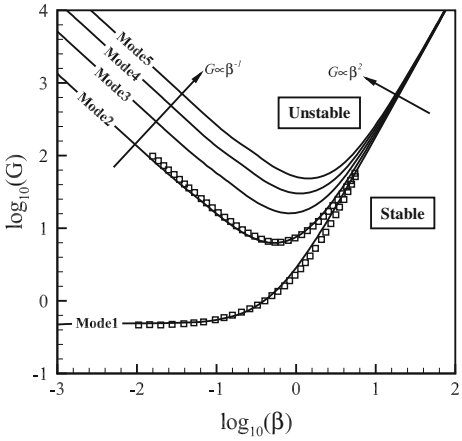


**Fig. 1.6** "Neutral curve" of the multiple Görtler modes in incompressible flows. A critical Görtler number (hereafter referred to as G) of 0.4638 is located at the quasi-zero spanwise wavenumber

when the *Ma* number is larger than a critical value, *e.g.* $Ma \geq 4$, roughly. The mode T can also intersect with the conventional wall-layer mode (mode W, disturbances exist in the layer close to the wall) at very large *Re* numbers. The crossover on the growth rate between the two modes has been studied with the asymptotic [43] and the local and marching methods [44].

Experimental studies of Görtler vortices in high-speed flows are scarce. The $Ma = 7$ experiment by Luca et.al. [45] demonstrated the generation of Görtler vortices from spanwise periodic temperature variations. The wavelength was found to maintain a constant value along the streamwise direction. However, neither the baseflow nor perturbation quantities were reported in the experiment. The other experiments were conducted over a compression ramp [46, 47]. Due to the concave curvature of the streamlines in the region of the flow separation, Görtler mechanism is engaged. On the other hand, properly handling Görtler instability is of vital importance in the design of high-speed wind-tunnel nozzles [48–50].

On the other hand, the unsteady Görtler mode has a smaller growth rate. Together with the high turbulence intensity, unsteady Görtler vortices are responsible for the transition in turbomachinery flows, *e.g.* over the turbine blades [33, 51]. Recently, Boiko et.al. [52, 53] excited the unsteady Görtler vortices in a low-turbulence subsonic wind-tunnel. Further numerical study with both the local and nonlocal analysis showed quantitative agreement with the experiment. However, the cause of the unsteady Görtler vortices in high-speed flows is far from well understood.

## 1.4 G–Type/K–Type Streaks and Their Effects on Flow Transition

Görtler vortices (G-type streaks) by itself, does not lead to the flow transition. Instead, the low- and high- speed streaks are produced and enhanced by the long-persisting streamwise counter-rotating vortices (termed Görtler vortices or Görtler rolls). Besides the Görtler flow, streaks can form in a laminar boundary layer in other situations through the *lift-up* mechanism [54–56]. For instance, streaks developed due to the transient growth of optimal disturbances (Klebanoff modes, K-type streaks) [57–59] which are more roundly analyzed with the consideration of receptivity to free-stream turbulence (FST) [60, 61] and wake flows past proper sized roughness elements [62–64]. Counterparts of the above mechanisms were observed in compressible flows as well [65–68]. These flows thus share many similarities. The secondary instability of streaks has been recognized as a key factor leading the boundary layer to transition. The subsequent breakdown process is observed to proceed rather rapidly [69]. Studying the secondary instability is thus important to understand the physical mechanism of the transition process. A number of numerical investigations [70–77] were carried out with the parameters taken from the experiment [69]. Recognizing the most dangerous secondary mode is of fundamental importance as it determines both the scenario and location of transition. For incompressible Görtler flow, the sinuous and varicose modes are found [71, 72] and analyzed with energy balancing mechanisms [73–75]. Schrader et.al. [32] performed the first spatial DNS for a Görtler flow including the experiment conditions of [78, 79] for incompressible flows. In their breakdown process reported, both the sinuous and varicose modes have been observed. It had been found that the sinuous mode appeared first and required a lower amplitude of the streak [77, 80] while varicose modes were stronger for large wavelengths of Görtler vortices [76]. This was later validated in the experiment for the secondary instability of streaks along a flat plate [81]. In the study of Li and Malik [76], the subharmonic type was also highlighted as they had comparable growth rate to the fundamental counterparts. Among these studies, a particular sinuous mode had been missed out. This mode is sinuous in nature but its disturbances are distributed near the *stem* of the *mushroom* [82]. In the wake of an isolated roughness element, this type of mode (but not the most dangerous) was also reported [68]. In the current study, we shall show this mode can have the largest growth rate and therefore is responsible for the sinuous breakdown under certain conditions.

Discussions on the secondary instability of Görtler vortices in compressible flows can be found in [41, 83, 84]. In the numerical study by Whang and Zhong [83], a $Ma = 15$ flow with a concave surface was simulated with direct numerical simulation (DNS). The varicose mode which develops into the horseshoe vortex was found to be dominant over the sinuous mode. In the $Ma = 6$ study by Li et.al. [84], however, the most dangerous mode was demonstrated to be the sinuous mode. Besides the secondary instability of Görtler vortices, the other routes towards transition, *e.g.* the Görtler - Mack mode interactions, were also explored in [84].

Besides promoting flow transition, recent studies on finite-amplitude streaks have provided a promising control methodology to attenuate the Tollmien-Schlichting (T-S) waves thereby delaying or even suppressing flow transition [85].

Prior to the onset of secondary instabilities [86], T-S waves can, to a remarkable extent, be stabilized. The direct numerical simulations (DNS) by Cossu and Brandt [87, 88] showed that the T-S waves can be effectively stabilized by optimal streaks. Here, "optimal" stands for the disturbance which experience maximum energy growth measured in a prescribed spatial or temporal range. In the Blasius boundary layer, as investigated by Andersson et.al. [58] and Luchini [59], the *Re*-independent optimal parameters are spanwise wavenumber $\beta_{opt} = 0.45$ and frequency $\omega_{opt} = 0$. Increase in the amplitude of the streaks shows a stronger effect of stabilization. This is due to the modification to the mean flow caused by the nonlinear development of streaks. The optimal streaks, nevertheless, are not necessarily "optimal" for the stabilization of T-S waves. [89].

The experiments performed by Fransson and co-workers successfully materialized the idea of passive control with circular roughness elements [90–92] and miniature vortex generators (MVGs) [93–96]. The threshold streak amplitude is substantially increased from 12 to 32% with the latter. The elaborated streaky flow excited in the boundary layer (*e.g.* with aforementioned MVGs) suffers from considerable viscous dissipation. To prevent the rapid decay of streaks, multiple MVGs in the streamwise direction could be necessary [93]; The control was also shown to be robust when subjected to random noise. On the other hand, some disadvantages are reported for MVG/roughness elements. (1) Under off-design flow conditions, the MVGs hardly play a positive role in maintaining laminar flows; (2) When the flow is exposed to FST, this passive control could fail because of the interactions between the MVGs and FST. Recently, free-stream vortices are proved to be able to generate effective streaks [97]. This provides a new strategy through which the above weakness may be overcome.

Apart from the two-dimensional (2-D) disturbances in a flat-plate boundary layer, streaks can stabilize the oblique waves [89, 98] as well. Similar approach for transition control in three-dimensional boundary-layer flow over swept-wings has been studied intensively by Saric et.al. [99, 100]. Here, the sub-critical crossflow modes are excited by the micron-sized roughness elements, which through their nonlinear interactions with the mean flow weakened the critical crossflow mode as well as its secondary instabilities [101].

## 1.5 Thesis Outline and Motivation

**In Chapter** 2, the numerical methods used in this thesis are introduced.

**In Chapter** 3, stability of the concave boundary layer is studied with linear stability theory. In particular, attention is paid for small *Re* number (mode synchronization) and very large *Re* number (mode competition) regimes. The branching of the discrete spectrum motivated the present work to further consider both the effect of the 3-D

disturbances and the streamwise curvature in an attempt to highlight the receptivity process of the unsteady and quasi-steady Görtler vortices. On the other hand, to clarify the behavior of the multiple Görtler modes, local and marching methods are adopted to study the competition between the trapped-layer-mode (Mode T) and wall-layer-mode (Mode W).

**In Chapter** 4, the secondary instabilities of Görtler vortices are investigated. By taking a broad view of existing studies in compressible Görtler flows, however, many aspects relating to the secondary instabilities of Görtler vortices remain unclear. For example, what is the effect of increasing *Ma* number on the secondary instability with Mode T being the governing mode? How is the neutral condition found in [80] influenced by the Mach number? Is the relationship between the growth rate of the varicose/sinuous mode and the basic wavelength of Görtler vortices [76] still valid in compressible flows? Should the subharmonic and detuned secondary instabilities be responsible for the transition process? These problems are investigated comprehensively in this chapter.

**In Chapter** 5, the stabilization of boundary layer with finite amplitude streaks is extended to hypersonic flows. In fact, most of previous studies performed on this topic are confined in incompressible flows. This chapter will show that both the first mode and Mack's second mode can be effectually stabilized.

**In Chapter** 6, the thesis is concluded.

## References

1. Mack, L.M.: Linear stability theory and the problem of supersonic boundary-layer transition. AIAA J **13**(3), 278–289 (1975)
2. Mack, L.M.: Boundary-layer linear stability theory. AGARD Report No 709 , Special Course on Stability and Transition of Laminar Flows (1984)
3. Federov, A., Tumin, A.: High-speed boundary-layer instability: Old terminology and a new framework. AIAA J. **49**(8), 1647–1657 (2011)
4. Fedorov, A.: Transition and stability of high-speed boundary layers. Annu. Rev. Fluid Mech. **43**, 79–95 (2011). doi:10.1146/annurev-fluid-122109-160750
5. Zhong, X., Wang, X.: Direct numerical simulation on the receptivity, instability, and transition of hypersonic boundary layers. Ann. Rev. Fluid Mech. **44**, 527–561 (2012). doi:10.1146/annurev-fluid-120710-101208
6. Theofilis, V.: Advances in global linear instability analysis of nonparallel and three-dimensional flows. Prog. Aerosp. Sci. **39**(4), 249–315 (2003). doi:10.1016/S0376-0421(02)00030-1, http://www.sciencedirect.com/science/article/pii/S0376042102000301
7. Theofilis, V.: Global linear instability. Ann. Rev. Fluid Mech. **43**, 319–352 (2011). doi:10.1146/annurev-fluid-122109-160705, http://www.annualreviews.org/doi/abs/10.1146/annurev-fluid-122109-160705
8. Reed, H.L., Saric, W.S., Arnal, D.: Linear stability theory applied to boundary layers. Annual Review of Fluid Mechanics **28**, 389–428 (1996). doi:10.1146/annurev.fl.28.010196.002133. http://www.annualreviews.org/doi/abs/10.1146/annurev.fl.28.010196.002133
9. Fu, S., Wang, L.: Rans modeling of high-speed aerodynamic flow transition with consideration of stability theory. Prog. Aerosp Sci. **58**, 36–59 (2013). doi:10.1016/j.paerosci.2012.08.004, http://www.sciencedirect.com/science/article/pii/S0376042112000851

10. Ma, Y., Zhong, X.: Receptivity of a supersonic boundary layer over a flat plate. Part 2. Receptivity to free-stream sound. J. Fluid Mech. **488**, 79–121 (2003). doi:10.1017/S0022112003004798, http://journals.cambridge.org/article_S0022112003004798
11. Ma, Y., Zhong, X.: Receptivity of a supersonic boundary layer over a flat plate. part 3. effects of different types of free-stream disturbances. J. Fluid Mech. **532**, 63–109 (2005). doi:10.1017/S0022112005003836, http://journals.cambridge.org/article_S0022112005003836
12. Fedorov, A.V.: Receptivity of a high-speed boundary layer to acoustic disturbances. J. Fluid Mech. **491** 101–129 (2003). doi:10.1017/S0022112003005263, http://journals.cambridge.org/article_S0022112003005263
13. Fedorov, A.V., Ryzhov, A.A., Soudakov, V.G., Utyuzhnikov, S.V.: Receptivity of a high-speed boundary layer to temperature spottiness. J. Fluid Mech. **722** 533–553 (2013). doi:10.1017/jfm.2013.111, http://journals.cambridge.org/article_S0022112013001110
14. Tempelmann, D., Schrader, L.U., Hanifi, A., Brandt, L., Henningson, D.S.: Swept wing boundary-layer receptivity to localized surface roughness. J. Fluid Mech. **711**, 516–544 (2012). doi:10.1017/jfm.2012.405, http://journals.cambridge.org/article_S0022112012004053
15. Fedorov, A.V.: Receptivity of a supersonic boundary layer to solid particulates. J. Fluid Mech. **737**, 105–131 (2013). doi:10.1017/jfm.2013.564, http://journals.cambridge.org/article_S0022112013005648
16. Ruban, A.I., Bernots, T., Pryce, D.: Receptivity of the boundary layer to vibrations of the wing surface. J. Fluid Mech. **723** 480–528 (2013). doi:10.1017/jfm.2013.119, http://journals.cambridge.org/article_S0022112013001195
17. Kovasznay, L.S.G.: Turbulence in supersonic flow. J. Aeronaut. Sci. **20**(10), 657–674 (1953)
18. Ma, Y., Zhong, X.: Receptivity of a supersonic boundary layer over a flat plate. Part 1. Wave structures and interactions. J. Fluid Mech. **488**, 31–78 (2003). doi:10.1017/S0022112003004786, http://journals.cambridge.org/article_S0022112003004786
19. Fedorov, A.V., Khokhlov, A.P.: Prehistory of instability in a hypersonic boundary layer. Theor. Comput. Fluid Dyn. **14**(6), 359–375 (2001). doi:10.1007/s001620100038, http://dx.doi.org/10.1007/s001620100038
20. Federov, A., Tumin, A.: Initial-value problem for hypersonic boundary-layer flows. AIAA J. **41**(3), 379–389 (2003)
21. Gushchin, V., Fedorov, A.: Excitation and development of unstable disturbances in a supersonic boundary layer. Fluid Dyn. **25**(3), 344–352 (1990). doi:10.1007/BF01049814, http://dx.doi.org/10.1007/BF01049814
22. Lifshitz, Y., Degani, D., Tumin, A.: Study of discrete modes branching in high-speed boundary layers. AIAA J. **50**(10), 2202–2210 (2012)
23. Görtler, H.: Über eine dreidimensionale instabilität laminarer grenzschichten an konkaven wänden. Ges. D. Wiss. Göttingen, Nachr **1**(2) (1940) (Translated as On the three-dimensional instability of laminar boundary layers on concave walls. NACA TM 1375, 1954)
24. Herbert, T.: On the stability of the boundary layer along a concave wall. Archiwum mechaniki stosowanej **28**(5–6), 1039–1055 (1976)
25. Hall, P.: Görtler vortices in growing boundary layers: the leading edge receptivity problem, linear growth and the nonlinear breakdown stage. Mathematika **37**, 151–189 (1990). doi:10.1112/S0025579300012894
26. Floryan, J.: On the Görtler instability of boundary layers. Prog. Aerosp. Sci. **28**(3), 235–271 (1991). doi:10.1016/0376-0421(91)90006-P
27. Saric, W.S.: Görtler vortices. Annu. Rev. Fluid Mech. **26**(1), 379–409 (1994). doi:10.1146/annurev.fl.26.010194.002115
28. Bassom, A.P., Seddougui, S.O.: Receptivity mechanisms for Görtler vortex modes. Theor. Comput. Fluid Dyn. **7**(5), 317–339 (1995). doi:10.1007/BF00312412
29. Denier, J.P., Hall, P., Seddougui, S.O.: On the receptivity problem for gortler vortices: Vortex motions induced by wall roughness. Philos. Trans. R. Soc. Lond. A: Math. Phys. Eng. Sci. **335**(1636), 51–85 (1991). doi:10.1098/rsta.1991.0036

30. Bassom, A.P., Hall, P.: The receptivity problem for O(1) wavelength gortler vortices. In: Proceedings of the Royal Society of London A: Mathematical, Physical and Engineering Sciences, vol. 446 no. 1928, pp. 499–516 (1994). doi:10.1098/rspa.1994.0117
31. Luchini, P., Bottaro, A.: Görtler vortices: a backward-in-time approach to the receptivity problem. J. Fluid Mech. **363**, 1–23 (1998). doi:10.1017/S0022112098008970
32. Schrader, L.u., Brandt, L., Zaki, T.A.: Receptivity, instability and breakdown of Görtler flow. J. Fluid Mech. **682**, 362–396 (2011). doi:10.1017/jfm.2011.229
33. Wu, X., Zhao, D., Luo, J.: Excitation of steady and unsteady Görtler vortices by free-stream vortical disturbances. J. Fluid Mech. **682**, 66–100 (2011). doi:10.1017/jfm.2011.224
34. Hall, P.: Taylor- Görtler vortices in fully developed or boundary-layer flows: linear theory. J. Fluid Mech. **124**, 475–494 (1982). doi:10.1017/S0022112082002596
35. Hall, P.: The linear development of Görtler vortices in growing boundary layers. J. Fluid Mech. **130**, 41–58 (1983). doi:10.1017/S0022112083000968
36. Bottaro, A., Luchini, P.: Görtler vortices: Are they amenable to local eigenvalue analysis? Eur. J. Mech. B/Fluids **18**(1), 47–65 (1999). doi:10.1016/S0997-7546(99)80005-3
37. Day, H.P., Herbert, T., Saric, W.S.: Comparing local and marching analysis of Görtler instability. AIAA J. **28**(6), 1010–1015 (1990)
38. Goulpié, P., Klingmann, B.G.B., Bottaro, A.: Görtler vortices in boundary layers with streamwise pressure gradient: Linear theory. Phys. Fluids **8**(2), 451–459 (1996). doi:10.1063/1.868799
39. Hall, P., Fu, Y.: On the Görtler vortex instability mechanism at hypersonic speeds. Theor. Comput. Fluid Dyn. **1**(3), 125–134 (1989). doi:10.1007/BF00417916
40. Spall, R.E., Malik, M.R.: Goertler vortices in supersonic and hypersonic boundary layers. Phys. Fluids A: Fluid Dyn. **1**(11), 1822–1835 (1989). doi:10.1063/1.857508
41. Fu, Y., Hall, P.: Nonlinear development and secondary instability of large-amplitude Görtler vortices in hypersonic boundary-layers. Euro. J. Mech. B-Fluids **11**(4), 465–510 (1992)
42. Fu, Y., Hall, P.: Effects of Görtler vortices, wall cooling and gas dissociation on the rayleigh instability in a hypersonic boundary layer. J. Fluid Mech. **247**, 503–525 (1993). doi:10.1017/S0022112093000540
43. Dando, A.H., Seddougui, S.O.: The compressible Görtler problem in two-dimensional boundary layers. IMA J. Appl. Math. **51**(1), 27–67 (1993). doi:10.1093/imamat/51.1.27
44. Ren, J., Fu, S.: Competition of the multiple Görtler modes in hypersonic boundary layer flows. Sci. China Phys. Mech. Astron. **57**(6), 1178–1193 (2014). doi:10.1007/s11433-014-5454-9
45. Luca, L., Cardone, G., Aymer de la Chevalerie, D., Fonteneau, A.: Goertler instability of a hypersonic boundary layer. Exp. Fluids **16**(1), 10–16 (1993). doi:10.1007/BF00188500
46. de la Chevalerie, D., Fonteneau, A., Luca, L.D., Cardone, G.: Görtler-type vortices in hypersonic flows: the ramp problem. Exp. Therm. Fluid Sci. **15**(2), 69–81 (1997). doi:10.1016/S0894-1777(97)00051-4
47. Schrijer, F.: Investigation of Görtler vortices in a hypersonic double compression ramp flow by means of infrared thermography. Quant. Infrared Thermogr. J. **7**(2), 201–215 (2010). doi:10.3166/qirt.7.201-215
48. Chen, F.J., Wilkinson, S.P., Beckwith, I.E.: Görtler instability and hypersonic quiet nozzle design. J. Spacecr. Rocket. **30**(2), 170–175 (1993)
49. Schneider, S.P.: Design of a mach-6 quiet-flow wind-tunnel nozzle using the e**n method for transition estimation. In: 36th AIAA Aerospace Sciences Meeting and Exhibit, AIAA-1998-0547 (1998)
50. Schneider, S.P.: Development of hypersonic quiet tunnels. J. Spacecr. Rocket. **45**(4), 641–664 (2008). doi:10.2514/1.34489
51. Volino, R.J., Simon, T.W.: Spectral measurements in transitional boundary layers on a concave wall under high and low free-stream turbulence conditions. J. Turbomach. **122**, 450–457 (2000)
52. Boiko, A., Ivanov, A., Kachanov, Y., Mischenko, D.: Quasi-steady and unsteady goertler vortices on concave wall: experiment and theory. In: J. Palma., A. Lopes (eds.) Advances in Turbulence XI, Springer Proceedings Physics, vol. 117, pp. 173–175. Springer, Berlin (2007). doi:10.1007/978-3-540-72604-3_54, http://dx.doi.org/10.1007/978-3-540-72604-3_54

53. Boiko, A., Ivanov, A., Kachanov, Y., Mischenko, D.: Steady and unsteady Görtler boundary-layer instability on concave wall. Euro. J. Mech. B/Fluids **29**(2), 61–83 (2010)
54. Landahl, M.T.: Wave breakdown and turbulence. SIAM J. Appl. Math. **28**(4), 735–756 (1975). doi:10.1137/0128061, http://dx.doi.org/10.1137/0128061
55. Landahl, M.T.: A note on an algebraic instability of inviscid parallel shear flows. J. Fluid Mech. **98**, 243–251 (1980). doi:10.1017/S0022112080000122, http://journals.cambridge.org/article_S0022112080000122
56. Ellingsen, T., Palm, E.: Stability of linear flow. Phys. Fluids (1958-1988) **18**(4), 487–488 (1975). doi:10.1063/1.861156
57. Hultgren, L.S., Gustavsson, L.H.: Algebraic growth of disturbances in a laminar boundary layer. Phys. Fluids (1958-1988) **24**(6), 1000–1004 (1981). doi:10.1063/1.863490
58. Andersson, P., Berggren, M., Henningson, D.S.: Optimal disturbances and bypass transition in boundary layers. Phys. Fluids **11**(1), 134–150 (1999). doi:10.1063/1.869908, http://scitation.aip.org/content/aip/journal/pof2/11/1/10.1063/1.869908
59. Luchini, P.: Reynolds-number-independent instability of the boundary layer over a flat surface: optimal perturbations. J. Fluid Mech. **404**, 289–309 (2000). doi:10.1017/S0022112099007259, http://journals.cambridge.org/article_S0022112099007259
60. Leib, S.J., Wundrow, D.W., Goldstein, M.E.: Effect of free-stream turbulence and other vortical disturbances on a laminar boundary layer. J. Fluid Mech. **380**, 169–203 (1999). doi:10.1017/S0022112098003504, http://journals.cambridge.org/article_S0022112098003504
61. Ricco, P., Wu, X.: Response of a compressible laminar boundary layer to free-stream vortical disturbances. J. Fluid Mech. **587**, 97–138 (2007). doi:10.1017/S0022112007007070, http://journals.cambridge.org/article_S0022112007007070
62. Morkovin, M.: On roughness induced transition: Facts, views, and speculations. In: Hussaini M., Voigt R. (eds.) Instability and Transition, ICASE/NASA LaRC Series, pp. 281–295. Springer US (1990). doi:10.1007/978-1-4612-3430-2_318, doi:10.1007/978-1-4612-3430-2_34
63. Joslin, R.D., Grosch, C.E.: Growth characteristics downstream of a shallow bump: Computation and experiment. Phys. Fluids **7**(12), 3042–3047 (1995). doi:10.1063/1.868680, http://scitation.aip.org/content/aip/journal/pof2/7/12/10.1063/1.868680
64. Tumin, A., Reshotko, E.: Receptivity of a boundary-layer flow to a three-dimensional hump at finite reynolds numbers. Phys. Fluids. **17**(9) (2005). doi:10.1063/1.2033907
65. Hanifi, A., Schmid, P.J., Henningson, D.S.: Transient growth in compressible boundary layer flow. Phys. Fluids **8**(3), 826–837 (1996). doi:10.1063/1.868864, http://scitation.aip.org/content/aip/journal/pof2/8/3/10.1063/1.868864
66. Tumin, A., Reshotko, E.: Spatial theory of optimal disturbances in boundary layers. Phys. Fluids **13**(7), 2097–2104 (2001)
67. Tumin, A., Reshotko, E.: Optimal disturbances in compressible boundary layers. AIAA J. **41**(12), 2357–2363 (2003)
68. De Tullio, N., Paredes, P., Sandham, N.D., Theofilis, V.: Laminar-turbulent transition induced by a discrete roughness element in a supersonic boundary layer. J. Fluid Mech. **735**, 613–646 (2013). doi:10.1017/jfm.2013.520
69. Swearingen, J.D., Blackwelder, R.F.: The growth and breakdown of streamwise vortices in the presence of a wall. J. Fluid Mech. **182**, 255–290 (1987). doi:10.1017/S0022112087002337
70. Sabry, A.S., Liu, J.T.C.: Longitudinal vorticity elements in boundary layers: nonlinear development from initial görtler vortices as a prototype problem. J. Fluid Mech. **231**, 615–663 (1991). doi:10.1017/S0022112091003543
71. Hall, P., Horseman, N.J.: The linear inviscid secondary instability of longitudinal vortex structures in boundary layers. J. Fluid Mech. **232**, 357–375 (1991). doi:10.1017/S0022112091003725
72. Yu, X., Liu, J.T.C.: The secondary instability in Goertler flow. Phys. Fluids A: Fluid Dyn. **3**(8), 1845–1847 (1991). doi:10.1063/1.857913
73. Yu, X., Liu, J.T.C.: On the mechanism of sinuous and varicose modes in three-dimensional viscous secondary instability of nonlinear Görtler rolls. Phys. Fluids **6**(2), 736–750 (1994). doi:10.1063/1.868312

74. Liu, W., Domaradzki, J.A.: Direct numerical simulation of transition to turbulence in Görtler flow. J. Fluid Mech. **246**, 267–299 (1993). doi:10.1017/S0022112093000126
75. Park, D.S., Huerre, P.: Primary and secondary instabilities of the asymptotic suction boundary layer on a curved plate. J. Fluid Mech. **283**, 249–272 (1995). doi:10.1017/S0022112095002308
76. Li, F., Malik, M.R.: Fundamental and subharmonic secondary instabilities of Görtler vortices. J. Fluid Mech. **297**, 77–100 (1995). doi:10.1017/S0022112095003016
77. Bottaro, A., Kingmann, B.: On the linear breakdown of Görtler vortices. Euro. J. Mech. B Fluids **15**(3), 301–330 (1996)
78. Tandiono, Winoto, S.H., Shah, D.A.: On the linear and nonlinear development of Görtler vortices. Phys. Fluids **20**(9), 094,103 (2008). doi:10.1063/1.2980349
79. Tandiono, Winoto, S.H., Shah, D.A.: Wall shear stress in Görtler vortex boundary layer flow. Phys. Fluids **21**(8), 084106 (2009). doi:10.1063/1.3205428
80. Andersson, P., Brandt, L., Bottaro, A., Henningson, D.S.: On the breakdown of boundary layer streaks. J. Fluid Mech. **428**, 29–60 (2001). doi:10.1017/S0022112000002421, http://journals.cambridge.org/article_S0022112000002421
81. Asai, M., Minagawa, M., Nishioka, M.: The instability and breakdown of a near-wall low-speed streak. J. Fluid Mech. **455**, 289–314 (2002). doi:10.1017/S0022112001007431
82. Ren, J., Fu, S.: Floquet analysis of fundamental, subharmonic and detuned secondary instabilities of Görtler vortices. Sci. China Phys. Mech. Astron. **57**(3), 555–561 (2014). doi:10.1007/s11433-014-5396-2
83. Whang, C., Zhong, X.: Secondary Görtler instability in hypersonic boundary layers. In :39th Aerospace Sciences Meeting Exhibit (2001). AIAA-2001-0273
84. Li, F., Choudhari, M., Chang, C.L., Wu, M., Greene, P.: Development and breakdown of Görtler vortices in high speed boundary layers. In: 50th Aerospace Sciences Meeting Including the New Horizons Forum and Aerospace Exposition (2010). doi: 10.2514/6.2010-705. AIAA-2010-0705
85. Choi, K.S.: Fluid dynamics: The rough with the smooth. Nature **440**(8), 754 (2006). doi:10.1038/440754a
86. Cossu, C., Brandt, L., Bagheri, S., Henningson, D.S.: Secondary threshold amplitudes for sinuous streak breakdown. Phys. Fluids **23**(7), 074103 (2011). doi:10.1063/1.3614480
87. Cossu, C., Brandt, L.: Stabilization of tollmien-schlichting waves by finite amplitude optimal streaks in the blasius boundary layer. Phys. Fluids **14**(8), L57–L60 (2002). doi:10.1063/1.1493791
88. Cossu, C., Brandt, L.: On tollmien-schlichting-like waves in streaky boundary layers. Euro. J. Mech. B/Fluids **23**(6), 815–833 (2004). doi:10.1016/j.euromechflu.2004.05.001
89. Bagheri, S., Hanifi, A.: The stabilizing effect of streaks on tollmien-schlichting and oblique waves: A parametric study. Phys. Fluids **19**(7), 078103 (2007). doi:10.1063/1.2746047
90. Fransson, J.H.M., Brandt, L., Talamelli, A., Cossu, C.: Experimental and theoretical investigation of the nonmodal growth of steady streaks in a flat plate boundary layer. Phys. Fluids **16**(10), 3627–3638 (2004). doi:10.1063/1.1773493
91. Fransson, J.H.M., Brandt, L., Talamelli, A., Cossu, C.: Experimental study of the stabilization of tollmien-schlichting waves by finite amplitude streaks. Phys. Fluids **17**(5), 054110 (2005). doi:10.1063/1.1897377
92. Fransson, J.H.M., Talamelli, A., Brandt, L., Cossu, C.: Delaying transition to turbulence by a passive mechanism. Phys. Rev. Lett. **96**, 064501 (2006). doi:10.1103/PhysRevLett.96.064501
93. Fransson, J.H.M., Talamelli, A.: On the generation of steady streamwise streaks in flat-plate boundary layers. J. Fluid Mech. **698**, 211–234 (2012). doi:10.1017/jfm.2012.80
94. Shahinfar, S., Sattarzadeh, S.S., Fransson, J.H.M., Talamelli, A.: Revival of classical vortex generators now for transition delay. Phys. Rev. Lett. **109**, 074501 (2012). doi:10.1103/PhysRevLett.109.074501
95. Shahinfar, S., Fransson, J.H.M., Sattarzadeh, S.S., Talamelli, A.: Scaling of streamwise boundary layer streaks and their ability to reduce skin-friction drag. J. Fluid Mech. **733**, 1–32 (2013). doi:10.1017/jfm.2013.431

96. Sattarzadeh, S.S., Fransson, J.H.: On the scaling of streamwise streaks and their efficiency to attenuate tollmien-schlichting waves. Exp. Fluids **56**(3), 58 (2015). doi:10.1007/s00348-015-1930-x
97. Siconolfi, L., Camarri, S., Fransson, J.H.M.: Boundary layer stabilization using free-stream vortices. J.Fluid Mech. **764**, R2 (2015). doi:10.1017/jfm.2014.731
98. Shahinfar, S., Sattarzadeh, S.S., Fransson, J.H.M.: Passive boundary layer control of oblique disturbances by finite-amplitude streaks. J. Fluid Mech. **749**, 1–36 (2014). doi:10.1017/jfm.2014.211
99. Saric, W.S., Carillo, R.B., Reibert, M.S.: Leading-edge roughness as a transition control mechanism. In: AIAA Paper 98-0781 (1998)
100. Saric, W.S., Reed, H.L.: Supersonic laminar flow control on swept wings using distributed roughness. In: AIAA paper 2002-0147 (2002)
101. Hosseini, S.M., Tempelmann, D., Hanifi, A., Henningson, D.S.: Stabilization of a swept-wing boundary layer by distributed roughness elements. J. Fluid Mech. **718**, R1 (2013). doi:10.1017/jfm.2013.33

# Chapter 2
# Methodology

## 2.1 Framework of the Stability Analysis

In Fig. 2.1, the numerical methods used in this thesis are outlined. Starting from the Navier-Stokes equations, the base flow is solved with boundary layer assumption. When perturbations are introduced into the flow, the stability equations can be obtained by subtracting the N-S equations of the laminar base flow. By parabolizing the stability equations, we make use of the high efficiency of the parabolized stability equations (PSE). The objective function and constraint are then made by introducing the adjoint equations. As a result, the optimal disturbances can be recovered. On the other hand, after linearizing the stability equations (LST), the equations can be solved locally as an eigenvalue problem or a singular value problem.

The study follows the procedure:

1. Solve the laminar base flow;
2. Perform the local modal and non-modal stability analysis;
3. Iterate the (linear) PSE and its adjoint equation to recover the optimal perturbations;
4. Calculate the nonlinear development and interactions of perturbations with the initial profiles from step 2 and/or 3;
5. Secondary instability analysis.



J. Ren, *Secondary Instabilities of Görtler Vortices in High-Speed Boundary Layers*, Springer Theses, https://doi.org/10.1007/978-981-10-6832-4_2

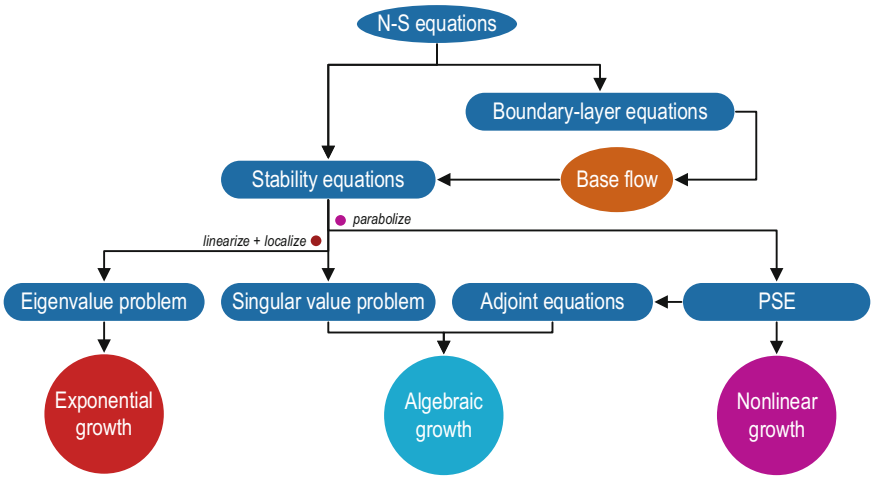


**Fig. 2.1** Framework of the stability analysis employed in this book

## 2.2 Governing Equations and the Base Flow

### *2.2.1 Governing Equations*

We start by writing the dimensional N-S equations in vector form:

$$\left.\begin{aligned}
\frac{\partial \rho^*}{\partial t^*} + \nabla^* \cdot \left(\rho^* \boldsymbol{V}^*\right) &= 0 \\
\rho^* \left(\frac{\partial \boldsymbol{V}^*}{\partial t^*} + \left(\boldsymbol{V}^* \cdot \nabla^*\right) \boldsymbol{V}^*\right) &= -\nabla^* p^* + \nabla^* \left(\lambda^* \left(\nabla^* \cdot \boldsymbol{V}^*\right)\right) \\
&\quad + \nabla^* \cdot \left(\mu^* \left(\nabla^* \boldsymbol{V}^* + \nabla^* \boldsymbol{V}^{*T}\right)\right) \\
{\rho^*}{C_p}^* \left(\frac{\partial T^*}{\partial t^*} + \left(\boldsymbol{V}^* \cdot \nabla^*\right) T^*\right) &= \nabla^* \cdot \left(\kappa^* \nabla^* T^*\right) \\
&\quad + \frac{\partial p^*}{\partial t^*} + \left(\boldsymbol{V}^* \cdot \nabla^*\right) p^* + \Phi^*
\end{aligned}\right\}. \tag{2.1}$$

The dissipation function in (2.1) is

$$\Phi^* = \lambda^* \left(\nabla^* \cdot \boldsymbol{V}^*\right)^2 + \frac{\mu^*}{2} \left(\nabla^* \boldsymbol{V}^* + \nabla^* \boldsymbol{V}^{*T}\right)^2, \tag{2.2}$$

$\boldsymbol{V}^* = (u^*, v^*, w^*)^T$ is the flow velocity. The coordinates employed in this thesis in shown in Fig. 1.5. $x$, $y$ and $z$ denote streamwise, normal-to-wall and spanwise directions respectively. The curvature of the wall is present in the streamwise direction.

The N-S equations are then scaled to remove the dimensions. The velocity is divided by $U_\infty^*$; thermodynamical quantities $\rho^*, T^*, \mu^*, \lambda^*$ and $\kappa^*$ by their freestream values; pressure $p^*$ by $\rho_\infty^* U_\infty^{*2}$; length and curvature by boundary layer thickness scale $\delta_0^* = \sqrt{\nu_\infty^* x_0^* / U_\infty^*}$ at $x_0^*$ and time $t^*$ by $\delta_0^*/U_\infty^*$, i.e.,

$$\left.\begin{aligned} u = \frac{u^*}{U_\infty^*},\ v = \frac{v^*}{U_\infty^*},\ w = \frac{w^*}{U_\infty^*} \\ \rho = \frac{\rho^*}{\rho_\infty^*},\ T = \frac{T^*}{T_\infty^*},\ \mu = \frac{\mu^*}{\mu_\infty^*},\ \lambda = \frac{\lambda^*}{\lambda_\infty^*},\ \kappa = \frac{\kappa^*}{\kappa_\infty^*} \\ x = \frac{x^*}{\delta_0^*},\ y = \frac{y^*}{\delta_0^*},\ z = \frac{z^*}{\delta_0^*},\ k = k^* \delta_0^* \\ p = \frac{p^*}{\rho_\infty^* (U_\infty^*)^2},\ t = \frac{t^* U_\infty^*}{\delta_0^*} \end{aligned}\right\} \tag{2.3}$$

As a result, the dimensionless form of the N-S equations are characterized with:

$$Re_0 = \frac{\rho_\infty^* U_\infty^* \delta_0^*}{\mu_\infty^*}, \quad Ma = \frac{U_\infty^*}{\sqrt{\gamma R_{\text{gas}}^* T_\infty^*}}, \quad Pr = \frac{\mu_\infty^* C_p^*}{\kappa_\infty^*}. \tag{2.4}$$

The N-S equations consists of 5 equations and 11 unknowns: $\rho, u, v, w, T, p, \mu, \lambda, \kappa, R_{\text{gas}}$ and $C_p$. Six complementary equations are prescribed for the closure of the system:
Equation of state (EoS) for perfect gas

$$\left.\begin{aligned} C_p^* = \text{CONST} \\ R_{\text{gas}}^* = \text{CONST} \\ p^* = \rho^* R_{\text{gas}}^* T^* \Leftrightarrow p = \frac{\rho T}{\gamma Ma^2} \end{aligned}\right\} \tag{2.5}$$

Constant $Pr$

$$Pr = \frac{C_p{}^* \mu^*}{\kappa^*} = \text{CONST} \Leftrightarrow \frac{\mu}{\mu_\infty} = \frac{\kappa}{\kappa_\infty} \tag{2.6}$$

Sutherland's law for viscosity

$$\left.\begin{aligned} \mu^* = \mu_s^* \frac{T^*}{T_s^*} \frac{T_s^* + S^*}{T^* + S^*} \Leftrightarrow \mu = \mu_s \frac{T}{T_s} \frac{T_s + S}{T + S} \\ T_s^* = 273K \\ \mu_s^* = 1.71 \times 10^{-5} kg/(m \cdot s) \\ S^* = 110.4K \end{aligned}\right\} \tag{2.7}$$

Stoke's hypothesis

$$\lambda^* + 2/3\mu^* = 0 \Leftrightarrow \lambda = -2/3\mu. \tag{2.8}$$

### 2.2.2 The Base Flow

For steady two-dimensional flows, the governing boundary layer equations can be derived from (2.1)[1]

$$\left.\begin{aligned} \frac{\partial(\rho^* u^*)}{\partial x^*} + \frac{\partial(\rho^* v^*)}{\partial y^*} = 0 \\ \rho^*\left(u^*\frac{\partial u^*}{\partial x^*} + v^*\frac{\partial u^*}{\partial y^*}\right) = -\frac{dp^*}{dx^*} + \frac{\partial}{\partial y^*}\left(\mu^*\frac{\partial u^*}{\partial y^*}\right) \\ \rho^*\left(u^*\frac{\partial H^*}{\partial x^*} + v^*\frac{\partial H^*}{\partial y^*}\right) = \frac{\partial}{\partial y^*}\left(\frac{\mu^*}{Pr}\frac{\partial H^*}{\partial y^*}\right) + \frac{\partial}{\partial y^*}\left[\left(1-\frac{1}{Pr}\right)\mu^* u^*\frac{\partial u^*}{\partial y^*}\right] \end{aligned}\right\} \tag{2.9}$$

where $H^*$ is the total enthalpy:

$$H^* = h^* + \frac{1}{2}u^*u^* = C_p^* T^* + \frac{1}{2}u^*u^* = \frac{\gamma}{\gamma-1}R_g^* T^* + \frac{1}{2}u^*u^* \tag{2.10}$$

Introduce the Levy-Lees transformation:

$$\left.\begin{aligned} d\xi = \rho_e^*\mu_e^* u_e^* dx^* \\ d\eta = \frac{\rho^* u_e^*}{\sqrt{2\xi}}dy^* \end{aligned}\right\} \tag{2.11}$$

Therefore, for perfect gas

$$\frac{\partial\eta}{\partial y^*} = \frac{\rho^* u_e^*}{\sqrt{2\xi}} = \frac{\rho^*}{\rho_e^*}\frac{\rho_e^* u_e^*}{\sqrt{2\xi}} \propto \rho = \frac{1}{T} \tag{2.12}$$

Define the stream function $\psi$

$$\rho^* u^* = \frac{\partial\psi^*}{\partial y^*},\ \rho^* v^* = -\frac{\partial\psi^*}{\partial x^*} \tag{2.13}$$

A dimensionless stream function $f$ is related to $\psi^*$ as:

$$\psi^*(x,\ y) = \sqrt{2\xi}\, f(\xi,\ \eta) \tag{2.14}$$

The dimensionless function $g$ is defined as

$$g\left(\xi,\ \eta\right)=\frac{H^*}{H_\infty^*} \tag{2.15}$$

Substituting (2.11), (2.13), (2.14) and (2.15) into the boundary layer Eq. (2.9), yields

$$\left.\begin{aligned} 2\xi\left(f'\frac{\partial f'}{\partial\xi}-\frac{\partial f}{\partial\xi}f''\right)&=\beta_p\left[\left(k+1\right)\left(g-f'^2\right)\right]+\left(Cf''\right)'+ff''\\ 2\xi\left(f'\frac{\partial g}{\partial\xi}-\frac{\partial f}{\partial\xi}g'\right)&=\left(a_1g'\right)'+\left(a_2f'f''\right)'+fg'\end{aligned}\right\} \tag{2.16}$$

where

$$\left.\begin{aligned} \beta_p&=\frac{2\xi}{u_e^*}\frac{du_e^*}{d\xi}\\ C&=\frac{\rho^*\mu^*}{\rho_e^*\mu_e^*}=\frac{\mu}{T}\\ k_M&=\frac{\gamma-1}{2}Ma^2\\ a_1&=\frac{C}{Pr}\\ a_2&=C\left(1-\frac{1}{Pr}\right)\frac{2k_M}{1+k_M}\end{aligned}\right\} \tag{2.17}$$

The flow temperature can be recovered from

$$\frac{T^*}{T_e^*}=\left(k_M+1\right)g-k_Mf'^2. \tag{2.18}$$

The boundary conditions are specified

$$\left.\begin{aligned} u^*=v^*&=0\\ \frac{\partial H^*}{\partial y^*}&=0\ \text{(adiabatic)}\\ H^*&=H_{\text{wall}}^*\ \text{(isothermal)}\end{aligned}\right\}\ \text{at}\ y^*=0 \tag{2.19}$$

$$\left.\begin{aligned} u^*&=U_\infty^*\\ H^*&=H_\infty^*\end{aligned}\right\}\ \text{at}\ y^*=\infty \tag{2.20}$$

Accordingly, (2.16) is subject to

$$\left.\begin{aligned} f=f'=0,\ g'=0\ (\text{or}\ g=g_{\text{wall}})\ \text{at}\ \eta=0\\ f'=1,\ g=1\ \text{at}\ \eta=\infty\end{aligned}\right\} \tag{2.21}$$

The resulting boundary value problem of (2.16) provides the similarity solution for compressible boundary layers which serves as the base flow. One may notice the

streamwise curvature is omitted in the base flow. This is a high-order influence on Görtler instability [2].

## 2.3 Stability Equations and Numerical Methods

The instantaneous flow field $\boldsymbol{q} = (\rho,\ u,\ v,\ w,\ T)$ consists of the laminar base flow $\boldsymbol{q}_0$ plus the perturbation $\tilde{\boldsymbol{q}}$:

$$\boldsymbol{q}(x, y, z, t) = \boldsymbol{q}_0(x, y) + \tilde{\boldsymbol{q}}(x, y, z, t) \tag{2.22}$$

The perturbed flow $\boldsymbol{q}$ and the base flow $\boldsymbol{q}_0$ both satisfie the N-S equations. We substitute (2.22) into the N-S Eq. (2.1) and subtract equation of the base flow. The stability equation is then derived:

$$\begin{aligned}\boldsymbol{\Gamma}\frac{\partial\tilde{\boldsymbol{q}}}{\partial t} + \boldsymbol{A}\frac{\partial\tilde{\boldsymbol{q}}}{\partial x} + \boldsymbol{B}\frac{\partial\tilde{\boldsymbol{q}}}{\partial y} + \boldsymbol{C}\frac{\partial\tilde{\boldsymbol{q}}}{\partial z} + \boldsymbol{D}\tilde{\boldsymbol{q}} = \boldsymbol{V}_{xx}\frac{\partial^2\tilde{\boldsymbol{q}}}{\partial x^2} + \boldsymbol{V}_{yy}\frac{\partial^2\tilde{\boldsymbol{q}}}{\partial y^2} \\ + \boldsymbol{V}_{zz}\frac{\partial^2\tilde{\boldsymbol{q}}}{\partial z^2} + \boldsymbol{V}_{xy}\frac{\partial^2\tilde{\boldsymbol{q}}}{\partial x\partial y} + \boldsymbol{V}_{yz}\frac{\partial^2\tilde{\boldsymbol{q}}}{\partial y\partial z} + \boldsymbol{V}_{zx}\frac{\partial^2\tilde{\boldsymbol{q}}}{\partial z\partial x} + \tilde{\boldsymbol{N}}\end{aligned} \tag{2.23}$$

where the $5 \times 5$ matrices $\boldsymbol{\Gamma}$, $\boldsymbol{A}$, $\boldsymbol{B}$, $\boldsymbol{C}$, $\boldsymbol{D}$, $\boldsymbol{V}_{xx}$, $\boldsymbol{V}_{yy}$, $\boldsymbol{V}_{zz}$, $\boldsymbol{V}_{xy}$, $\boldsymbol{V}_{xz}$, $\boldsymbol{V}_{yz}$ are functions of the base flow, curvature and the dimensionless parameters $Re$, $Ma$, $Pr$. Detailed expressions can be found in one of the author's journal articles [3]. The vector $\tilde{\boldsymbol{N}}$ indicates nonlinear terms.

### *2.3.1 Modal Stability: The Eigenvalue Problem*

Assume wavelike solutions of the form:

$$\tilde{\boldsymbol{q}}(x, y, z, t) = \hat{\boldsymbol{q}}(y)\exp\left(\mathrm{i}(\alpha x + \beta z - \omega t)\right) + c.c. \tag{2.24}$$

Substitute into (2.23) and ignore the nonlinear terms. In this work, $\beta$ and $\omega$ are prescribed (spatial problem) and $\alpha$ is to be solved.

$$\mathbf{A}\hat{\boldsymbol{q}} + \mathbf{B}\frac{\partial\hat{\boldsymbol{q}}}{\partial y} + \mathbf{C}\frac{\partial^2\hat{\boldsymbol{q}}}{\partial y^2} = \alpha\left(\mathbf{M}\hat{\boldsymbol{q}} + \mathbf{N}\frac{\partial\hat{\boldsymbol{q}}}{\partial y}\right) + \alpha^2\mathbf{P}\hat{\boldsymbol{q}} \tag{2.25}$$

where

$$\left.\begin{aligned}
\mathbf{A} &= -\mathrm{i}\omega\boldsymbol{\Gamma} + \mathrm{i}\beta\boldsymbol{C} + \boldsymbol{D} + \beta^2\boldsymbol{V}_{zz} \\
\mathbf{B} &= \boldsymbol{B} - \mathrm{i}\beta\boldsymbol{V}_{yz} \\
\mathbf{C} &= -\boldsymbol{V}_{yy} \\
\mathbf{M} &= -\mathrm{i}\boldsymbol{A} - \beta\boldsymbol{V}_{xz} \\
\mathbf{N} &= \mathrm{i}\boldsymbol{V}_{xy} \\
\mathbf{P} &= -\boldsymbol{V}_{xz}
\end{aligned}\right\} \tag{2.26}$$

(2.25) is the eigenvalue equation to be solved. We make use of the 4th-order central differential scheme:

$$\left.\begin{aligned}
\frac{\partial\hat{\boldsymbol{q}}_j}{\partial y} &= \frac{\hat{\boldsymbol{q}}_{j-2} - 8\hat{\boldsymbol{q}}_{j-1} + 8\hat{\boldsymbol{q}}_{j+1} - \hat{\boldsymbol{q}}_{j+2}}{12\Delta y} \\
\frac{\partial^2\hat{\boldsymbol{q}}_j}{\partial y^2} &= \frac{-\hat{\boldsymbol{q}}_{j-2} + 16\hat{\boldsymbol{q}}_{j-1} - 30\hat{\boldsymbol{q}}_j + 16\hat{\boldsymbol{q}}_{j+1} - \hat{\boldsymbol{q}}_{j+2}}{12(\Delta y)^2}
\end{aligned}\right\}. \tag{2.27}$$

We defined the discretized vector $\hat{\boldsymbol{Q}} = (\hat{\boldsymbol{q}}_1,\ \hat{\boldsymbol{q}}_2,\ \cdots,\ \hat{\boldsymbol{q}}_j,\ \cdots,\ \hat{\boldsymbol{q}}_N)$. The finite-difference procedure therefore can be written in matrix form:

$$\left.\begin{aligned}
\boldsymbol{F}_y\hat{\boldsymbol{Q}} &= \left(\frac{\partial\hat{\boldsymbol{q}}_1}{\partial y},\ \frac{\partial\hat{\boldsymbol{q}}_2}{\partial y},\ \cdots,\ \frac{\partial\hat{\boldsymbol{q}}_j}{\partial y},\ \cdots,\ \frac{\partial\hat{\boldsymbol{q}}_N}{\partial y}\right) \\
\boldsymbol{F}_{yy}\hat{\boldsymbol{Q}} &= \left(\frac{\partial^2\hat{\boldsymbol{q}}_1}{\partial y^2},\ \frac{\partial^2\hat{\boldsymbol{q}}_2}{\partial y^2},\ \cdots,\ \frac{\partial^2\hat{\boldsymbol{q}}_j}{\partial y^2},\ \cdots,\ \frac{\partial^2\hat{\boldsymbol{q}}_N}{\partial y^2}\right)
\end{aligned}\right\} \tag{2.28}$$

(2.25) becomes

$$\left(\mathbf{A}' + \mathbf{B}'\boldsymbol{F}_y + \mathbf{C}'\boldsymbol{F}_{yy}\right)\hat{\boldsymbol{Q}} = \alpha\left(\mathbf{M}' + \mathbf{N}'\boldsymbol{F}_y\right)\hat{\boldsymbol{Q}} + \alpha^2\mathbf{P}'\hat{\boldsymbol{Q}} \tag{2.29}$$

where matrices of the size $5N \times 5N$ $\boldsymbol{A}'$, $\boldsymbol{B}'$, $\boldsymbol{C}'$, $\boldsymbol{M}'$, $\boldsymbol{N}'$, $\boldsymbol{P}'$ are the discretizations of $\boldsymbol{A}$, $\boldsymbol{B}$, $\boldsymbol{C}$, $\boldsymbol{M}$, $\boldsymbol{N}$, $\boldsymbol{P}$. (2.29) is a nonlinear eigenvalue equation and can be linearized through:

$$\begin{pmatrix} \boldsymbol{O} & \boldsymbol{I} \\ \mathbf{A}' + \mathbf{B}'\boldsymbol{F}_y + \mathbf{C}'\boldsymbol{F}_{yy} & -\mathbf{M}' - \mathbf{N}'\boldsymbol{F}_y \end{pmatrix}\begin{pmatrix} \hat{\boldsymbol{Q}} \\ \alpha\hat{\boldsymbol{Q}} \end{pmatrix} = \alpha\begin{pmatrix} \boldsymbol{I} & \boldsymbol{O} \\ \boldsymbol{O} & \mathbf{P}' \end{pmatrix}\begin{pmatrix} \hat{\boldsymbol{Q}} \\ \alpha\hat{\boldsymbol{Q}} \end{pmatrix} \tag{2.30}$$

The boundary conditions for (2.30) is

$$\begin{cases} \hat{u} = \hat{v} = \hat{w} = \hat{T} = 0 & \text{at } y = 0 \\ \hat{u} = \hat{v} = \hat{w} = \hat{T} = 0 & \text{at } y = \infty \end{cases} \tag{2.31}$$

Numerically solving (2.30), one obtains the eigenvector $\hat{\boldsymbol{Q}}$ (the perturbation) and the eigenvalue $\alpha$, where $-\alpha_i$ is the growth rate and $\alpha_r$ is the streamwise wavenumber.

### 2.3.2 Algebraic Stability: The Singular Value Problem

In algebraic stability analysis, no assumption is made on the perturbation along $x$:

$$\tilde{\boldsymbol{q}}(x, y, z, t) = \hat{\boldsymbol{q}}(x, y) \exp\left(\mathrm{i}(\beta z - \omega t)\right) + c.c. \tag{2.32}$$

Substitute into (2.23), ignore the nonlinear terms, in an operator form, we have

$$\frac{\mathrm{d}\hat{\boldsymbol{q}}}{\mathrm{d}x} = \mathscr{L}\hat{\boldsymbol{q}} \tag{2.33}$$

The solution is

$$\hat{\boldsymbol{q}}(x) = \hat{\boldsymbol{q}}(0) e^{x\mathscr{L}} \tag{2.34}$$

Define the inner product of any two vectors:

$$\langle \hat{\boldsymbol{p}},\ \hat{\boldsymbol{q}} \rangle = \int_0^\infty \hat{\boldsymbol{p}}^H \hat{\boldsymbol{q}} \mathrm{d}y \tag{2.35}$$

An energy norm is defined on the inner product space:

$$\|\hat{\boldsymbol{q}}\|_E = \langle \hat{\boldsymbol{q}},\ \boldsymbol{M}\hat{\boldsymbol{q}} \rangle \tag{2.36}$$

where

$$\boldsymbol{M} = \mathrm{diag}\left( \frac{\hat{T}}{\bar{\rho}\gamma Ma^2},\ \bar{\rho},\ \bar{\rho},\ \bar{\rho},\ \frac{\bar{\rho}}{\gamma(\gamma-1)\hat{T}Ma^2} \right) \tag{2.37}$$

is a diagonal matrix (positive definite), take Cholesky decomposition:

$$\boldsymbol{M} = \boldsymbol{F}^H \boldsymbol{F} \tag{2.38}$$

The energy norm (2.36) [4] measures the perturbation energy at a specified streamwise location and, can be related to the 2−norm through

$$\begin{aligned} \|\hat{\boldsymbol{q}}\|_E = \langle \hat{\boldsymbol{q}},\ \boldsymbol{M}\hat{\boldsymbol{q}} \rangle &= \int_0^\infty \hat{\boldsymbol{q}}^H \boldsymbol{M}\hat{\boldsymbol{q}} \mathrm{d}y \\ &= \int_0^\infty \hat{\boldsymbol{q}}^H \boldsymbol{F}^H \boldsymbol{F}\hat{\boldsymbol{q}} \mathrm{d}y = \langle \boldsymbol{F}\hat{\boldsymbol{q}}, \boldsymbol{F}\hat{\boldsymbol{q}} \rangle = \|\boldsymbol{F}\hat{\boldsymbol{q}}\|_2^2 \end{aligned} \tag{2.39}$$

(2.36) can be further extended to the energy norm of matrices:

$$\|\boldsymbol{A}\|_E = \max \frac{\|\boldsymbol{A}\hat{\boldsymbol{q}}\|_E}{\|\hat{\boldsymbol{q}}\|_E} = \max \frac{\|\boldsymbol{F}\boldsymbol{A}\boldsymbol{F}^{-1}\boldsymbol{F}\hat{\boldsymbol{q}}\|_2^2}{\|\boldsymbol{F}\hat{\boldsymbol{q}}\|_2^2} = \|\boldsymbol{F}\boldsymbol{A}\boldsymbol{F}^{-1}\|_2^2 \tag{2.40}$$

The eigenvalue and eigenvector solved in Sect. 2.3.1 give the solution for $x \to \infty$ which is not necessarily consistent with the flow physics. Take Couette flow as an example, its growth rate is negative (stable) at any given $Re$. However, flow instability is still observed in experiments. The reason is that the matrix of the eigenvalue problem is usually non-regular. Thus its eigenvectors are not orthogonal to each other. The perturbation may become unstable after linear combinations:

$$\breve{\boldsymbol{q}}(x) = \sum_{k=1}^{K} \phi_k(x) \hat{\boldsymbol{q}}_k \tag{2.41}$$

where $\phi_k(x) = \phi_k(0) e^{\mathrm{i}\alpha_k x}$, In a finite streamwise domain from 0 to $x$, we measure the maximum possible amplification factor of the perturbation energy $G$.

$$\begin{aligned} G(\beta, \omega, Re, x) &= \max \frac{\|\breve{\boldsymbol{q}}(x)\|_E}{\|\breve{\boldsymbol{q}}(0)\|_E} = \max \frac{\|\breve{\boldsymbol{q}}(0) e^{x\mathscr{L}}\|_E}{\|\breve{\boldsymbol{q}}(0)\|_E} \\ &= \|e^{x\mathscr{L}}\|_E = \|\boldsymbol{F}\boldsymbol{\Lambda}\boldsymbol{F}^{-1}\|_2^2 \end{aligned} \tag{2.42}$$

where

$$\boldsymbol{\Lambda} = \mathrm{diag}\left(e^{\mathrm{i}\alpha_1 x},\ e^{\mathrm{i}\alpha_2 x},\ \cdots,\ e^{\mathrm{i}\alpha_K x}\right) \tag{2.43}$$

The matrix $\boldsymbol{F}$ satisfies $\boldsymbol{F}^H \boldsymbol{F} = \boldsymbol{A}$. The matrix $\boldsymbol{A}$ is given by the elements $a_{ij} = \langle \hat{\boldsymbol{q}}_i,\ \hat{\boldsymbol{q}}_j \rangle$. The 2-norm of $\boldsymbol{F}\boldsymbol{\Lambda}\boldsymbol{F}^{-1}$ therefore can be determined from its maximum singular value $\sigma_1$.

### 2.3.3 PSE

The limitations for local eigenvalue or singular problem are:

1. The stability equations are solved locally, thus, the base flow must be quasi-parallel. For example, Görtler instability can not be solved locally except when the streamwise coordinate is large where the flow is quasi-parallel (Sect. 1).
2. Nonlinear terms are ignored. Therefore, the amplitude of the perturbation must be small enough.

The parabolized stability equations (PSE) overcome the above and is more efficient than eigenvalue problem. Take Fourier expansions for the perturbation $\tilde{\boldsymbol{q}}$ and nonlinear terms $\tilde{\boldsymbol{N}}$:

$$\left.\begin{aligned}\tilde{\boldsymbol{q}} &= \sum_{m=-M}^{M}\sum_{n=-N}^{N}\hat{\boldsymbol{q}}_{mn}(x,y)\exp\left(\mathrm{i}\int\alpha_{mn}\mathrm{d}x+\mathrm{i}n\beta z-\mathrm{i}m\omega t\right)\\ \tilde{\boldsymbol{N}} &= -\sum_{m=-M}^{M}\sum_{n=-N}^{N}\hat{\boldsymbol{N}}_{mn}(x,y)\exp\left(\mathrm{i}\int\alpha_{mn}\mathrm{d}x+\mathrm{i}n\beta z-\mathrm{i}m\omega t\right)\end{aligned}\right\} \tag{2.44}$$

Substitute into (2.23), we have

$$\begin{aligned}&\mathbf{A}\hat{\boldsymbol{q}}_{mn}+\mathbf{B}\frac{\partial\hat{\boldsymbol{q}}_{mn}}{\partial y}+\mathbf{C}\frac{\partial^2\hat{\boldsymbol{q}}_{mn}}{\partial y^2}+\mathbf{D}\frac{\partial\hat{\boldsymbol{q}}_{mn}}{\partial x}\\ &\quad+\mathbf{E}\frac{\partial^2\hat{\boldsymbol{q}}_{mn}}{\partial x\partial y}+\mathbf{F}\frac{\partial^2\hat{\boldsymbol{q}}_{mn}}{\partial x^2}+\hat{\boldsymbol{N}}_{mn}\exp\left(-\mathrm{i}\int\alpha_{mn}\mathrm{d}x\right)=0\end{aligned} \tag{2.45}$$

where

$$\left.\begin{aligned}\mathbf{A} &= -\mathrm{i}m\omega\boldsymbol{\Gamma}+\mathrm{i}n\beta\boldsymbol{C}+\boldsymbol{D}+\beta^2n^2\boldsymbol{V}_{zz}+\mathrm{i}\alpha_{mn}\boldsymbol{A}\\ &\quad+(\alpha_{mn}^2-\mathrm{i}\alpha_{mn,x})\boldsymbol{V}_{xx}+n\beta\alpha_{mn}\boldsymbol{V}_{xz}\\ \mathbf{B} &= \boldsymbol{B}-\mathrm{i}n\beta\boldsymbol{V}_{yz}-\mathrm{i}\alpha_{mn}\boldsymbol{V}_{xy}\\ \mathbf{C} &= -\boldsymbol{V}_{yy}\\ \mathbf{D} &= \boldsymbol{A}-\mathrm{i}n\beta\boldsymbol{V}_{xz}-2\mathrm{i}\alpha_{mn}\boldsymbol{V}_{xx}\\ \mathbf{E} &= -\boldsymbol{V}_{xy}\\ \mathbf{F} &= -\boldsymbol{V}_{xx}\end{aligned}\right\} \tag{2.46}$$

An axillary equation for $\alpha_{mn}$ (2.47) is required to make the shape function $\hat{\boldsymbol{q}}_{mn}$ evolves slowly in the streamwise direction. i.e., $\frac{\partial\hat{\boldsymbol{q}}_{mn}}{\partial x}\sim\mathscr{O}(1/Re)$.

$$\alpha^{\mathrm{new}}=\alpha^{\mathrm{old}}-\mathrm{i}\frac{\int_0^\infty\rho\left(\hat{u}^\dagger\partial\hat{u}/\partial x+\hat{v}^\dagger\partial\hat{v}/\partial x+\hat{w}^\dagger\partial\hat{w}/\partial x\right)\mathrm{d}y}{\int_0^\infty\rho\left(\hat{u}^\dagger\hat{u}+\hat{v}^\dagger\hat{v}+\hat{w}^\dagger\hat{w}\right)\mathrm{d}y} \tag{2.47}$$

Through the magnitude analysis of (2.45), we have $\mathbf{A}\sim\mathbf{B}\sim\mathbf{D}\sim\mathscr{O}(1)$, $\mathbf{C}\sim\mathbf{E}\sim\mathbf{F}\sim\mathscr{O}(1/Re)$, $\partial\hat{\boldsymbol{q}}_{mn}/\partial y\sim\mathscr{O}(1)$, $\partial\hat{\boldsymbol{q}}_{mn}/\partial x\sim\mathscr{O}(1/Re)$. Ignore terms of order $O(1/Re^2)$ and above, the equation is parabolized:

$$\mathbf{A}\hat{\boldsymbol{q}}_{mn}+\mathbf{B}\frac{\partial\hat{\boldsymbol{q}}_{mn}}{\partial y}+\mathbf{C}\frac{\partial^2\hat{\boldsymbol{q}}_{mn}}{\partial y^2}+\mathbf{D}\frac{\partial\hat{\boldsymbol{q}}_{mn}}{\partial x}+\hat{\boldsymbol{N}}_{mn}\exp\left(-\mathrm{i}\int\alpha_{mn}\mathrm{d}x\right)=0 \tag{2.48}$$

The fourth order central difference (2.27) and implicit Euler scheme is applied in the $y$ and $x$ directions respectively. The discretized equations become

$$\left(\mathbf{A}'+\mathbf{B}'\boldsymbol{F}_y+\mathbf{C}'\boldsymbol{F}_{yy}\right)\hat{\boldsymbol{Q}}_{mn}+\mathbf{D}'\frac{\partial\hat{\boldsymbol{Q}}_{mn}}{\partial x}+\hat{\boldsymbol{N}}'_{mn}\exp\left(-\mathrm{i}\int\alpha_{mn}\mathrm{d}x\right)=0 \tag{2.49}$$

The nonlinear terms in (2.49) are calculated iteratively with local physical quantities. By marching downstream, the spatial development of the perturbation is solved. Discussions on the residual ellipticity of PSE can be found in [5, 6] and validation is provided by [7–9].

It is important to note, the streamwise wavenumber of Görtler mode and Klebanoff mode $\alpha_r \equiv 0$. Their shape functions evolve slowly in the streamwise physically. As a result, the governing equations are parabolic in nature. No auxiliary condition is applied. (2.48) is simplified as

$$\mathbf{A}\hat{\boldsymbol{q}}_{mn} + \mathbf{B}\frac{\partial \hat{\boldsymbol{q}}_{mn}}{\partial y} + \mathbf{C}\frac{\partial^2 \hat{\boldsymbol{q}}_{mn}}{\partial y^2} + \mathbf{D}\frac{\partial \hat{\boldsymbol{q}}_{mn}}{\partial x} + \hat{N}_{mn} = 0 \tag{2.50}$$

The detailed expressions of matrices $\mathbf{A}$, $\mathbf{B}$, $\mathbf{C}$, $\mathbf{D}$ are provided in the Appendix.

### 2.3.4 Secondary Instability Equations

In the methodology of the linear secondary instability (Herbert 1988; Schmid and Henningson 2001), the stability analysis is performed typically in a y-z cross-section (so-called Bi-global). The disturbances, therefore, are assumed to be inhomogeneous in the wall-normal and spanwise direction but periodic in time and streamwise direction, i.e.,

$$\left.\begin{aligned} \tilde{\boldsymbol{q}}_{0s}(y,z) &= \sum_{n_1=-\infty}^{\infty} \hat{\boldsymbol{q}}_{0n_1}(y)\, e^{\mathrm{i}n_1\beta z} \\ \tilde{\boldsymbol{q}}_s(x,y,z,t) &= e^{\gamma z} e^{\omega_s t + \mathrm{i}\alpha_s x} \sum_{n_2=-\infty}^{\infty} \hat{\boldsymbol{q}}_{n_2}(y)\, e^{\mathrm{i}n_2\beta z} \\ 0 \le \gamma_i &\le \frac{\beta}{2} \end{aligned}\right\} \tag{2.51}$$

where $0 \le \gamma_i/\beta \le 0.5$ is the Floquet parameter and decides the type of the secondary instability. $\gamma_i/\beta = 0$ produces the fundamental, $\gamma_i/\beta = 0.5$ the subharmonic and the other values result in detuned types. Substitute (2.51) into the N-S Eq. (2.1), after a similar procedure as in the primary instability (Sect. 2.3.1) the secondary instability equations can be obtained. The temporal problem is solved with $\alpha_s$ prescribed and $\omega_s$ is the eigenvalue to be determined.

## 2.4 Adjoint Equations and Optimal Perturbations

### *2.4.1 Adjoint Equations*

The stability equations described in Sects. 2.3.1 and 2.3.3 can be written in the form of operators after linearization:

$$\mathscr{L}\hat{\boldsymbol{q}} = 0 \tag{2.52}$$

With the inner product defined in Sect. 2.3.2, we define the adjoint operator $\mathscr{L}^*$ which satisfies

$$\left\langle \hat{\boldsymbol{p}},\ \mathscr{L}\hat{\boldsymbol{q}} \right\rangle = \left\langle \mathscr{L}^*\hat{\boldsymbol{p}},\ \hat{\boldsymbol{q}} \right\rangle + \text{B.C.} \tag{2.53}$$

where $\hat{\boldsymbol{p}}$ is the adjoint vector to $\hat{\boldsymbol{q}}$, B.C. denotes the boundary terms after integration. For the equations of PSE,

$$\mathscr{L} = \mathbf{A} + \mathbf{B}\frac{\partial}{\partial y} + \mathbf{C}\frac{\partial^2}{\partial y^2} + \mathbf{D}\frac{\partial}{\partial x} \tag{2.54}$$

Integrating (2.53) by parts yields

$$\mathscr{L}^* = \mathbf{A}^* + \mathbf{B}^*\frac{\partial}{\partial y} + \mathbf{C}^*\frac{\partial^2}{\partial y^2} + \mathbf{D}^*\frac{\partial}{\partial x} \tag{2.55}$$

where

$$\left.\begin{aligned} \mathbf{A}^* &= \mathbf{A}^H - \frac{\partial \mathbf{B}^H}{\partial y} + \frac{\partial^2 \mathbf{C}^H}{\partial y^2} - \frac{\partial \mathbf{D}^H}{\partial x} \\ \mathbf{B}^* &= -\mathbf{B}^H + 2\frac{\partial \mathbf{C}^H}{\partial y} \\ \mathbf{C}^* &= \mathbf{C}^H \\ \mathbf{D}^* &= -\mathbf{D}^H \end{aligned}\right\} \tag{2.56}$$

To remove the boundary terms in (2.53), the boundary condition for $\hat{\boldsymbol{p}} = (\hat{\rho}^\dagger,\ \hat{u}^\dagger,\ \hat{v}^\dagger,\ \hat{w}^\dagger,\ \hat{T}^\dagger)$ is specified:

$$\begin{cases} \hat{u}^\dagger = \hat{v}^\dagger = \hat{w}^\dagger = \hat{T}^\dagger = 0 & y = 0 \\ \hat{u}^\dagger = \hat{v}^\dagger = \hat{w}^\dagger = \hat{T}^\dagger = 0 & y = \infty \end{cases} \tag{2.57}$$

The adjoint equations are therefore written:

$$\mathscr{L}^*\hat{\boldsymbol{p}} = 0 \tag{2.58}$$

The numerical procedure is similar to solving PSE, except for the marching is backward from downstream to upstream.

### 2.4.2 Optimal Perturbations

The optimal perturbation can be recovered with Lagrange-multiplier. The objective function is the perturbation energy at $x = x_1$ divided by the value at the inlet $x = x_0$:

$$J(\hat{\boldsymbol{q}}) = \frac{\|\hat{\boldsymbol{q}}_1\|_E}{\|\hat{\boldsymbol{q}}_0\|_E} \tag{2.59}$$

We define the functional

$$\mathscr{F}(\hat{\boldsymbol{q}},\ \hat{\boldsymbol{p}}) = J(\hat{\boldsymbol{q}}) - \left\langle \hat{\boldsymbol{p}},\ \mathscr{L}\hat{\boldsymbol{q}} \right\rangle \tag{2.60}$$

To seek the maximum value of the objective $J(\hat{\boldsymbol{q}})$, we seek the stagnation point of the functional (2.60). Take variation of (2.60):

$$\delta\mathscr{F} = \left\langle \nabla_{\hat{\boldsymbol{p}}}\mathscr{F},\ \delta\hat{\boldsymbol{p}} \right\rangle + \left\langle \nabla_{\hat{\boldsymbol{q}}}\mathscr{F},\ \delta\hat{\boldsymbol{q}} \right\rangle \tag{2.61}$$

In order the variation is 0, the two parts in (2.61) must both equal to 0. The first part:

$$\left\langle \nabla_{\hat{\boldsymbol{p}}}\mathscr{F},\ \delta\hat{\boldsymbol{p}} \right\rangle = 0 \Leftrightarrow \mathscr{L}\hat{\boldsymbol{q}} = 0 \tag{2.62}$$

is satisfied by solving the stability equations. With the definition of the adjoint operator (2.53), the second part is

$$\begin{aligned} \left\langle \nabla_{\hat{\boldsymbol{q}}}\mathscr{F},\ \delta\hat{\boldsymbol{q}} \right\rangle = 0 \Leftrightarrow & -\left\langle \mathscr{L}^*\hat{\boldsymbol{p}},\ \delta\hat{\boldsymbol{q}} \right\rangle \\ & + \left\langle \mathbf{D}^H\hat{\boldsymbol{p}}_0,\ \delta\hat{\boldsymbol{q}}_0 \right\rangle - \left\langle \mathbf{D}^H\hat{\boldsymbol{p}}_1,\ \delta\hat{\boldsymbol{q}}_1 \right\rangle \\ & - \left\langle \frac{\|\hat{\boldsymbol{q}}_1\|_E}{\|\hat{\boldsymbol{q}}_0\|_E^2}\boldsymbol{M}\hat{\boldsymbol{q}}_0,\ \delta\hat{\boldsymbol{q}}_0 \right\rangle \\ & + \left\langle \frac{1}{\|\hat{\boldsymbol{q}}_0\|_E}\boldsymbol{M}\hat{\boldsymbol{q}}_1,\ \delta\hat{\boldsymbol{q}}_1 \right\rangle \end{aligned} \tag{2.63}$$

where $\left\langle \mathscr{L}^*\hat{\boldsymbol{p}},\ \delta\hat{\boldsymbol{q}} \right\rangle = 0$ is equivalent to solving the adjoint equations. At $x = x_0$ and $x = x_1$:

$$\left.\begin{aligned} \mathbf{D}^H\hat{\boldsymbol{p}}_0 - \frac{\|\hat{\boldsymbol{q}}_1\|_E}{\|\hat{\boldsymbol{q}}_0\|_E^2}\boldsymbol{M}\hat{\boldsymbol{q}}_0 = 0 \\ -\mathbf{D}^H\hat{\boldsymbol{p}}_1 + \frac{1}{\|\hat{\boldsymbol{q}}_0\|_E}\boldsymbol{M}\hat{\boldsymbol{q}}_1 = 0 \end{aligned}\right\} \tag{2.64}$$

Therefore, we have the initial condition for the direct and adjoint equations:

$$\left.\begin{aligned}\hat{\boldsymbol{q}}_0 &= c_0 \boldsymbol{M}^{-1} \mathbf{D}^H \hat{\boldsymbol{p}}_0 \\ \hat{\boldsymbol{p}}_1 &= c_1 (\mathbf{D}^H)^{-1} \boldsymbol{M} \hat{\boldsymbol{q}}_1\end{aligned}\right\} \tag{2.65}$$

where $c_0$ and $c_1$ are constants. For linear problems, they have no influence on the results. The optimal pertubation is obtained by solving iteratively (2.52), (2.58) and (2.65) :

1. Determine the location of the inlet $x_0$ and the outlet of the optimal perturbation $x_1$;
2. Solve the eigenvalue problem to obtain the intial perturbation $\hat{\boldsymbol{q}}_0$;
3. March the direct Eq. (2.52) from $x_0$ to $x_1$;
4. From (2.65), obtain the initial condition $\hat{\boldsymbol{p}}_1$ for the adjoint equation at $x_1$;
5. March the adjoint Eq. (2.58) from $x_1$ to $x_0$;
6. From (2.65), obtain the initial condition $\hat{\boldsymbol{q}}_0$ for the direct equation at $x_0$.

repeat step 3–6, until the objective function (2.59) reaches a convergence. Usually it takes only 3–4 iterations.

## References


1. Schlichting, H., Gersten, K.: Boundary-Layer Theory. Springer, Berlin (2017). doi:10.1007/978-3-662-52919-5
2. Floryan, J.M., Saric, W.S.: Stability of Görtler vortices in boundary layers. AIAA J. **20**(3), 316–324 (1982)
3. Ren, J., Fu, S.: Competition of the multiple Görtler modes in hypersonic boundary layer flows. Sci. China Phys. Mech. Astron. **57**(6), 1178–1193 (2014). doi:10.1007/s11433-014-5454-9
4. Hanifi, A., Schmid, P.J., Henningson, D.S.: Transient growth in compressible boundary layer flow. Phys. Fluids **8**(3), 826–837 (1996). doi:10.1063/1.868864, http://scitation.aip.org/content/aip/journal/pof2/8/3/10.1063/1.868864
5. Li, F., Malik, M.R.: On the nature of pse approximation. Theor. Comput. Fluid Dyn. **8**(4), 253–273 (1996). doi:10.1007/BF00639695, http://dx.doi.org/10.1007/BF00639695
6. Andersson, P., Henningson, D., Hanifi, A.: On a stabilization procedure for the parabolic stability equations. J. Eng. Math. **33**(3), 311–332 (1998). doi:10.1023/A:1004367704897, http://dx.doi.org/10.1023/A%3A1004367704897
7. Bertolotti, F.P., Herbert, T., Spalart, P.R.: Linear and nonlinear stability of the blasius boundary layer. J. Fluid Mech. **242**, 441–474 (1992). doi:10.1017/S0022112092002453, http://journals.cambridge.org/article_S0022112092002453
8. Chang, C.L., Malik, M., Erlebacher, G., Hussaini, M.: Compressible stability of growing boundary layers using parabolized stability equations. In: 22nd Fluid Dynamics, Plasma Dynamics and Lasers Conference (1991). AIAA-1991-1636
9. Herbert, T.: Parabolized stability equations. Annu. Rev. Fluid Mech. **29**, 245–283 (1997). doi:10.1146/annurev.fluid.29.1.245, http://www.annualreviews.org/doi/abs/10.1146/annurev.fluid.29.1.245

# Chapter 3
# Linear Instability

In hypersonic boundary layers, Görtler modes show particular behaviors. When the *Re* number is not large, the synchronization which is well-known in a flat-plate boundary layer also happens. On the other hand, when *Re* is large, the competition of the multiple Görtler modes may take place. In this chapter, we make use of the classic modal stability analysis to studied the two problems.

In the local normal mode analysis, the dimensionless frequency $F$ is often introduced to remove the influence of the local boundary layer length scale thus signifying a physical frequency, i.e.

$$F = \frac{\omega^* \nu_\infty^*}{U_\infty^{*2}} = \frac{\omega}{Re} \tag{3.1}$$

The term "*global frequency*" for $F$ is adopted in this work. Similarly, the global spanwise wavenumber $B$ and curvature $K$ can be defined as

$$B = \frac{2\pi \nu_\infty^*}{U_\infty^* \lambda^*} = \frac{\beta}{Re} \tag{3.2}$$

$$K = \frac{\nu_\infty^*}{U_\infty^* r^*} = \frac{k}{Re} \tag{3.3}$$

They are related to the wavelength parameter of the Görtler vortices [1], i.e.

$$\Lambda = \frac{U_\infty^* \lambda^*}{\nu_\infty^*} \sqrt{\frac{\lambda^*}{r^*}} = \sqrt{\left(\frac{2\pi}{B}\right)^3 K} \tag{3.4}$$



J. Ren, *Secondary Instabilities of Görtler Vortices in High-Speed Boundary Layers*, Springer Theses, https://doi.org/10.1007/978-981-10-6832-4_3

## 3.1 Discrete Spectrum of the Görtler Modes

In this section, the boundary layer instabilities with spanwise wavenumbers $B = 1.0\times10^{-4},\ 2.5\times10^{-4}$ and curvature $K = 1.0\times10^{-6},\ -1.0\times10^{-6}$ are considered. The frequency is consistent with the basic case, i.e. $F = 2.2\times10^{-4}$.

Influence of the spanwise wavelength

It was shown [2] that the increase in the wave angle $\psi$ results in the decrease in the growth rate when the mode F is synchronized with the mode S. Disturbances with the constant spanwise wavelength are considered here. Typically, the spectrum with $B = 1.0\times10^{-4},\ 2.5\times10^{-4}$ are given in Fig. 3.1. Within the range of $\omega \in [0, 0.88]$, four fast modes $F^{(1)} \sim F^{(4)}$ arise from the inclined fast acoustic wave for the two cases. The phase velocity of the inclined acoustic wave is $c = 1 \pm 1/(Ma\cos\psi_i)$. Here $\psi_i$ is the wave angle of a particular mode when synchronizing with the continuous spectrum. In the case of $B = 1.0\times10^{-4}$, $\psi_{F^{(1)}} = 29.5°$, $\psi_{F^{(2)}} = \psi_{F^{(3)}} = \psi_{F^{(4)}} = 29.8°$ and

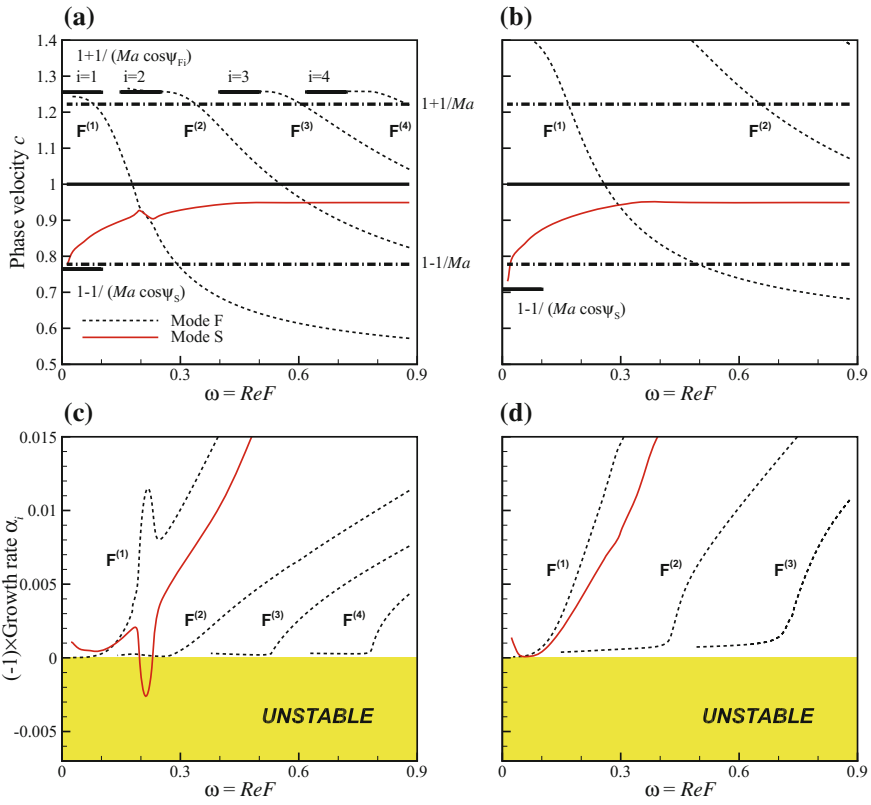


**Fig. 3.1** The phase velocity **a** $B = 1.0\times10^{-4}$; **b** $B = 2.5\times10^{-4}$ and growth rate **c** $B = 1.0\times10^{-4}$; **d** $B = 2.5\times10^{-4}$ of the discrete spectrum as a function of the angular frequency $\omega$

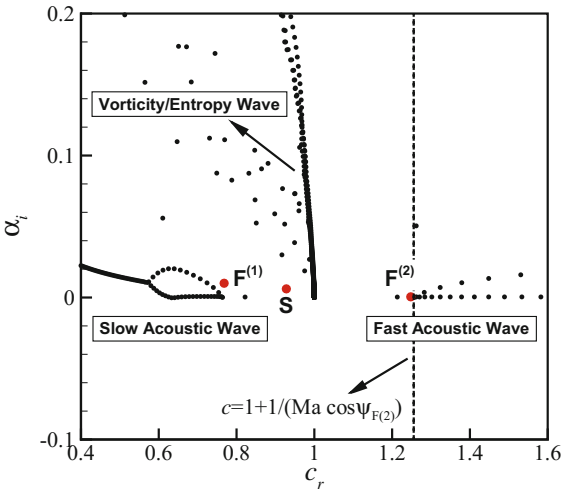


**Fig. 3.2** The discrete spectrum with mode $F^{(1)}$, $F^{(2)}$ and mode $S$ highlighted; $B = 1.0 \times 10^{-4}$, $\omega = 0.3$

$\psi_S = 20.4°$. When the wavenumber is increased to $B = 2.5 \times 10^{-4}$, the waveangles increase to $\psi_{F^{(1)}} = 58.0°$ and $\psi_S = 42.5°$. The evolution of the phase velocity of the mode F is thus influenced more greatly by the wavenumber $B$ than the mode S. Through the comparison with the basic case ($B = 0$) in Fig. 1.1, a general trend is to be expected. The growthrate of the unstable mode reduces with the increase in the wavenumber. The synchronization between the mode F and the mode S is weakened at $B = 1.0 \times 10^{-4}$ and almost disappeared when $B = 2.5 \times 10^{-4}$ which leads to the disturbance becoming stable. The spectrum of the 3-D disturbance with $B = 1.0 \times 10^{-4}$ at $\omega = 0.3$ is shown in Fig. 3.2. It is at this state that the mode $F^{(2)}$ is in the synchronization with the inclined fast acoustic wave. On the other hand, the synchronization between the mode $F^{(1)}$ and mode $S$ is finished leaving both modes stable.

Influence of the streamwise curvature

The effect of the streamwise curvature on the spectrum is shown in Fig. 3.3. The global convex (positive) and concave curvature (negative), i.e. $K = 1.0 \times 10^{-6}$ and $K = -1.0 \times 10^{-6}$, are considered. Comparing with the basic case in Fig. 1.1, the convex curvature reduces the growth rate of the mode $S$ when synchronizing with the mode $F^{(1)}$. The concave curvature in Fig. 3.3b, d shows a destabilizing effect with the unstable region enlarged and the growth rate increased. The synchronization for the mode $S$ and the mode $F^{(2)}$ is also observed in the concave case. This is actually the third Mack mode although its growth rate is negative at the present moderate Ma-number.

The phase velocity of the mode $F^{(2)}$, $F^{(3)}$... does not equal exactly to the fast acoustic wave when they synchronize with the fast acoustic wave as shown in Fig. 3.3a, b. The spectrum at $\omega = 0.22$ is given in Fig. 3.4 where the mode $F^{(2)}$,

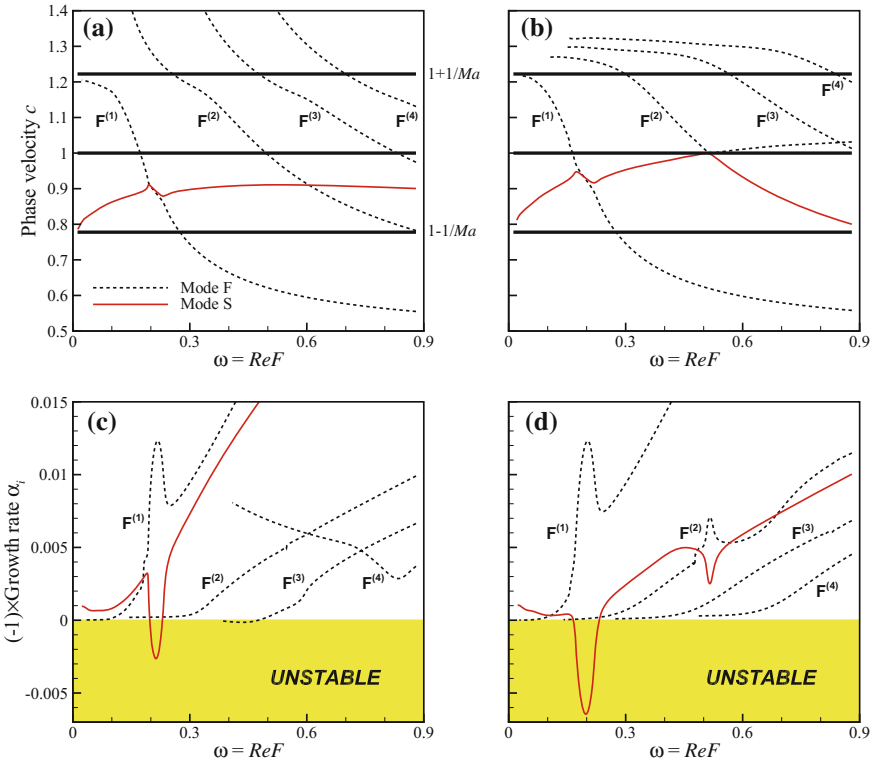


**Fig. 3.3** The phase velocity **a** $K = 1.0 \times 10^{-6}$; **b** $K = -1.0 \times 10^{-6}$ and growth rate **c** $K = 1.0 \times 10^{-6}$; **d** $K = -1.0 \times 10^{-6}$ of the discrete spectrum as a function of the angular frequency $\omega$

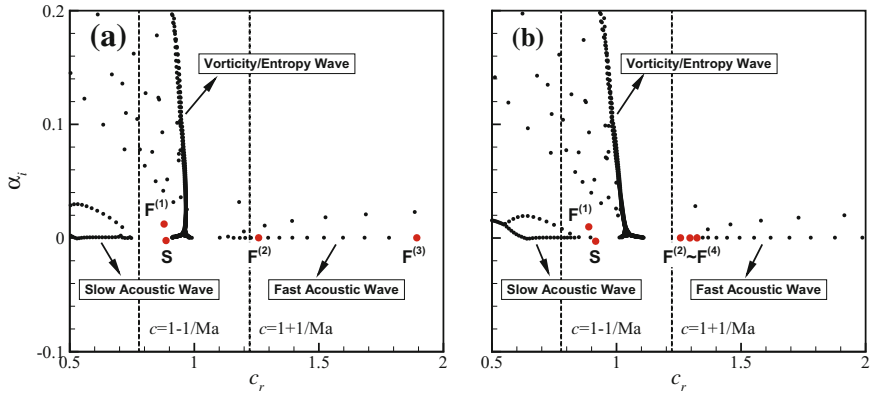


**Fig. 3.4** The discrete spectrum with mode $F^{(1)}$, $F^{(2)}$, $F^{(3)}$, $F^{(4)}$ and mode $S$ highlighted; $\omega = 0.22$; **a** $K = 1.0 \times 10^{-6}$; **b** $K = -1.0 \times 10^{-6}$

$F^{(3)}$ and $F^{(4)}$ are still in the continuous spectrum of the fast acoustic wave. The concave curvature leads to the promotion of the F modes. These modes are at the *tip* of the continuous spectrum of the fast acoustic wave in Fig. 3.4b. It is clear that these modes come from the continuous spectrum of the fast acoustic wave both for the concave and the convex conditions.

The spectrum branching which is similar to the one described in [3] is observed for the case subject to the concave curvature in Fig. 3.3b, d. The branching is related to the synchronization between the mode $F^{(2)}$ and the mode $S$. This phenomenon shows that a similar dispersion relationship also holds for the synchronization between the higher fast modes and the mode $S$.

Influence of the spanwise wavelength and the streamwise curvature: The Görtler mode

When the concave curvature and the 3-D disturbances are both considered, the unsteady Görtler modes then occurs.

The phase velocity and the growth rate of the discrete spectrum with the dimensionless frequency $F = 2.2 \times 10^{-4}$ and curvature $K = -1.0 \times 10^{-6}$ are shown in Fig. 3.5. There, the influence of the spanwise wavenumber is illustrated for $B = 2.0 \times 10^{-4}$, $2.5 \times 10^{-4}$ and $3.0 \times 10^{-4}$. For all the three wavenumbers, in the leading edge where $\omega$ is small, the discrete modes originate from the fast and slow inclined acoustic wave of the continuous spectrum. The mode S becomes unstable when the Re number is large while the fast modes are all stable. When the wavenumber $B$ is small, an obvious synchronization between the mode F and mode S is observed in Fig. 3.5a, b highlighted with the circles. Recalling Sect. 3, this synchronization becomes weaker as the wavenumber increases. This is true when the streamwise curvature is present. As a result, in the case of $B = 2.5 \times 10^{-4}$, the strong gradient of the growth rate is nearly missing. When the wavenumber is increased to $B = 3.0 \times 10^{-4}$, the synchronization totally disappears. In the current three cases, the increase in the wavenumber $B$ results in a larger growth rate of the mode S when the Reynolds number is large. In the following part of this section, all the possible synchronizations are discussed.

**Synchronization 1**. In the leading edge, the full spectrum at Re = 55 and $\omega = 0.012$ for the case $B = 2.5 \times 10^{-4}$ is plotted in Fig. 3.6. The mode F and the mode S are synchronized with the fast and slow inclined acoustic wave respectively. It should be noted that, it is the mode S that develops into the unsteady Görtler mode for all the three cases of the different wavenumbers.

**Synchronization 2**. The mode $F^{(1)}$ then synchronizes with the vorticity/entropy wave of the continuous spectrum at $\omega = 0.260$ although the expected jump of the growth rate is not discernable. The evolution of the disturbances $\hat{u}_r$, $\hat{\rho}_r$ and $\hat{T}_r$ for mode $F^{(1)}$ when synchronized with the vorticity/entropy wave of the continuous spectrum is plotted in Fig. 3.7. The disturbances are scaled to maintain unitary extreme value. In the vicinity of the synchronization region, the freestream vortic-

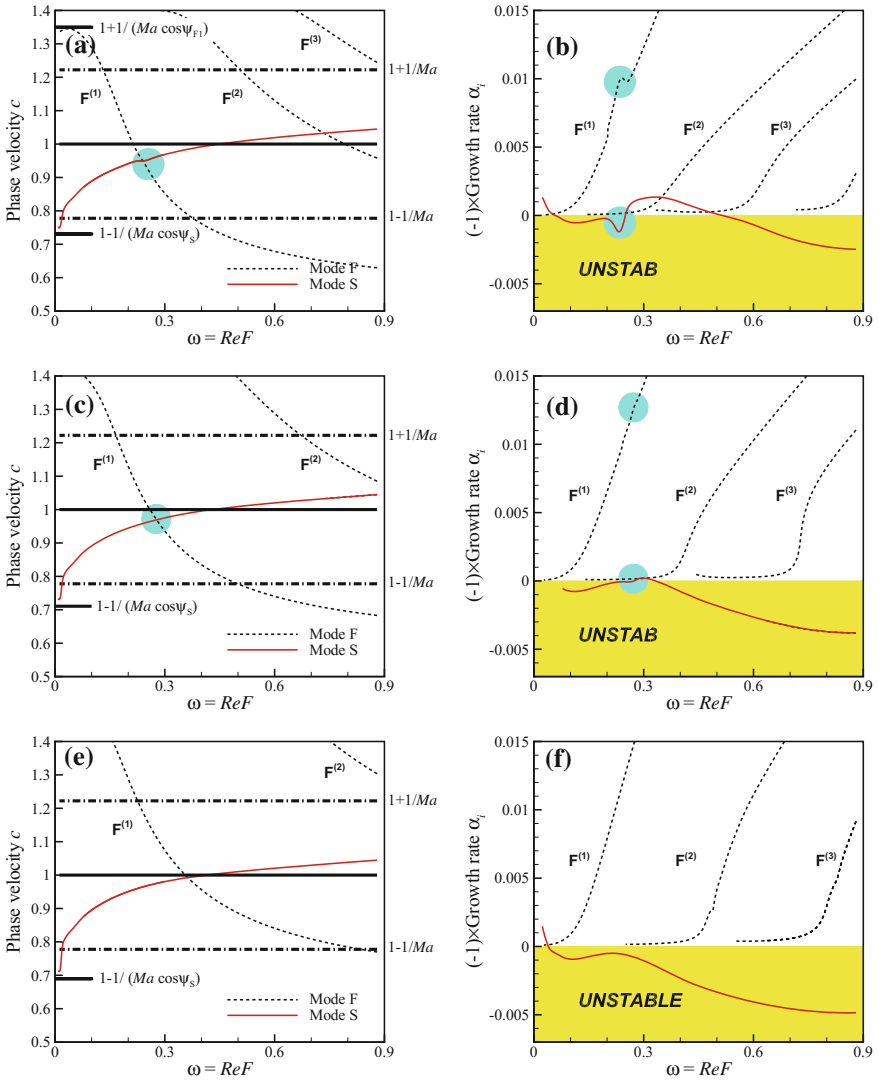


**Fig. 3.5** The phase velocity and growth rate of the discrete spectrum as a function of the angular frequency $\omega$; LST results for $F = 2.2 \times 10^{-4}$; $K = -1.0 \times 10^{-6}$. **a**, **b** $B = 2.0 \times 10^{-4}$; **c**, **d** $B = 2.5 \times 10^{-4}$; **e**, **f** $B = 3.0 \times 10^{-4}$

ity/entropy disturbances appear in the disturbance profile in the upper edge of the boundary layer. Discussions on this kind of synchronization can be found in [4, 5].

**Synchronization 3**. The synchronization between the mode $F$ and mode $S$ which give rise to the second mode over a flat plate is weakened here due to the spanwise wavenumber. The case $B = 2.0 \times 10^{-4}$ reveals the strongest synchronization. In

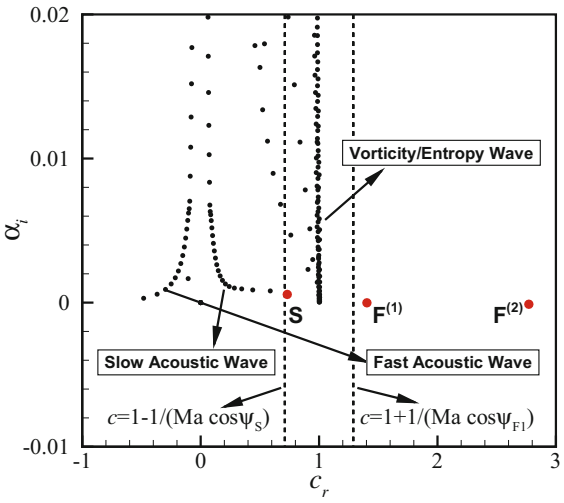


**Fig. 3.6** The discrete spectrum with mode $F^{(1)}$, $F^{(2)}$ and mode $S$ highlighted; $B = 2.5 \times 10^{-4}$, $K = -1.0 \times 10^{-6}$, $\omega = 0.012$

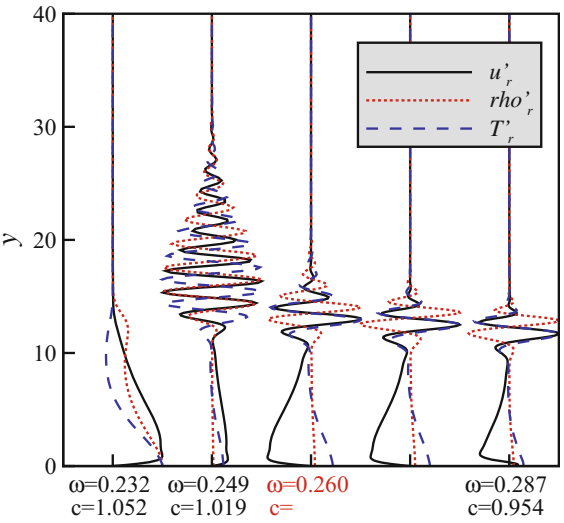


**Fig. 3.7** Evolution of the disturbances $\hat{u}_r$, $\hat{\rho}_r$ and $\hat{T}_r$ of mode $F^{(1)}$ when synchronizes with the vorticity/entropy wave of the continuous spectrum; $\omega \in [0.232, 0.287]$, $B = 2.5 \times 10^{-4}$, $K = -1.0 \times 10^{-6}$

this case, the Görtler mode(mode $S$) may be influenced when it synchronizes with the mode $F^{(1)}$ at $\omega = 0.244$. The profiles at the synchronization point for mode $F^{(1)}$ and mode $S$ are given in Fig. 3.8. The main part of the mode $F^{(1)}$ and mode $S$ have similar profiles in the section of $10 \leq y \leq 15$.

When the $Re$ number is large, as is consistent with the existing knowledge, the Görtler mode can be resolved with the normal mode analysis. This will be clarified through the comparison with the PSE for the above three cases. To specify the initial disturbances for the PSE, attention is paid to the disturbances modulated by the mode F and mode S (Görtler mode) respectively. It has been shown in Fig. 3.5

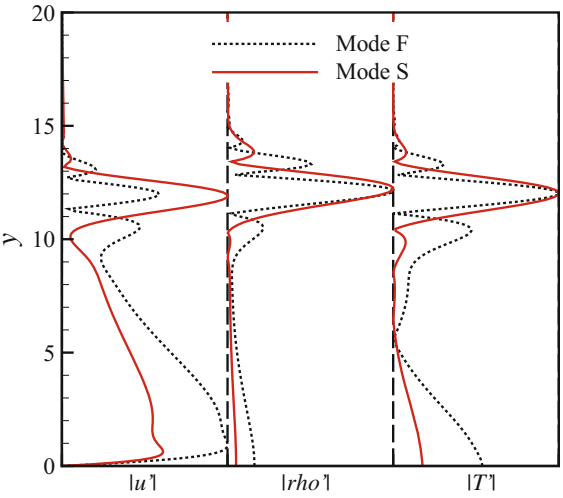


**Fig. 3.8** Disturbance profiles $|\hat{u}|$, $|\hat{\rho}|$ and $|\hat{T}|$ of mode $F^{(1)}$ and mode S; $\omega = 0.244$; $B = 2.0 \times 10^{-4}$; $K = -1.0 \times 10^{-6}$

that the mode F synchronizes with the continuous spectrum of the vorticity/entropy wave at $\omega = 0.214,\ 0.259,\ 0.356$ for the three cases. The mode F and mode S are then synchronized at $\omega = 0.240,\ 0.278$ for the first two cases. The disturbances predicted with LST at $\omega = 0.198$ are specified as the initial condition for the PSE calculation. The marching is carried out to the station $\omega = 0.440$. Different marching step sizes and grid points in the normal direction were applied and tested to give grid-independent solution.

To compare with the results given by LST, the local length scale $\delta^* = \sqrt{\nu_\infty^* x^* / U_\infty^*}$ is used for re-scaling. The evolution of the phase velocity and the growth rate is shown in Fig. 3.9. In the first two cases, the synchronization region for the mode F and the continuous spectrum of the vorticity/entropy wave has been resolved and labeled as region 1. When the phase velocity of the mode F $c_r = 1$, the synchronization occurs. This is also manifested as a drop in $\alpha_i$ of the mode F. After the synchronization in region 1, the disturbances of the mode F then synchronizes with the mode S in region 2. This is started with the intersections of the phase velocity between the mode F and the mode S. In the first case in Fig. 3.9a, b, both the phase velocities and the growth rates of the mode F and the mode S experience a remarkable change. In the second and the third case in Fig. 3.9c, e, a peak in the phase velocity is observed when the mode F tries to intersect with the mode S. After the mode F-S synchronization, the mode F finally loses its position and becomes the mode S in all the three cases. This is labeled as region 3. As shown in Fig. 3.9b, d, f, the growth rate of the mode F fluctuates around the mode S and its phase velocity approaches the mode S. In other words, the disturbances are finally modulated by the unsteady Görtler mode for both initial conditions.

In the last case, the synchronization between the mode F and the continuous spectrum of the vorticity/entropy wave is mixed with the modulation by the mode S. As also predicted with LST, the mode F-S synchronization (region 2) is missing. By

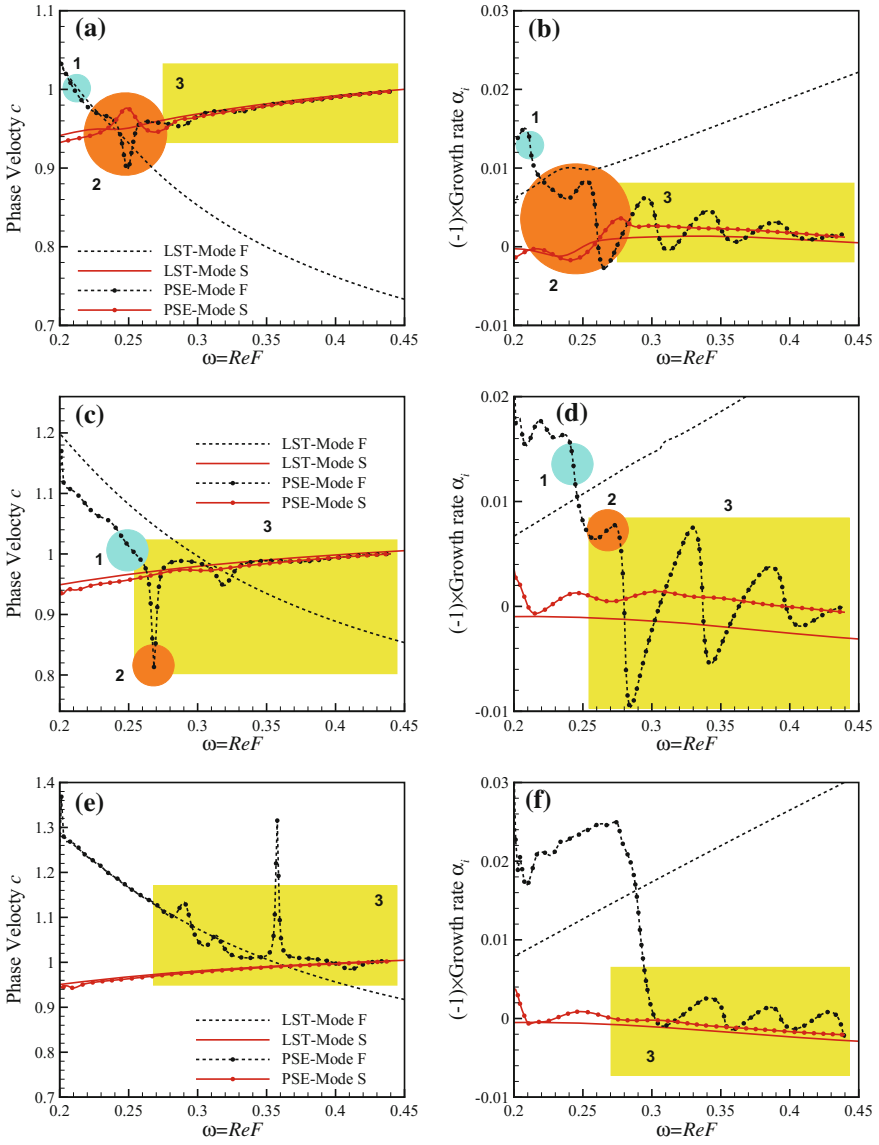


**Fig. 3.9** The phase velocity and growth rate of the discrete spectrum as a function of the angular frequency $\omega$; PSE results for $F = 2.2 \times 10^{-4}$; $K = -1.0 \times 10^{-6}$; (**a**, **b**) $B = 2.0 \times 10^{-4}$; (**c**, **d**) $B = 2.5 \times 10^{-4}$; (**e**, **f**) $B = 3.0 \times 10^{-4}$

comparing the results from LST and PSE in Fig. 3.9, we conclude that the agreement on the phase velocity of the mode S has been reached but the LST over predicts the growth rate of the mode S (Görtler mode).

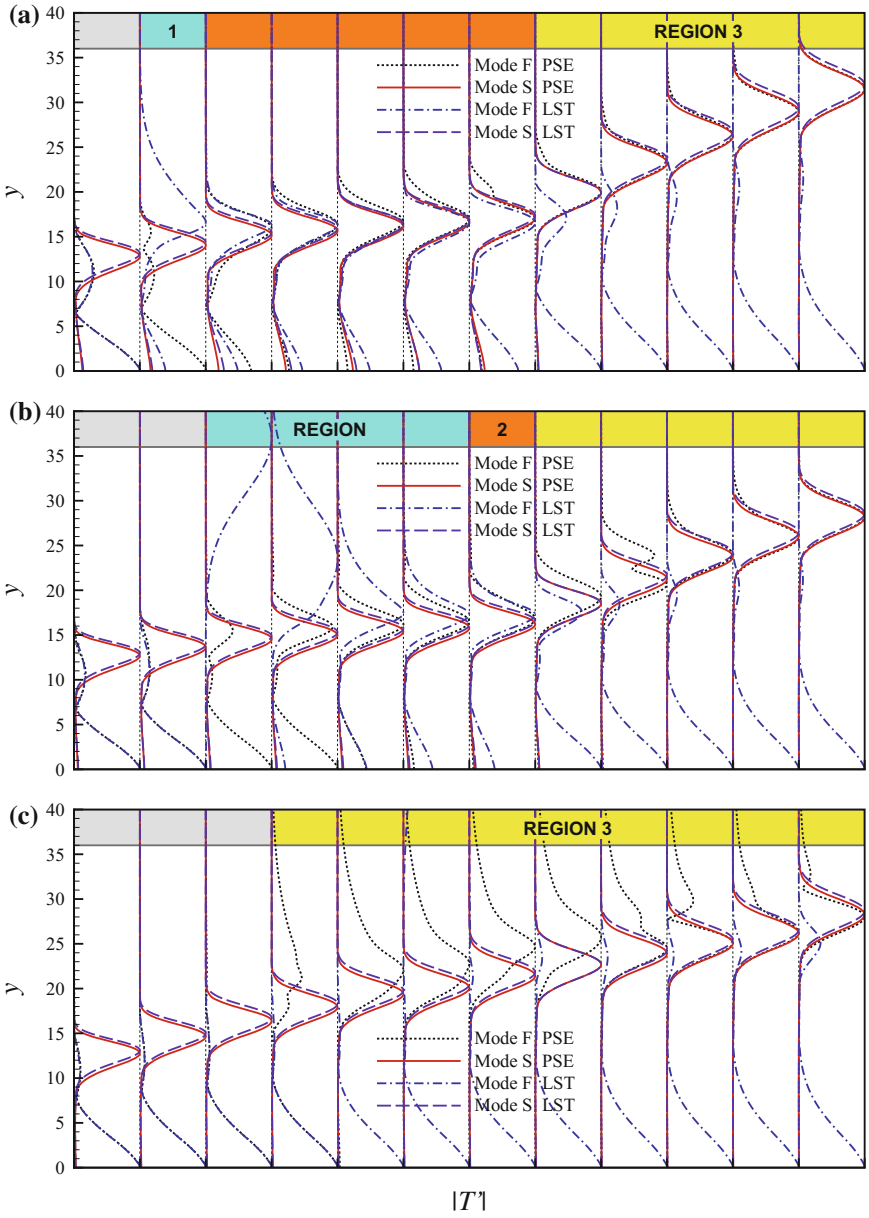


**Fig. 3.10** Evolution of the temperature disturbance of $|\hat{T}|$ for mode F and mode S predicted with LST and PSE. **a** $B = 2.0 \times 10^{-4}$; **b** $B = 2.5 \times 10^{-4}$; **c** $B = 3.0 \times 10^{-4}$

The evolution of the temperature disturbance profiles of the mode F and the mode S in the above process can be categorized in three regions as shown in Fig. 3.10. The results from the local LST analysis are also plotted for comparison. It is seen in Fig. 3.10 that before any synchronization, i.e. before the disturbances entering into Region 1, the LST and PSE give nearly identical results. In Region 1, due to the synchronization between the mode F and the continuous spectrum of the vorticity/entropy wave, the mode F in the PSE gather strength in the upper edge of the boundary layer. As a result, the disturbances in the near-wall region diminish. The local profiles of the mode F resolved with LST show major disturbances outside the boundary layer. Thus, in Region 1 a distinct difference between the LST and PSE results occurs. On the other hand, the mode S remains its shape as predicted by the two methods. Entering Region 2, where the mode F synchronizes with the mode S, the profiles of the two modes are analogous to each other. It is also in this region that the four curves almost coincide. Further downstream in Region 3, the mode F is modulated by the mode S. The PSE profiles of the mode F begin to deviate from its LST modal shapes and finally coincide with the mode S.

From the above discussion, it is clear that the unsteady Görtler mode (mode S) experienced similar synchronization process as in the flat plate. Similar to the 3-D disturbances in the flat plate, when the spanwise wavenumber $B$ is large, the mode F-S synchronization disappears.

The growth rate of the unsteady Görtler mode is sensitive to the frequency $F$. When the frequency decreases all the way to zero, the growth rate of the mode also increases to its maximum value. This is why the steady Görtler vortices are mostly considered. Here, the disturbances with the frequency $F = 1.0 \times 10^{-4}$, $1.0 \times 10^{-5}$ and $1.0 \times 10^{-6}$ are investigated as an approximation to the quasi-steady Görtler mode.

Fig. 3.11 shows the evolution of the phase velocity and the growth rate of the Görtler modes with three different frequencies. When the frequency decreases to the quasi-steady level, e.g. $F \sim 10^{-5}$, the origin of the Görtler mode also changes

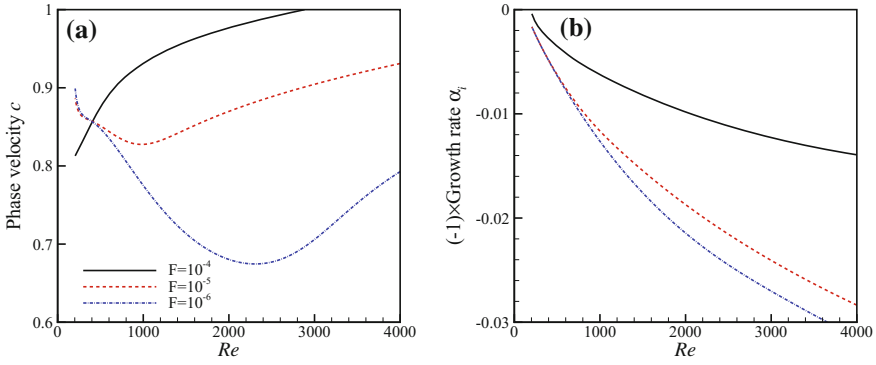


**Fig. 3.11** The phase velocity (**a**) and growth rate (**b**) of the Görtler mode as a function of the Reynolds number $R$; $F = 1.0 \times 10^{-4}$, $1.0 \times 10^{-5}$, $1.0 \times 10^{-6}$; $B = 2.5 \times 10^{-4}$; $K = -1.0 \times 10^{-6}$

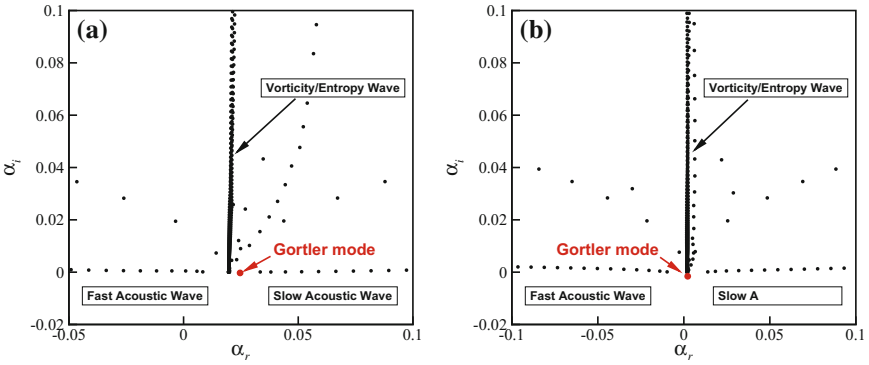


**Fig. 3.12** The discrete spectrum with the Görtler mode highlighted; $Re = 200$; $B = 2.5 \times 10^{-4}$; $K = -1.0 \times 10^{-6}$; **a** $F = 1.0 \times 10^{-4}$; **b** $F = 1.0 \times 10^{-5}$

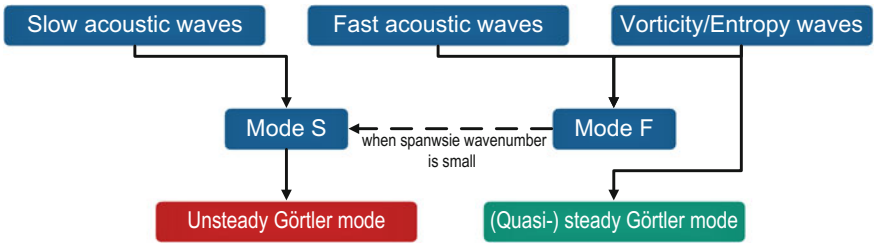


**Fig. 3.13** Scenario of the unsteady and quasi-steady Görtler mode

from the slow acoustic wave to the vorticity/entropy wave. The full spectrum at $Re = 200$ is given in Fig. 3.12 where the Görtler mode is in an initial stage. The Görtler mode with $F = 1.0 \times 10^{-4}$ originates from the slow acoustic wave at the leading edge. However, the Görtler mode with $F = 1.0 \times 10^{-5}$ can be traced to the vorticity/entropy wave. The vorticity/entropy wave is thus the leading exciter for the quasi-steady Görtler vortices. This is consistent with the results given by Whang and Zhong [6, 7].

A scenario can, therefore, be put forward in Fig. 3.13. The reader may refer to Fedorov [8] for the scenario of the Mack mode in high-speed boundary layer. The mode F originating from the fast acoustic wave synchronizes with the continuous spectrum of the vorticity/entropy wave. After the synchronization, the disturbance profile of the mode F is greatly influenced especially in the upper region of the boundary layer. The mode S originating from the slow acoustic wave finally develops into the unsteady Görtler mode. During this process, the mode S may synchronize with the mode F depending on the spanwise wavenumber. When the frequency is relatively low, i.e. a quasi-steady case, the Görtler modes are excited by the vorticity/entropy wave.

Finally, it should be pointed out that there is no definite division between the unsteady and the quasi-steady Görtler modes. A continuous variation occurs when

the frequency decreases to the quasi-steady state. Therefore, the vorticity/entropy wave shows more influence on the excitation of the Görtler mode relative to the fast/slow acoustic wave when the frequency decreases.

## 3.2 Competition of the Multiple Görtler Modes

Before the multiple Görtler modes and their effect on the flow stabilities are studied, it is important to identify each individual mode in the numerical computation and track down its behavior. The disturbance modes are related to the solutions of the eigenvalue problem. The present mode tracking approach is thus based on the crosschecking of the eigenvectors. For the wall-layer modes (mode W), the primary mode (mode W1) corresponds to the largest eigenvalue solution with one independent Görtler vortex, the secondary mode (mode W2) corresponds to the second largest eigenvalue solution with two independent Görtler vortices. This is usually the case in the incompressible problems. In the compressible boundary layer flows, however, Mach number comes into play a dominant role in addition to the $Re$ and the Görtler numbers, that sequence may be influenced by the trapped-layer mode (mode T). As will be shown later, the crossover of the mode W1 and mode T may indeed take place.

Typical case of the spectrum of the Görtler modes and their corresponding disturbances are shown in Fig. 3.14. The existing seven Görtler modes are circled against other pseudo eigenvalues. All the Görtler eigenvalues are located on the quasi-imaginary-axis, i.e. the wavenumber $Re(\alpha) \approx 0$. This is consistent with the physical phenomenon where no streamwise wave exists. The spatial structures of these modes are presented in Fig. 3.15 in the form of the streamwise perturbation

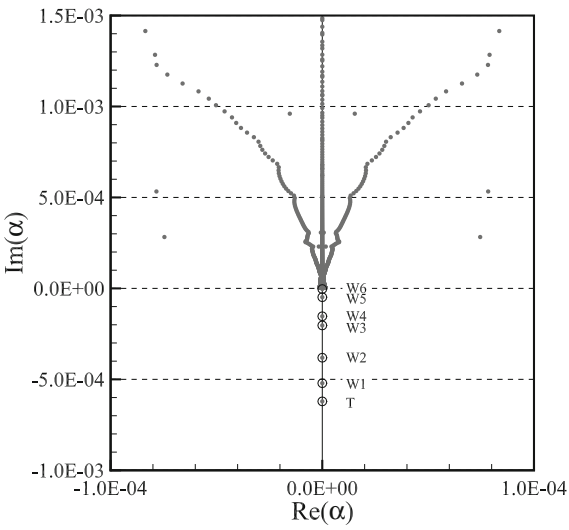


**Fig. 3.14** Eigenvalue spectrum of a typical Görtler instability. $Ma = 4, k = -10^{-6}, \beta = 1.1514, G = 954.0955$

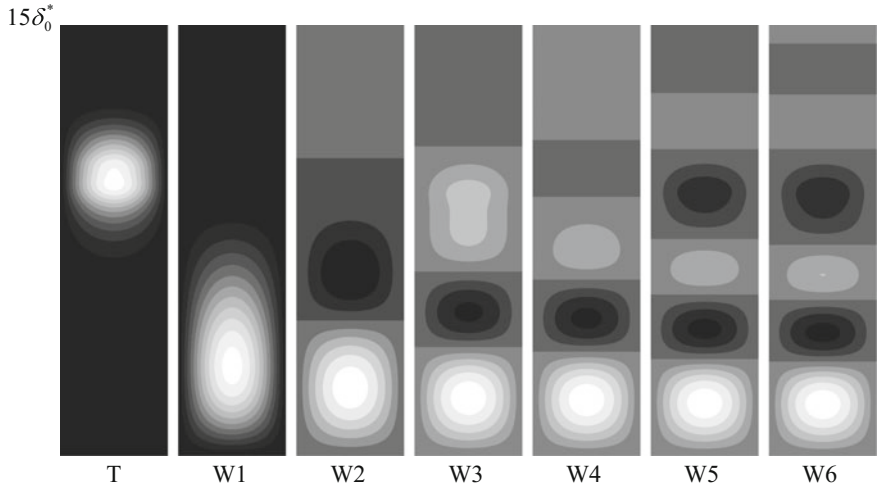


**Fig. 3.15** Contours of streamwise velocity perturbation $\hat{u}$ for the most amplified seven Görtler modes with the same control parameters as in Fig. 3.14

velocity contours. It can be inferred that the most amplified mode is mode T and the other modes are mode W1–W6.

Mode competition: The local analysis

To define a neutral curve in the $G - \beta$ map, calculations are carried out with a number of cases. Here, the curvature $k = 10^{-6}$ and Mach number $Ma = 0.95$, 2, 4 and 6 are fixed and each case is characterized with the wavenumber $\beta$ and the Görtler number $G$. Below, the contours of the disturbance growth rate for the two most amplified Görtler modes are given in Fig. 3.16. For the cases of $Ma = 0.95$ and 2, the most amplified modes are the mode W1 and W2 described with black and red lines, respectively. While in the $Ma = 4$ and 6 cases, the black lines stand for the mode T and the red lines for the mode W1. The curves with zero growth rates indicate the neutral stability curve. The results were obtained with both quasi-parallel and nonparallel base flows which are denoted with the dashed lines and the solid lines, respectively. The crossover of the contours of the growth rate for the mode T and mode W1 are observed at $Ma = 4$ and 6 when the Görtler number are sufficiently large. The switch of the dominating modes from the mode T to mode W1 is likely to influence the transition process.

Also, as shown in Fig. 3.17, a typical wavenumber is chosen as $\beta = 0.91$. The results obtained with the quasi-parallel base flows are given. The compressibility shows a stabilizing effect as the local growth rate drops with the increase of $Ma$ number. For this specified wavenumber, the initially most amplified mode T is being overtaken by mode W1 when G increases. The crossover points are denoted with the

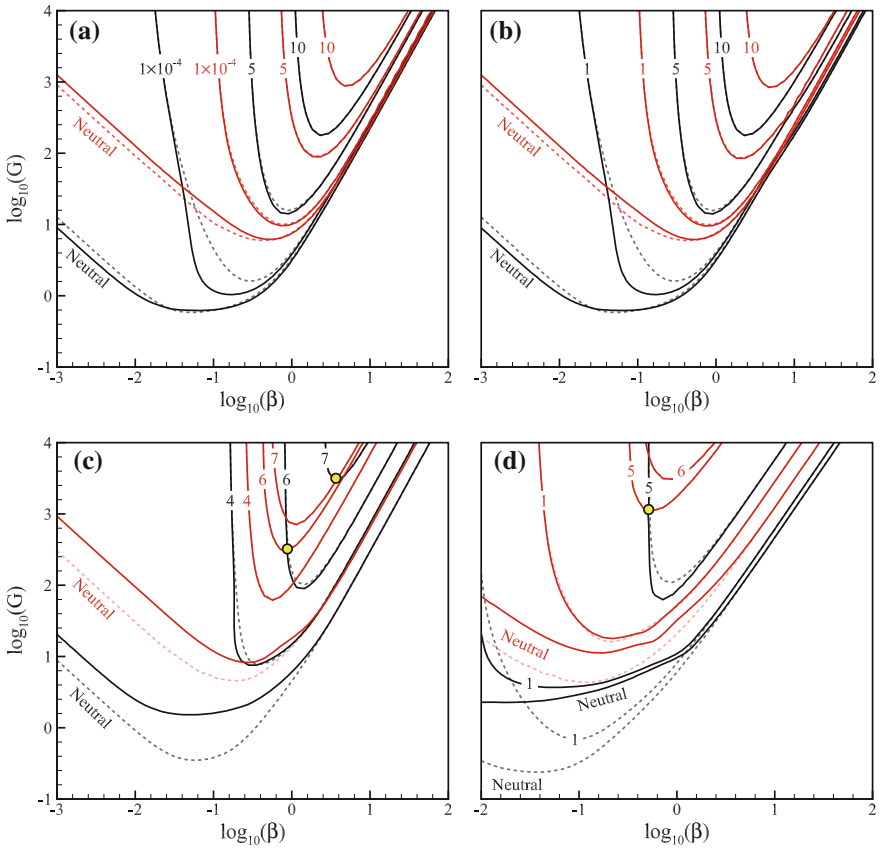


**Fig. 3.16** Contours of the disturbance local growth rate for the most amplified two modes. Labels in the figure indicate the local growth rate with a multiplier of $10^{-4}$: black line, most amplified mode, nonparallel base flow; black dotted lines, most amplified mode, quasi-parallel base flow; red line, second amplified mode, nonparallel base flow; red dotted lines, second amplified mode, quasi-parallel base flow. **a** $Ma = 0.95$; **b** $Ma = 2.0$; **c** $Ma = 4.0$; **d** $Ma = 6.0$

circles. It is interesting to note that this mode crossover takes place at the wavenumbers of the Görtler instability of practical interest.

In all the cases including low and high-speed flows with $Ma$ ranges from 0.01 to 6, as shown in Fig. 3.16, the right branch of the neutral curve is free from the influence of the parallel flow assumption. When $G$ is large enough, the nonparallel effects cease to influence the stability behavior wherever the wavenumber is located.

Before the marching analysis is performed, the normal mode solution is presented in a manner with more physical significance. Here, the dimensionless wavelength parameter $\Lambda$ is used in place of $\beta$, as it maintains the physical wavelength when marching downstream. The definition of $\Lambda$ is

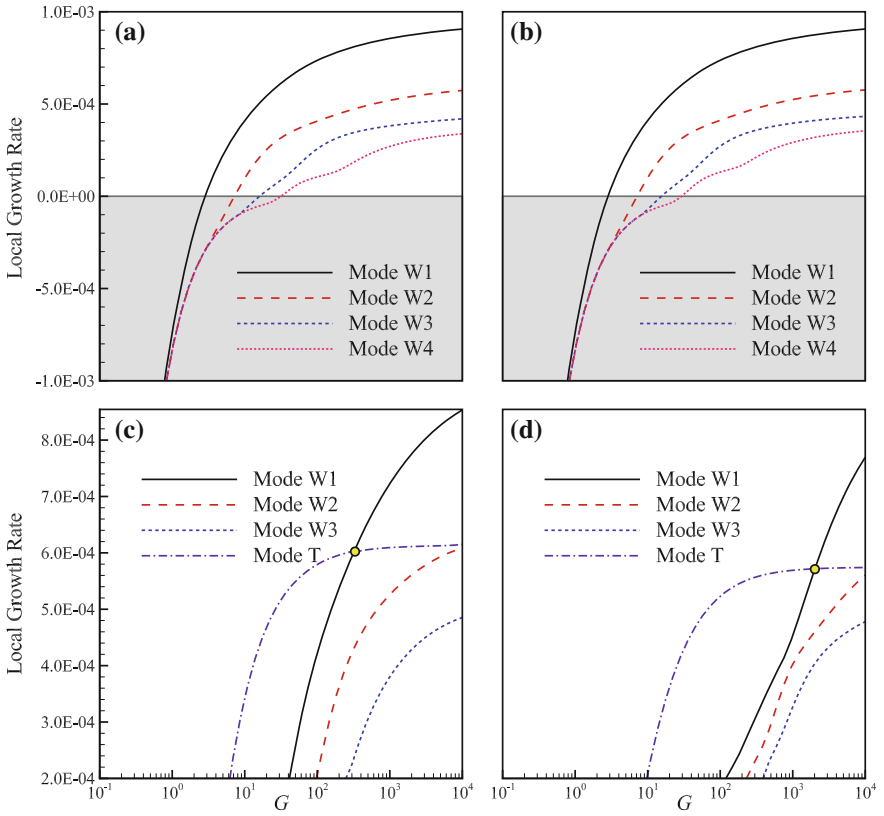


**Fig. 3.17** Local growth rate of the multiple Görtler modes at $\beta$=0.91. **a** $Ma = 0.95$; **b** $Ma = 2.0$; **c** $Ma = 4.0$; **d** $Ma = 6.0$

$$\Lambda = \frac{U_\infty^* \lambda^*}{\upsilon_\infty^*} \sqrt{\frac{\lambda^*}{R^*}} \tag{3.5}$$

The Greek letter λ stands for the spanwise wave length and $R$ for the radius of curvature. In a "Marching" view, the crossover of the two modes actually takes place for large wavelength instability as shown in Fig. 3.18. The results show little difference between the parallel and nonparallel basic flows. It is interesting and significative that the growth rate drops as $G$ increases for small wavelength cases, e.g. $\Lambda \leq 500 f$. This is essentially different from the incompressible cases [5]. In the incompressible case, the Görtler vortices are likely to fall in the range of $\Lambda \in [10^2, 10^3]$. The increase of $G$ generally helps to increase the growth rate once the disturbance wavelength is located in the amplified region. Nevertheless, in the current $Ma = 4$ and 6 case, the maximum amplification occurs within $\Lambda \in [10^2, 10^5]$. This is a much larger range within which the crossover occurs.

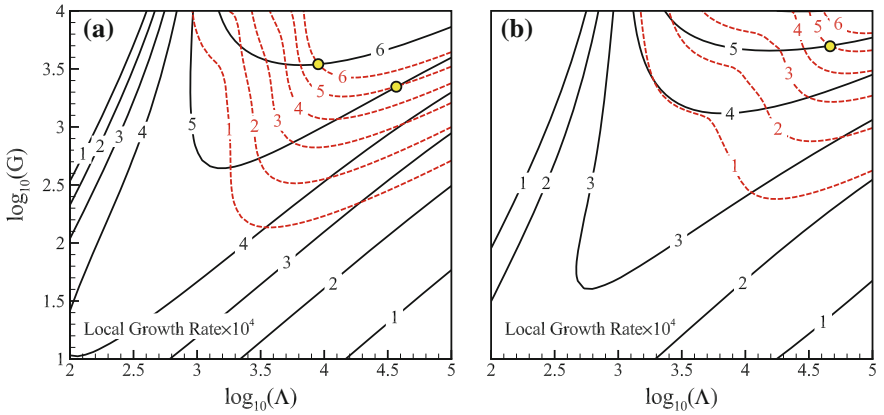


**Fig. 3.18** Contours of the disturbance local growth rate for the mode T and the mode W1 in the $G - \Lambda$ coordinates. The labels indicate the local growth rate with a magnification of $10^4$: black line, mode T; red dashed lines, mode W1; ∘, crossover point **a** Ma=4.0 and **b** Ma=6.0

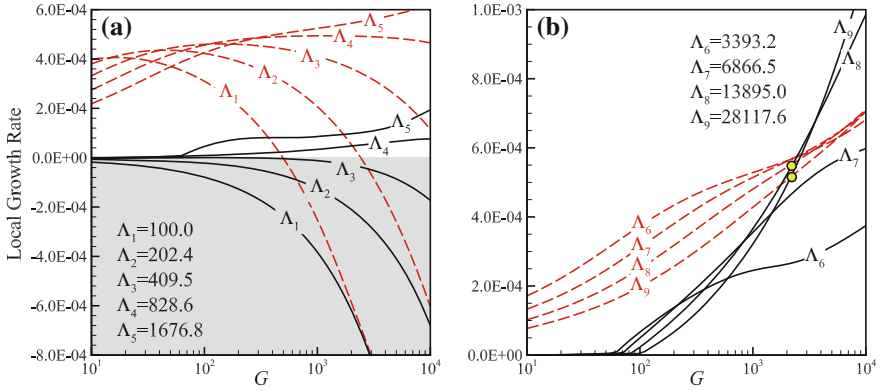


**Fig. 3.19** Local growth rate of selected wavelengths **a** $\Lambda_1 \sim \Lambda_5$ and **b** $\Lambda_6 \sim \Lambda_9$ for mode T and mode W1 with $G \in [10^1, 10^4]$, $Ma = 4$: black dotted lines, mode T; black line, mode W1; ∘, crossover point

Here, we fix some wavelengths for one of the hypersonic cases, e.g. $Ma = 4$. Growth rates of different wavelength are plotted in Fig. 3.19. The wavelength parameter ranges from 100.0 to 28117.6. It is obvious that the growth rate of mode T is always larger than mode W1 when $G$ is not too large. This is maintained till the very large wavelength case in Fig. 3.19b. Crossover of the growth rates takes place for $\Lambda_8$ and $\Lambda_9$ as shown by the circle mark in the figure.

Mode competition: The marching analysis

The marching analysis is performed for a typical wavelength corresponding to $\Lambda = 16000$. The crossover occurs at $G = 2197.8$ from the local analysis as shown in

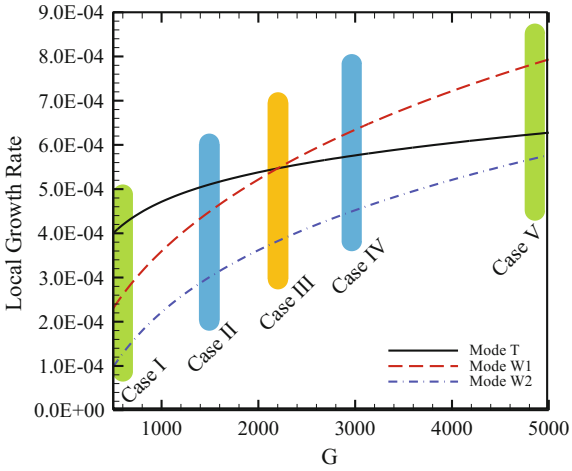


**Fig. 3.20** Local growth rate of the mode W1, mode W2 and mode T predicted by local analysis. The parameters of the five cases are given in Table 3.1

**Table 3.1** Marching parameters of the five cases defined in Fig. 3.20

| CASE | Regions | $G$ | $Re(\times 10^6)$ | $\beta$ (local scale) |
|---|---|---|---|---|
| I | T | 500–540 | 1.357–1.429 | 0.623–0.656 |
| II | T–W | 1500–1540 | 2.823–2.873 | 1.300–1.320 |
| III | W–T | 2180–2220 | 3.622–3.666 | 1.664–1.684 |
| IV | W–T | 3000–3040 | 4.481–4.521 | 2.058–2.077 |
| V | W | 4960–5000 | 6.266–6.300 | 2.878–2.893 |

Fig. 3.20. In fact, four particular regions (Region T, T–W, W–T and W) could be recognized as a prior. The following marching analysis will be performed in five cases covering these regions, respectively.

As described by Bottaro and Luchini [9], the marching and local analysis results agree well for $x$ sufficiently large. Benmalek and Saric [10], in their curvature-variation study, demonstrated that the initial conditions from the local analysis produce no quantitative dependence on the location where they are applied. To minimize the influence of the initial condition, the local profile of the disturbance is applied after the neutral point as the initial condition and the analysis is performed downstream far enough from the influence of the initial condition.

In the view point of the marching analysis, the multi-modes manifest a "single mode". The marching parameters are listed in Table 3.1. These cases can be selected a posteriori from the marching results.

Case I stands for the region far before the crossover point where the mode T enjoy the definite advantages over the other modes (Region T). As shown in Fig. 3.21a, though initialized with different modes, the disturbances all prove to be the mode T downstream. The mode W1 undergoes a temporary presence and then a "transformation" to the mode T while it is a short instant for the mode W2 to show up

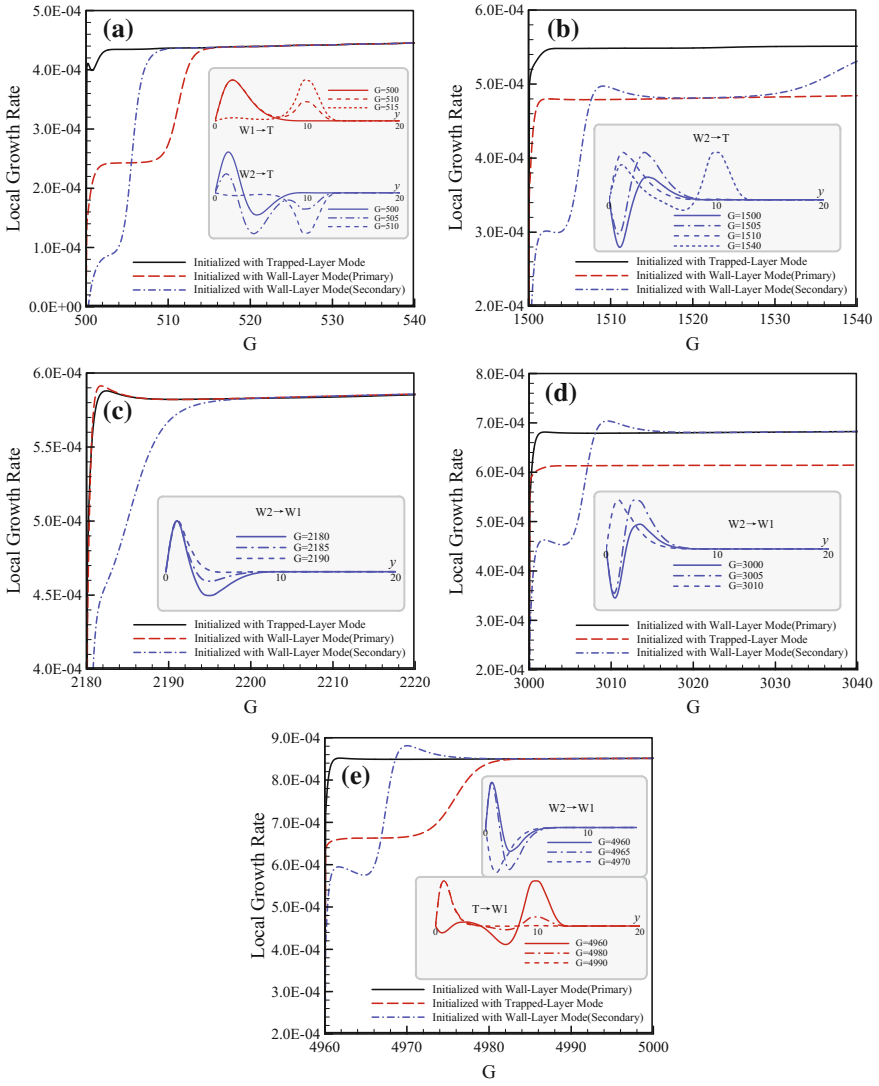


**Fig. 3.21** Local growth rate of the mode T and the mode W1 and W2 predicted by marching analysis. Evolutions of the disturbance $\hat{u}$ are given in the subplot of each figure. **a** CASE I; **b** CASE II; **c** CASE III; **d** CASE IV; **e** CASE V

its shape. Evolutions of the disturbance profile $\hat{u}$ are given in the subplot of each figure. The mode W1 has one peak and the disturbances are concentrated in the near wall region. The difference for the mode W2 is the second peak. The mode T also has one peak but the disturbances are detached from the wall. Still before the crossover point, case II shown in Fig. 3.21b supports the two modes simultaneously.

The growth rates of the two modes become closer. The mode W1 now is able to be maintained in the boundary layer. The mode W2 is "captured" by the mode W1 but finally "transformed" into the mode T (Region T–W). Case III passes through the crossover point in Fig. 3.21c. In this specific region, the growth rates of the most amplified two modes are nearly equal. As was expected, the two modes can co-exist while the mode W2 "transformed" into the mode W1 downstream which is finally the most amplified (Region T–W). In Fig. 3.21d, e, a similar process was noticed where the mode W1 overtakes the mode T (Region W–T and W).

As a matter of fact, these eigenfunctions of the modes are nonorthogonal. When the initial condition is specified with the eigenfunction of a particular mode for the marching analysis, it also covers the disturbance shape of other modes. Thus, the "transformation" is actually the appearance of the shape (mode T or W1) due to its larger growth rate. Furthermore, the initial condition derived from the normal mode approach in fact projects onto both the W and T modes.

The above marching analysis confirmed the crossover of the mode W1 and the mode T predicted by the local analysis. In the vicinity of the crossover point (Region T–W and W–T), the two modes will both have the chance to be excited and develop downstream. The other mode-shape initialized will finally develop into the shape corresponding to the most amplified mode. Further away from the crossover point, the most amplified mode will be the only survivor in the boundary layer (Region T and W). It should be pointed out that, when the nonlinear effects are considered, the crossover is not obviously influenced [11, 12].

As a practical application towards the engineering areas, the RANS modeling can be formulated based on the the linear stability theory [13]. Therefore, it is in the Region T–W and W–T discussed above that the multiple modes should be considered.

## 3.3 Conclusion

The origin of the unsteady and quasi-steady Görtler modes are explored in this article with LST and PSE approaches. The $M = 4.5$ boundary layer is chosen as the basic flow. The new terminology proposed by Fedorov and Tumin [3] are adopted in the present analysis.

The increase in the spanwise wavelength of the disturbances or the convex curvature shows a stabilizing effect on the F-S mode synchronization. However, a concave curvature promotes this synchronization. The combined effect of the 3-D disturbances and the concave curvature produces the unsteady and quasi-steady Görtler mode. When the frequency is in the order for the Mack modes, e.g. $F \sim 10^{-4}$, the mode S developed from the slow acoustic wave finally shows up as the unsteady Görtler mode. The F-S mode synchronization may also have a influence on the excitation of the unsteady Görtler mode on the condition that the spanwise wavenumber is not too large. By decreasing the frequency, the quasi-steady Görtler mode are recovered. The freestream vorticity/entropy wave plays an important role in exciting the quasi-steady Görtler vortices.

In the compressible boundary layer flows, the competition between the multiple Görtler modes is illustrated with the local and marching analyses. Eigenvalue formulation at the small wave number regime is proved to be inaccurate due to the nonparallel base flow. It can be concluded that the local method is valid either in the large wavenumber region or in the large Görtler number region. The competition between the multiple Görtler modes takes place far beyond the neutral area, i.e. the Görtler number is sufficiently large. Hence, the local analysis is valid.

Investigation into the hypersonic problems brings interesting flow features different to the convectional incompressible flows. The increase in the Görtler number even decreases the growth rate of the trapped-layer mode (mode T) when the wavelength is small. The most amplified wavelength has increased by a remarkable degree of magnitude, i.e. from $\Lambda \in [10^2, 10^3]$ to $\Lambda \in [10^3, 10^5]$. These behaviors are caused by the occurrence of the mode T in hypersonic cases, it does not exist in the incompressible flows as their modal shapes can hardly be formed. Indeed, they are even difficult to be observed experimentally. However, when $Ma$ number is increased to a certain value, i.e. $Ma \geq 4$, the mode T is the most amplified at an incipient low Görtler number. With the further increase in Görtler number, the mode W1 finally overtakes mode T and becomes the most dangerous mode. The disturbances are, therefore, modulated by different regions (Region T, T–W, W–T and W) when exposed in different Görtler numbers. It is also shown that the compressibility is to insert stabilizing effect on both mode T and mode W.

## References


1. Saric, W.S.: Görtler vortices. Annu. Rev. Fluid Mech. **26**(1), 379–409 (1994). doi:10.1146/annurev.fl.26.010194.002115
2. Ma, Y., Zhong, X.: Receptivity of a supersonic boundary layer over a flat plate. part 1. wave structures and interactions. J. Fluid Mech. **488**, 31–78 (2003). doi:10.1017/S0022112003004786. http://journals.cambridge.org/article_S0022112003004786
3. Federov, A., Tumin, A.: High-speed boundary-layer instability: old terminology and a new framework. AIAA J. **49**(8), 1647–1657 (2011)
4. Fedorov, A.V., Khokhlov, A.P.: Prehistory of instability in a hypersonic boundary layer. Theor. Comput. Fluid Dyn. **14**(6), 359–375 (2001). doi:10.1007/s001620100038
5. Federov, A., Tumin, A.: Initial-value problem for hypersonic boundary-layer flows. AIAA J. **41**(3), 379–389 (2003)
6. Whang, C., Zhong, X.: Receptivity of Görtler vortices in hypersonic boundary layers. In: 40th AIAA-2002-0151 Aerospace Sciences Meeting and Exhibit (2002)
7. Whang, C., Zhong, X.: Leading edge receptivity of Görtler vortices in a mach 15 flow over a blunt wedge. In: 41st AIAA-2003-0790 Aerospace Sciences Meeting and Exhibit (2003)
8. Fedorov, A.: Transition and stability of high-speed boundary layers. Annu. Rev. Fluid Mech. **43**, 79–95 (2011). doi:10.1146/annurev-fluid-122109-160750
9. Bottaro, A., Luchini, P.: Görtler vortices: are they amenable to local eigenvalue analysis? Eur. J. Mech. B Fluids **18**(1), 47–65 (1999). doi:10.1016/S0997-7546(99)80005-3
10. Benmalek, A., Saric, W.S.: Effects of curvature variations on the nonlinear evolution of Görtler vortices. Phys. Fluids **6**(10), 3353–3367 (1994). doi:10.1063/1.868394

11. Ren, J., Fu, S.: Multiple grtler modes in compressible boundary layer flows. In: 42nd AIAA Fluid Dynamics Conference and Exhibit. American Institute of Aeronautics and Astronautics (2012). doi:10.2514/6.2012-3078
12. Ren, J., Fu, S.: Nonlinear development of the multiple gortler modes in hypersonic boundary layer flows. In: 43rd AIAA Fluid Dynamics Conference. American Institute of Aeronautics and Astronautics (2013). doi:10.2514/6.2013-2467
13. Fu, S., Wang, L.: Rans modeling of high-speed aerodynamic flow transition with consideration of stability theory. Progr. Aerosp. Sci. **58**, 36–59 (2013). doi:10.1016/j.paerosci.2012.08.004. http://www.sciencedirect.com/science/article/pii/S0376042112000851

# Chapter 4
# Secondary Instability

## 4.1 Spatial Development of Görtler Vortices

As the steady state for secondary instabilities to set-in, the linear and nonlinear development of Görtler vortices are discussed in this section. To investigate the effect of the $Ma$ number on the secondary instability of Görtler vortices. Five groups of cases are studies here with $Ma = 0.015,\ 1.5,\ 3.0,\ 4.5$ and 6.0. The $Ma = 0.015$ case represents the incompressible flow and coincides with the experiment condition of [1]. The $Ma = 1.5$ and 3.0 cases are for moderate supersonic flows while $Ma = 4.5$ and 6.0 are for hypersonic flows. For each $Ma$ number, a number of cases with different combinations of wavenumbers $B$ and Floquet parameters $\gamma$ are considered to study the effect of the spanwise wavelength and the tuning parameter. These cases share the following flow parameters. The global curvature $K = -10^{-6}$, Reynolds number $Re \in [200, 1000]$ and thus the Görtler number $G \in [2.8, 31.6]$. The global curvature is chosen to represent the most commonly engaged Görtler flows. Recall that in the experiment of [1, 2], $K = -0.94 \times 10^{-6}$ and $-2.5 \times 10^{-6}$ respectively. The flow parameters of all the cases are listed in Table 4.1. For example, the case M3-S-B2 indicates the flow with Mach number $Ma = 4.5$, Floquet parameter $\gamma_i/\beta = 0.5$ (subharmonic) and global wavenumber $B = 1.0 \times 10^{-3}$.

In Fig. 4.1, the local growth rate of the primary Görtler modes as a function of $Re$ is given for supersonic cases. Only the most amplified mode is plotted here apart from the other sub-dominant Görtler modes. The local normal mode analysis is performed within $Re \in [200, 1000]$ locating in the post-neutral regime. The growth rate for $Re \geq 400$ (*i.e.* $G \geq 8$) can be accurately predicted with the local approach as discussed in Chap. 1. Unlike the Mack mode which grows only when the mode F synchronizes with the mode S, the unstable band of Görtler vortices is much larger [4]. They keep growing downstream until the *right-branch regime* is reached [5]. As shown in Fig. 4.1, the increase in the Mach number generally decreases the growth rate of Görtler modes, therefore, showing a stabilizing effect on the primary instability. In addition to the case B1, B2 and B3, the growth rate of another five wavenumbers are plotted with dashed lines. These wavenumbers uniformly distribute



J. Ren, *Secondary Instabilities of Görtler Vortices in High-Speed Boundary Layers*, Springer Theses, https://doi.org/10.1007/978-981-10-6832-4_4

**Table 4.1** Parameters of the flow cases in the current study. The five Mach numbers increase linearly from incompressible to hypersonic conditions. The three global spanwise wavenumber cover the (quasi-) most amplified Görtler modes in all the five Mach numbers. In the incompressible case, these wavenumbers coincide with the wavelengths 36 mm, 18 mm and 9 mm considered in [3]

| M0 | M1 | M2 | M3 | M4 |
|---|---|---|---|---|
| $Ma = 0.015$ | $Ma = 1.5$ | $Ma = 3.0$ | $Ma = 4.5$ | $Ma = 6.0$ |
| | F | S | D | |
| | $\gamma_i/\beta = 0$ | $\gamma_i/\beta = 0.5$ | $\gamma_i/\beta \in (0, 0.5)$ | |
| | B1 | B2 | B3 | |
| | $B = 0.5 \times 10^{-3}$ | $B = 1.0 \times 10^{-3}$ | $B = 2.0 \times 10^{-3}$ | |

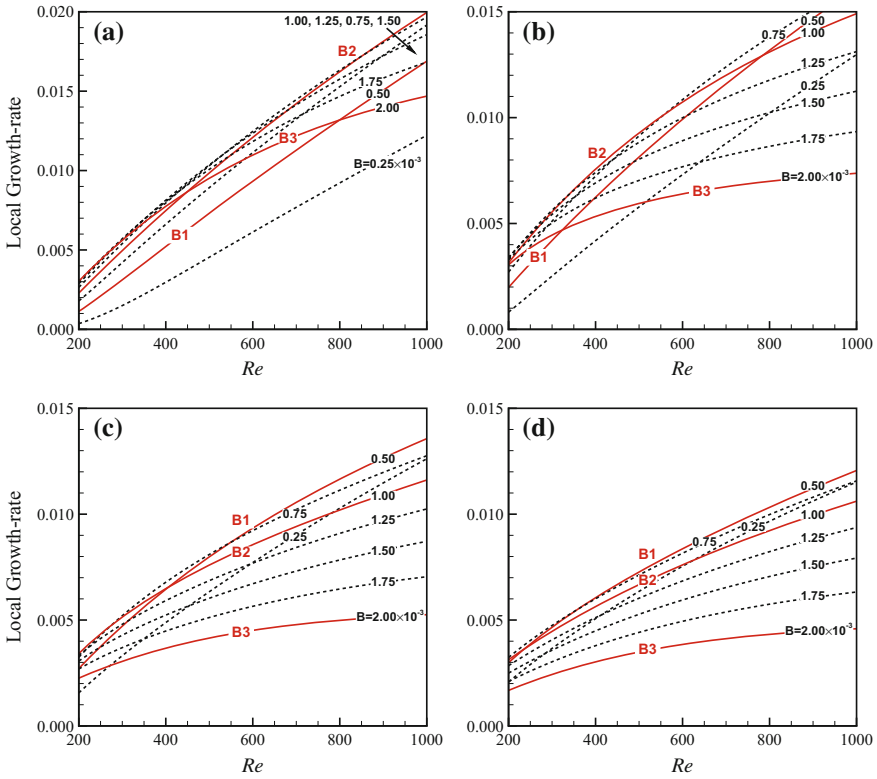


**Fig. 4.1** Local growth rate of the most amplified Görtler mode predicted with normal mode analysis. Results for eight global spanwise wavenumbers are provided (see line labels). $Re \in [200, 1000]$. **a** $Ma = 1.5$, **b** $Ma = 3.0$, **c** $Ma = 4.5$, **d** $Ma = 6.0$

within the range of $B = [0.25 \times 10^{-3}, 2.00 \times 10^{-3}]$. Integrating the growth rate within $Re \in [400, 1000]$ (not shown in the figure), the most dangerous wavenumbers are identified as $B = 1.25 \times 10^{-3}$ for case M1, $B = 0.75 \times 10^{-3}$ for M2 and $B =$

$0.50 \times 10^{-3}$ for M3 and M4. The above result shows, when the *Ma* number increases, the most dangerous wavenumber decreases. As can be inferred from Fig. 4.1, the specified three wavenumber B1= $0.5 \times 10^{-3}$, B2= $1.0 \times 10^{-3}$ and B3= $2.0 \times 10^{-3}$, by and large, cover the most amplified and also the least amplified Görtler vortices within the eight wavenumbers thus ensuring representativeness of the cases listed in Table 4.1.

As stated in Sect. 3.2, the mode T has the largest growth rate in hypersonic cases except for very large *Re* numbers. Figure 4.2 shows the modal profiles $|u'|$ $|\rho'|$ and $|T'|$ for case M1, M2, M3 and M4 at $Re = 400$ and 1000. The disturbance components $v'$ and $w'$ (not shown in the figure) have much smaller amplitudes. Nevertheless, they take the leading roles in the *lift-up* mechanism. The boundary layer edge defined as $99.99\%U_\infty$ is also plotted in the figure. The four cases have the same wavenumber B2 but the *Ma* numbers are different. The disturbances are scaled so that the streamwise velocity disturbance $|u'|$ has unit maximum value. With the increase in the *Ma* number, amplitudes of the disturbance components $|\rho'|$ and $|T'|$ become larger. The dominant component, therefore, is the temperature disturbance when $Ma \geq 3$. In moderate supersonic cases ($Ma = 1.5,\ 3.0$), the profiles of the disturbances attach the boundary layer wall while for hypersonic cases ($Ma = 4.5,\ 6.0$), all disturbance components detach from the wall. It is evident that the disturbances for $Ma = 1.5$ and $Ma = 3.0$ belong to the mode W while mode T governs the disturbances for $Ma = 4.5$ and $Ma = 6.0$ cases. The disturbances of the mode T and mode W are located within the boundary layer. The two types of Görtler mode both are steady and have zero streamwise wavenumber, *i.e.*$\alpha_r = 0$. The differences between the two modes are reflected on the Reynolds number effect as well. By increasing the Reynolds number, the modal shapes tend to become more mature. As a result, the disturbances of the mode W move towards the wall while mode T to the reverse direction when the profiles at $Re = 400$ and $Re = 1000$ are compared. It should be stressed that the crossover of the two modes [6, 7] do not occur in the present study as the *Re* number is not large enough. Therefore, the linear spatial development of Görtler vortices is governed by the most amplified mode, say, the behavior of a single mode.

With the understanding of the modal growth, the nonlinear development of Görtler vortices for the five groups of Mach numbers and three wavenumbers are performed. The initial disturbance is introduced into the boundary layer at $Re = 200$ with disturbance profiles from the normal mode analysis. The marching reaches a saturated status due to the nonlinear effects for incompressible and moderate compressible flows. In hypersonic flow, the saturation state hardly exists. This will be explained later in this section. The position of the starting point selected here causes no difference on the resulting Görtler vortices [8, 9]. The initial amplitude of the disturbances (based on the streamwise velocity disturbance) are specified as $A(u) = 2 \times 10^{-3}$ to allow sufficient linear growth (see Eq. (4.1)). The development of Görtler vortices with spanwise wavenumber B2 in the nonlinear regime for case M1, M2, M3 and M4 are provided in Fig. 4.3. The contours of the streamwise velocity $u$ are at the levels of 0.1, 0.2, ..., 0.9. Ten slices distributed within $Re \in [520, 720]$ are plotted to illustrate the rise and development of the *mushrooms*. The disturbances begin to

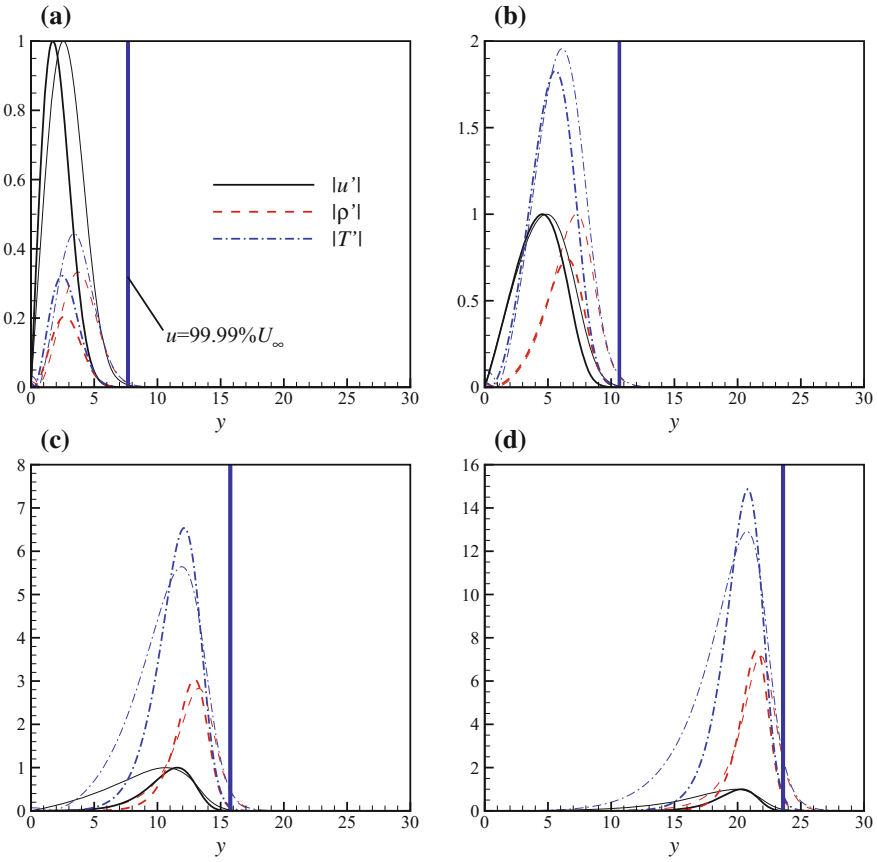


**Fig. 4.2** Disturbances profiles of $|u'|$, $|\rho'|$ and $|T'|$ at $Re = 400$ (thin lines) and $Re = 1000$ (thick lines) with the global spanwise wavenumber $B = 1.0 \times 10^{-3}$. The $|u'|$-amplitude is normalized to maintain unit maximum value. The vertical lines show the upper edge of the boundary layer defined as 99.99% of the freestream velocity. **a** $Ma = 1.5$, **b** $Ma = 3.0$, **c** $Ma = 4.5$, **d** $Ma = 6.0$

alter the profiles of the boundary layer visibly at $Re \approx 520$ where the amplitude of the disturbances reaches 5% of the base flow. The contours of the density and the temperature are analogous to the streamwise velocity in Fig. 4.3.

It is seen in Fig. 4.3 that the counter-rotating streamwise vortices carry the fluids with high momentum & low temperature towards the wall and fluids with low momentum & high temperature to the reverse direction exerting the *lift up* mechanism. The boundary layer streaks, also the thermal streaks [10], form as a result. One can observe the changes in the boundary layer due to the increase in the *Ma* number:

(1) The boundary layer thickness varies with *Ma* parabolically as $\delta_{99} \propto Ma^2$. This can be identified from the first slice of the contours in each subplot in Fig. 4.3 where the boundary layer flow starts to receive perceptible increments from the disturbances.

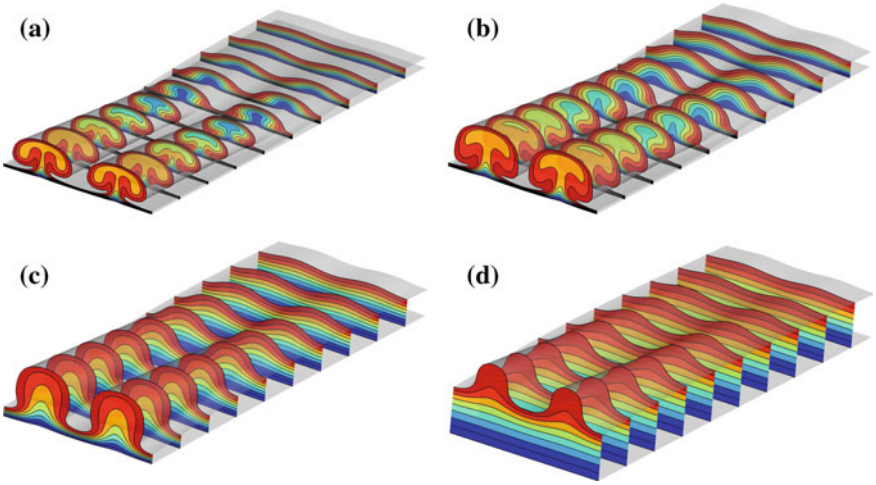


**Fig. 4.3** Nonlinear development of Görtler vortices and the formation of low- and high-speed streaks. Contour plots of the streamwise velocity are within $Re \in [520, 720]$. Contour levels $= 0.1,\ 0.2,\ \cdots, 0.9$. Global spanwise wavenumber B2=$1.0 \times 10^{-3}$. **a** $Ma = 1.5$, **b** $Ma = 3.0$, **c** $Ma = 4.5$, **d** $Ma = 6.0$

(2) Due to the reduction of the growth rate of Görtler modes as $Ma$ number increases, the *lift up* effect weakens hampering the formation of the *mushrooms*. Scrutinizing the two hypersonic cases shown in Fig. 4.3c, d, no *mushroom* is yet *matured*. Thus, the *bell* shape best describes this structure in comparison with the conventional *mushrooms* shape. This phenomenon is first reported by [11].

(3) The moderate supersonic ($Ma = 1.5$ and 3.0) and hypersonic ($Ma = 4.5$ and 6.0) cases are governed by the mode W and mode T respectively. As a result, the near-wall flows remain uninfluenced especially in the $Ma = 6.0$ case. The thickness of the boundary layer almost keeps unchanged in the interval of the *bells* for the $Ma = 6.0$ case whereas in the other cases the streamwise vortices take the high speed flows towards the wall hence reducing the thickness of the boundary layer. An unperturbed area where the boundary layer is not affected by the disturbances thus forms in hypersonic cases.

Figure 4.4 shows the nonlinear development of the amplitude of the Fourier components (based on density disturbances $\hat{\rho}$). The crossover between the base flow correction mode (mode 0) and the fundamental mode (mode 1) occurs in all the cases considered here. The start of the saturation is characterized by the flattening of the disturbance amplitude that clearly occurs for the case M1 and M2. In the region of saturation, the rapid growth of the amplitudes slows down and is replaced with the redistribution of the disturbance energy among harmonics. In fact, in the non-parallel boundary layer flows which slowly develop in the streamwise direction, the definite saturation may never exist. Comparing the four cases shown in Fig. 4.4, the saturation amplitude is not much influenced by the $Ma$ number.

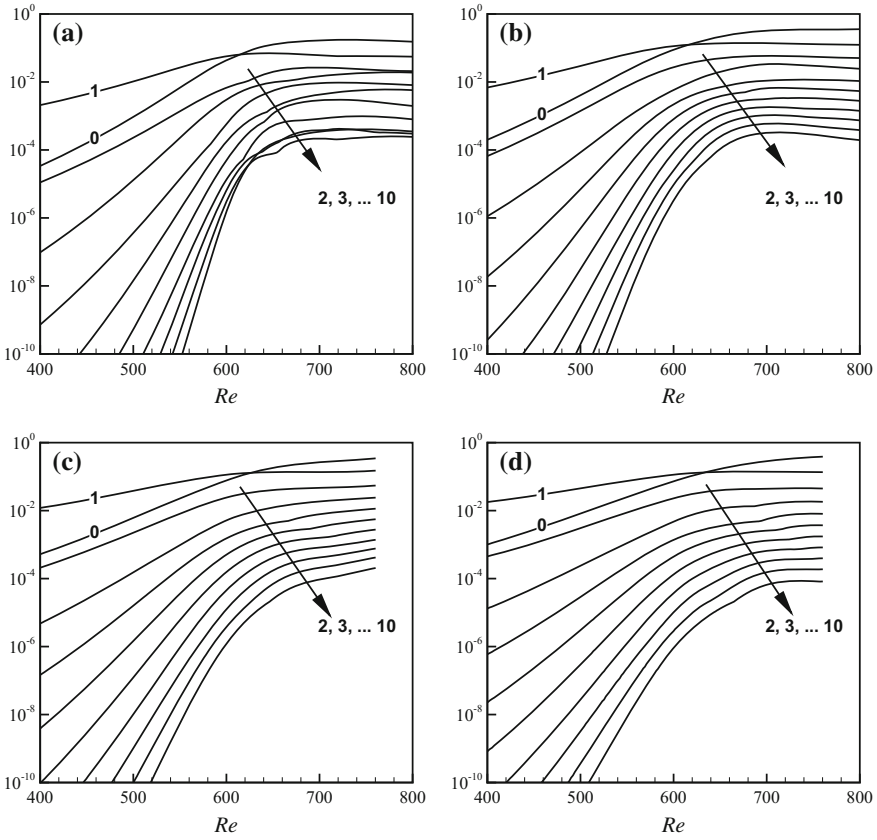


**Fig. 4.4** Development of the amplitude of the disturbances' Fourier components $\hat{\rho}_0$, $\hat{\rho}_1$,..., $\hat{\rho}_{10}$ as a function of the *Re* number. The number labeled indicates the wavenumber n of the harmonics as defined in 2.44. **a** $Ma = 1.5$, **b** $Ma = 3.0$, **c** $Ma = 4.5$, **d** $Ma = 6.0$

Following the definition introduced by [12], the streak amplitude based on the streamwise velocity disturbance is

$$A(u) = 0.5\left(\max_{y,z}(\tilde{u}) - \min_{y,z}(\tilde{u})\right) \tag{4.1}$$

For compressible flows, we also introduce the thermal streak amplitude

$$A(T) = 0.5\left(\max_{y,z}(\tilde{T}) - \min_{y,z}(\tilde{T})\right) \tag{4.2}$$

as a measure of the gradient. The amplitude of the gradient is defined as [13]

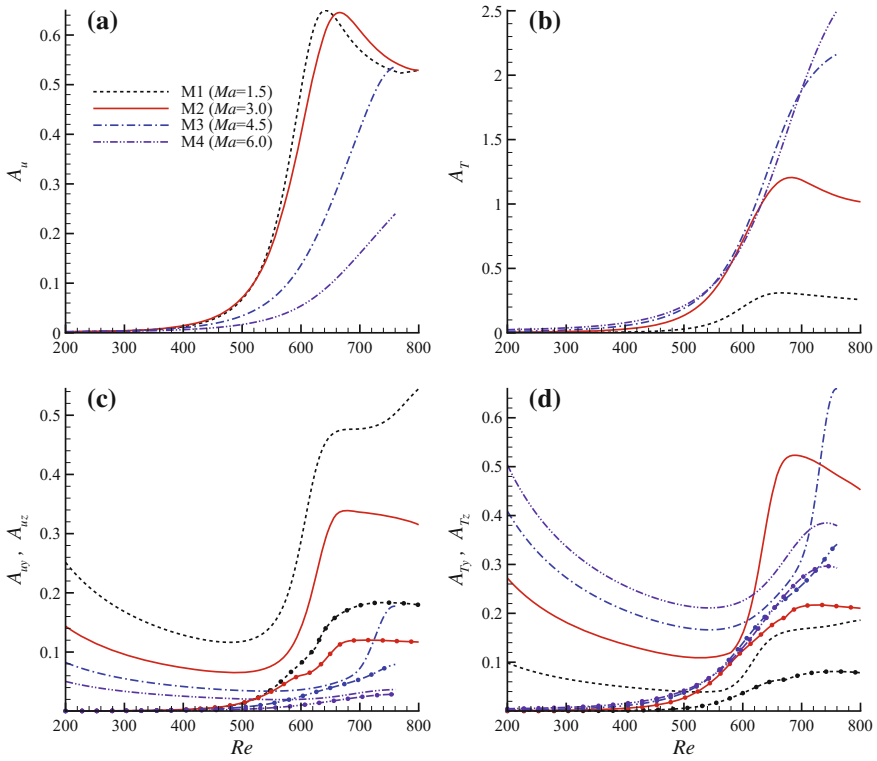


**Fig. 4.5** Spatial development of the streaks indicated with streak amplitude and gradient amplitude. $Re \in [200, 800]$; B2$= 1.0 \times 10^{-3}$; $Ma = 1.5,\ 3.0,\ 4.5$ and 6.0. **a** streak amplitude $A(u)$ based on streamwise velocity disturbance $\tilde{u}$. **b** streak amplitude $A(T)$ based on temperature disturbance $\tilde{T}$. **c** streamwise velocity gradient amplitude $A(u_y)$ (lines without symbols) and $A(u_z)$ (with solid circle symbols). **d** temperature gradient amplitude $A(T_y)$ (lines without symbols) and $A(T_z)$ (with solid circle symbols)

$$\begin{aligned} A(u_y) &= \max_{y,z} |(U+\tilde{u})_y|, \quad A(u_z) = \max_{y,z} |(U+\tilde{u})_z| \\ A(T_y) &= \max_{y,z} |(T+\tilde{T})_y|, \quad A(T_z) = \max_{y,z} |(T+\tilde{T})_z| \end{aligned} \tag{4.3}$$

In Fig. 4.5a, b, the streak amplitude $A(u)$ and $A(T)$ are plotted as functions of $Re$. The global wavenumber B2$= 1.0 \times 10^{-3}$. For the two moderate supersonic cases M1 and M2, $A(u)$ increase first and both reach a maximum value around 0.64. The amplitude $A(u)$ and $A(T)$ start to decrease in the region of saturation. For the two hypersonic cases M3 and M4, $A(u)$ keeps increasing to 0.54 and 0.24 respectively. A general trend is that the amplitude $A(u)$ decreases while $A(T)$ increases when the Mach number is increased. It's worth noting that $A(T)$ finally reaches 2.2 and 2.5 in M3 and M4 which becomes more than twice of the baseflow. As a result, the nonlinear terms become large enough which require increasingly more iterations at

each station. This creates obstacles for the governing parabolic stability equations and also for the steady development of Görtler vortices in high-speed flows. This is the reason why nonlinear marching becomes difficult to maintain and the saturation hardly exists in hypersonic cases. One can improve the situation by increasing the number of harmonics included and reducing the step size $\Delta x$ thus diminishing the differences between two steps. The marching is stopped when the *mushrooms* or *bells* (based on $A(u)$ and $A(T)$) are fully or over developed.

Fig. 4.5c, d show the amplitude of the gradients for $u_y$, $u_z$ and $T_y$, $T_z$ defined in (4.3). The lines with and without circle symbols indicate the $y$- and $z$- gradient respectively. The $y$-gradient naturally exists in undisturbed boundary and thus is not zero when the initial disturbance is introduced. Along with the development of the streak, both $A(u_y)$ and $A(T_y)$ decrease first and then increase. In the case M1 and M2, the saturation finally prevents the rapid growth of this gradient. The $z$-gradients are generally related to the sinuous secondary mode. In all the cases considered here, they keep growing until the saturation (if exists) occurs.

On the whole, the *Ma* number greatly affects the spatial development of Görtler vortices. In addition to the preceding analysis, the increase in the Mach number also brings the following changes to the primary steady states. (1) The temperature disturbance as well as the related gradients becomes the dominant component; (2) Saturation of the disturbance hardly exists in hypersonic cases due to the dramatically increase of the temperature disturbances. It can be expected that the secondary instability shall experience a very different scenario depending on the *Ma* number of the flow.

## 4.2 The Secondary Instability

The streamwise elongated streaks are receptive to the secondary disturbances when the amplitude is large enough and the secondary instability reaches the maximum growth rate near the saturation of the primary disturbances. To better understand the development of the secondary disturbances, the secondary instability analysis is performed for the fundamental, subharmonic and detuned cases at multiple locations. In this subsection, the secondary perturbations are considered at $Re = 700$.

The secondary instabilities which give rise to the high-frequency unsteady disturbances are regarded as the element factor leading to the flow transition. Due to the periodicity of Görtler vortices in the spanwise direction, the secondary instability modes can be divided into odd and even modes which determine the symmetry or antisymmetry of the disturbances. For example, for the odd modes, the secondary disturbances $\tilde{\rho}_s$, $\tilde{u}_s$, $\tilde{v}_s$ and $\tilde{T}_s$ are antisymmetric while $\tilde{w}_s$ is symmetric in the $y$-$z$ cross section. The even modes have inverse symmetry as the odd modes. The odd and even modes are, virtually, responsible for the sinuous and varicose motions of the transition process. Therefore, in this study, they are termed the sinuous and varicose modes respectively.

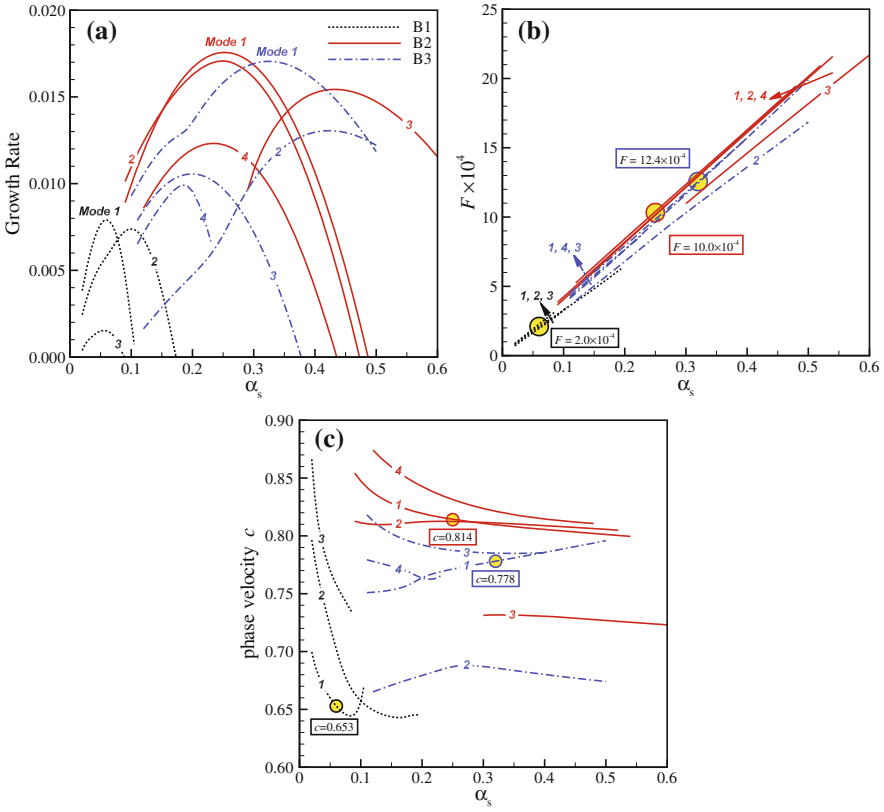


**Fig. 4.6** **a** Growth rate of the fundamental secondary disturbances as a function of the streamwise wavenumber $\alpha_s$ at $Re = 700$. Case M1-F-B1, M1-F-B2 and M1-F-B3 are shown. Say, $Ma = 1.5$, $\gamma_i = 0$, $B = 0.5$, 1.0 and $2.0 \times 10^{-3}$. The labels "Mode 1, 2, ... " indicate the ranking of maximum growth rate. The most amplified four modes (if exist) are provided. **b** Dimensionless frequency $F$ (see 3.1). The dominant frequencies $F = 2.0,\ 10.0$ and $12.4 \times 10^{-4}$ (belong to the largest growth rates) are circled for the three cases. **c** Phase velocity $c$ of the corresponding disturbances. The dominant phase velocity $c = 0.653,\ 0.778$ and 0.814 are circled

Generally speaking, a series of varicose and sinuous modes are supported by the fully developed Görtler flows. These modes become amplified within a limited range of wavenumbers or frequencies. Figure 4.6a shows the most amplified four modes (if exist) for the case M1-F-B1, M1-F-B2 and M1-F-B3 at $Re = 700$. These secondary modes are labeled as "mode 1, mode 2..." according to their maximum growth rates. As shown in the figure, there is an optimal wavenumber $\alpha_{s,opt}$ for each of the secondary mode. The growth rate decreases when the wavenumber deviates from this value. For the case B1, the growing disturbances live in a narrower band of the streamwise wavenumbers, *i.e.*$\alpha_s \in (0, 0.2)$ compared to B2 and B3 in which $\alpha_s \in (0, 0.6)$. By examining the peak growth rates of the three cases, the B2 case has the maximum growth rate followed by B3 and B1. Recalling the primary instability

shown in Fig. 4.1a, the primary instability observes the same rank as $B2 > B3 > B1$. These results show that a larger integrated primary growth and thus a higher amplitude level produces the corresponding priority for the secondary instability thus leading to an earlier flow transition that follows. It shall be noticed that some of the modes reach their peak growth rate at an obviously larger wavenumber $\alpha_{s,opt}$, *e.g.* mode 3 for case B2 and mode 2 for case B3. In fact, they are the sinuous type but have the disturbances concentrated in the *stem* of the *mushroom* which will be highlighted in this study. To distinguish, they are termed the sinuous mode type II here while the convectional sinuous modes are referred to as sinuous mode type I.

The frequency, to some extent, distinguishes the disturbance types. The dimensionless frequency $F$ of the T-S mode and the Mack second mode [14, 15], or the mode F/S in the framework suggested by [16], has a typical value of $O(10^{-4})$ [17, see, for example,]. Figure 4.6b shows the frequencies of the current secondary disturbances. They are, virtually, at the order of $O(10^{-3})$ and often termed as *high-frequency*. The varicose and sinuous mode type I with the same spanwise wavenumber $B$ (mode 1,2,3 for case B1; mode 1,2,4 for B2 and mode 1,3,4 for B3) have a very similar frequency while it is relatively smaller for the sinuous mode type II (mode 3 for B2 and mode 2 for B3). The most dangerous frequencies (belong to the largest growth rate) is $F = 2.0,\ 10.0$ and $12.4 \times 10^{-4}$ for the three cases. As shown in Fig. 4.6b, the frequencies increase almost linearly with the wavenumber $\alpha_s$ showing the phase velocities weakly dependent on the wavenumber (see Fig. 4.6c). The critical phase velocity at the maximum growth rate reads $c = 0.653,\ 0.778$ and 0.814 respectively for the three cases. The sinuous mode type II has an obviously lower phase velocity.

The contours of the streamwise velocity disturbances (absolute value, solid lines) together with the base flow (dashed lines) are plotted in Fig. 4.7 at the wavenumber $\alpha_{s,opt}$ with which they experience the peak growth rates. The most amplified three modes are provided. Both the base flow and the disturbances are normalized to have unit maximum values. The most dangerous mode (mode 1 as indicated in Fig. 4.6) for the three wavelengths B1, B2 and B3 are sinuous type I, varicose and sinuous type I, respectively.

At the same location at $Re = 700$, when the $Ma$ number is increased, the most dangerous modes are all sinuous modes as can be inferred from Fig. 4.8 showing the most dangerous modes for case M2, M3 and M4. The streamwise wavenumber corresponds to the optimal value $\alpha_{s,opt}$ of each case. Scrutinizing case M2-F-B1, M3-F-B1 and M4-F-B1, the Ma number effect is manifested by the secondary disturbances: (1) As discussed in the previous section, the transformation from mode W to mode T uplifts the streaks leaving the near-wall region unperturbed. In other words, the near-wall boundary layer flow is not much affected by Görtler vortices in hypersonic flows. The spanwise shear in the base flow, therefore, concentrates near the upper part of the boundary layer. The sinuous disturbances, consequently, shift towards the upper edge of the boundary layer as the $Ma$ number increases. (2) There are three peak values $\hat{u}_s$ for case M2-F-B1 but two for M3-F-B1 and one for M4-F-B1. This is due to the reduction in the growth rate of the primary instability

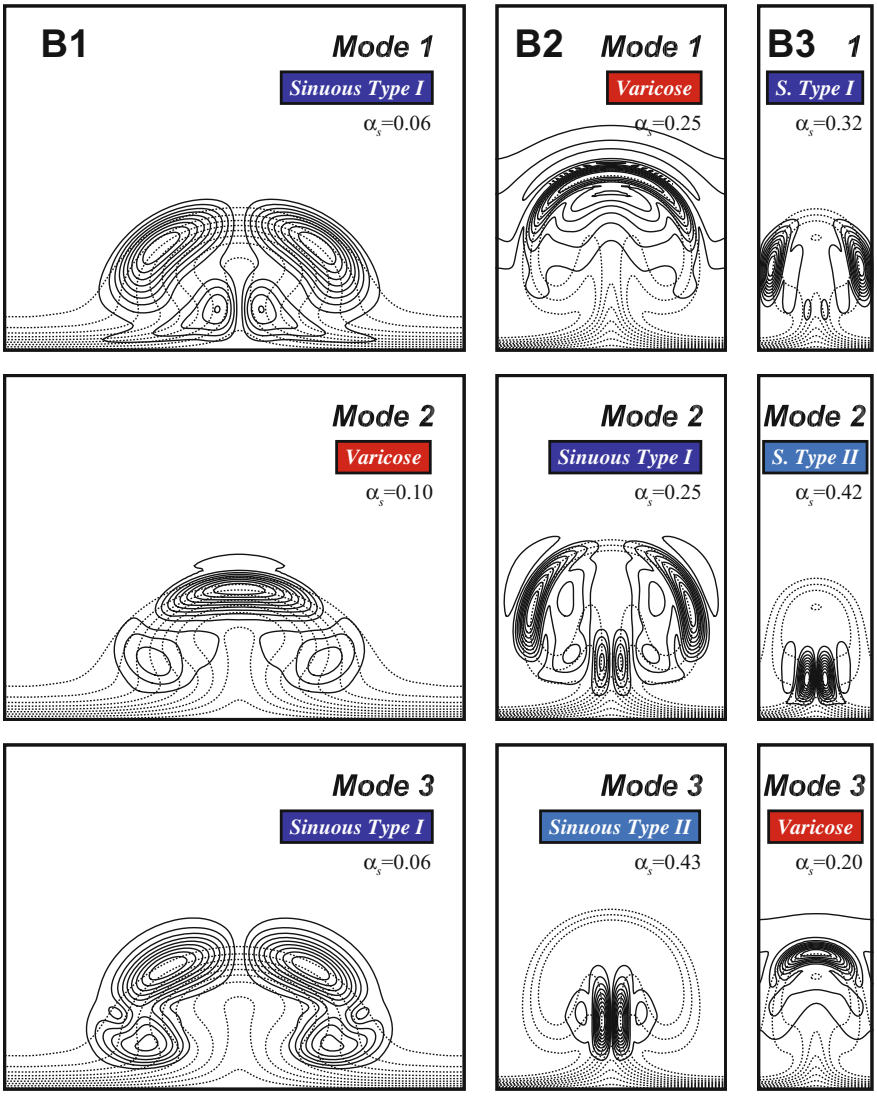


**Fig. 4.7** Fundamental secondary disturbances of the most amplified three modes for case M1-F-B1, M1-F-B2 and M1-F-B3 at $Re = 700$. Contours of the streamwise velocity disturbance $|\hat{u}_s(y, z)|$ (solid lines) and the base flows (dashed lines). Contour levels $= 0.1,\ 0.2, \cdots, 0.9$. Disturbances subject to the wavenumbers $\alpha_s$ which is the optimal values $\alpha_{s,opt}$ at peak growth rates as labeled in each subfigure. "Mode 1, Mode 2 and Mode 3" correspond to the ranking shown in Fig. 4.6

which leads to the retrogress of the *mushroom*. The distortion of the base flow is thus weakened. Further more, in M3-F-B3 and M4-F-B3, there is indeed no unstable modes as the streak is too weak.

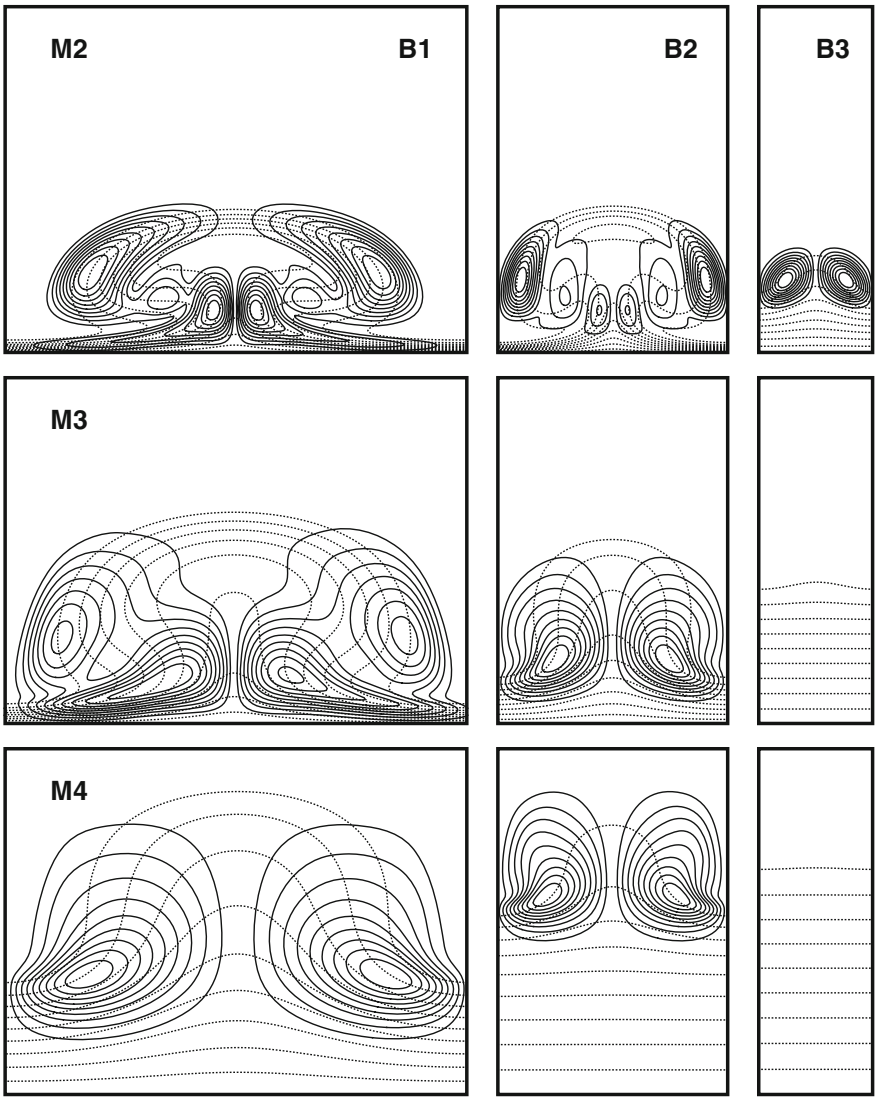


**Fig. 4.8** Secondary disturbances of the most amplified modes for case M2, M3 and M4 with wavenumbers B1, B2 and B3 at $Re = 700$. Contours of the streamwise velocity disturbance $|\hat{u}_s(y, z)|$ (solid lines) and the base flow (dashed lines). Contour levels $= 0.1,\ 0.2, \cdots, 0.9$. Disturbances subject to wavenumbers $\alpha_s$ which is the optimal values $\alpha_{s,opt}$ at peak growth rates

The above analysis is based on a single location corresponding to $Re = 700$. To highlight the effect of Mach number $Ma$ and wavenumber $B$, results of multiple streamwise locations are summarized in Fig. 4.9. Here, the growth rate at seven streamwise locations in the (quasi-) saturated regime are given for case M0, M1, M2

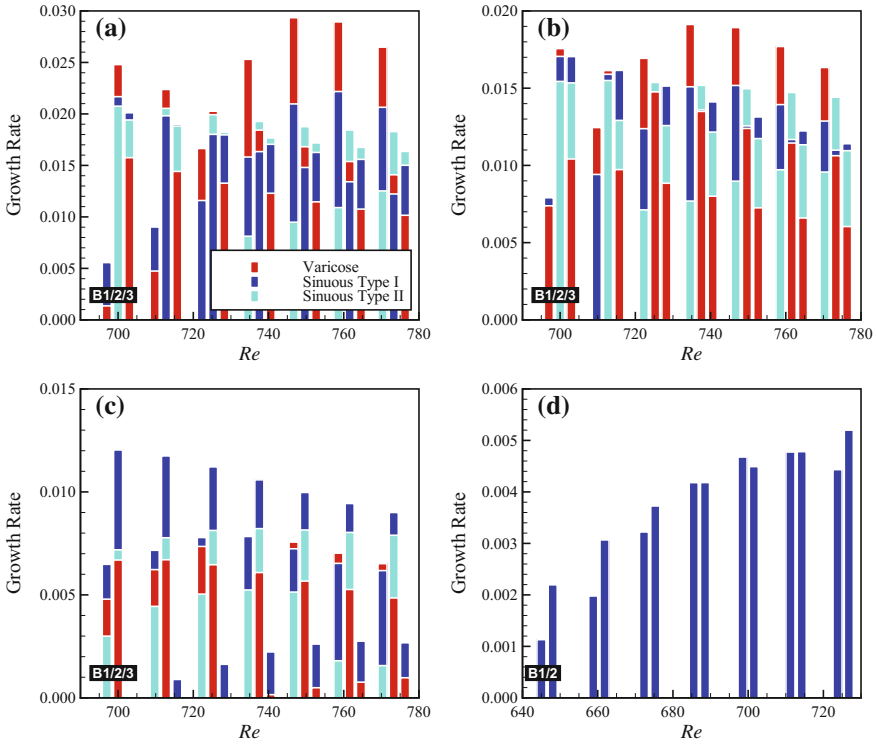


**Fig. 4.9** Growth rates of the secondary disturbances for incompressible, moderate supersonic and hypersonic cases. **a** M0, **b** M1, **c** M2 and **d** M3. Seven streamwise coordinates with $Re =$ 700, 713, 726, 738, 750, 762 and 773 are specified for case M0, M1 and M2 while $Re =$ 647, 660, 674, 687, 700, 713 and 725 for case M3. The growth rate is give by the upper bound of the bar with a certain color. The red, dark blue and light blue bars denote the varicose mode, sinuous mode type I and sinuous mode type II respectively (see also the legend). In the case M3, only the sinuous mode type I exists. Three groups of wavenumbers B1, B2 and B3 (for case M3 only B1 and B2) are shown next to each other as labeled in the left bottom of each subfigure

and M3. The three most dangerous modes, *i.e.*the varicose mode, sinuous mode type I and sinuous mode type II appear in M0, M1 and M2. In case M3, only the sinuous mode type I exists.

Although high-speed flows are of main interests here, discussions are first given for case M0. Recalling the incompressible study by [3], they showed that the even mode dominated for large wavelengths while the odd mode was more severe for small wavelengths. The conclusion came from the stability analysis up to $x = 1.0$ m. Within this range, the 18 mm (B2) and 36 mm (B1) wavelength cases had larger growth rates with the even mode while the most dangerous mode in the 9 mm (B3) case was the odd mode. In the experiment (the spanwise wavelength $\approx$18 mm, case B2), both the sinuous and varicose motions arose during the transition process [1, see, Fig. 14]. The sinuous mode is more frequently produced. According to the analysis

given by [3], for this B2 case, the varicose mode had a comparable growth rate to the sinuous mode but maintained the maximum growth rate when the Reynolds number was large. In a recent study, [18] revisited the B2 case and realized that the sinuous mode type II was missing in their studies. The sinuous mode type II do exist under experimental condition. But its growth rate is less than the most dangerous mode (varicose mode) [18]. The growth rate of the sinuous mode type II exceeds the varicose mode downstream ($x > 120$ cm) which falls outside the scope of the experimental measurement. In the experimental observation, most of the streaks start to breakdown at around $x = 100$–$120$ cm burying the sinuous mode type II. It will be elucidated here that this mode can have the largest growth rate downstream and may be responsible for the sinuous transition. For case M0-F-B2, the varicose mode has a larger growth rate than the sinuous mode type I but eventually loses out to the sinuous mode type II from $Re = 725$. It should be emphasized that, besides the growth rate from the Bi-Global stability analysis, receptivity to secondary disturbances [19] and the transient growth (multi-mode behavior), can influence the outcome of the transition process as well. This provides more interesting topics for future studies. As a result, it is not common that two adjacent streaks breakdown at the same time. Some of the streaks remain stable as can be found in [1]. It can be deduced that the sinuous mode II must have a dominant influence on the streaks which become unstable downstream.

For the other two wavenumbers, case M0-F-B1 is initially dominated by the sinuous mode type I and finally the varicose mode has a considerable advantage. The sinuous mode type II (followed by sinuous mode type I) dominates the case M0-F-B3. In short, the conclusion drawn by [3] reappears in Fig. 4.9a either if the sinuous mode type II is neglected or the flow condition is limited to the experiment condition.

In the compressible case with low Mach number, *i.e.*case M1 in Fig. 4.9b, it is evident that the varicose mode is stronger at small wavenumbers while the sinuous mode takes over at large wavenumbers. This is demonstrated as case M1-F-B1, M1-F-B2 and M1-F-B3 are governed by the varicose mode, sinuous mode type II and sinuous mode type I, respectively. When the Mach number is increased to 3.0, *i.e.*case M2 in Fig. 4.9c, the varicose mode is losing competitive edge for the wavenumber B1. Evaluating all the three wavenumbers, the overall disturbances fall into the control of the sinuous mode type I. The sinuous mode type I indeed becomes the only existing growing mode in case M3 (Fig. 4.9d) and M4 (not shown). Figure 4.9 also illustrates the reduction of the secondary growth rate by increasing the Mach numbers. The stabilizing effect of the Mach number is justified both for the primary, secondary instabilities and hence the flow transition.

The dimensionless frequency $F$ of the dominate disturbance for wavenumber B2 is provided in Table 4.2. Increase in the Mach number reduces this dimensionless frequency. As also shown in Fig. 4.6, mode S-II has a considerably larger frequency as this mode achieves its maximum growth rate at a larger wavenumber $\alpha_s$.

Scrutinizing the sinuous mode type II, it exists in incompressible (M0) and moderate compressible cases (M1 and M2). For the cases evaluated herein, this mode has actually the largest growth rate for the cases M0-F-B2, M0-F-B3 and M1-F-B2

**Table 4.2** Dimensionless frequency $F$ of the dominant disturbance for wavenumber B2 multiplied by $10^4$. The seven Reynolds number are the same as in Fig. 4.9. The type of the secondary mode is given in the brackets

| Index of $Re$ | M0 | M1 | M2 | M3 |
|---|---|---|---|---|
| 1 | 12.0 (V) | 10.2 (V) | 7.4 (S-I) | 3.0 (S-I) |
| 2 | 12.2 (V) | 10.6 (V) | 8.1 (S-I) | 3.1 (S-I) |
| 3 | 12.3 (V) | 16.3 (S-II) | 8.4 (S-I) | 3.1 (S-I) |
| 4 | 19.1 (S-II) | 16.1 (S-II) | 8.7 (S-I) | 3.1 (S-I) |
| 5 | 18.8 (S-II) | 16.0 (S-II) | 8.5 (S-I) | 3.1 (S-I) |
| 6 | 18.1 (S-II) | 15.6 (S-II) | 8.6 (S-I) | 2.9 (S-I) |
| 7 | 17.6 (S-II) | 15.2 (S-II) | 8.4 (S-I) | 2.9 (S-I) |

in the saturated regime. Thus, the sinuous mode type II must be closely watched as it can play a very important role in the transition process for subsonic and moderate supersonic flows.

[13] formulated a relation between the frequency $\omega$ or the wavenumber $\alpha_s$ with the amplitude $A(U_z)$. In the present study, a similar relation is also proposed up to moderate compressible flows for both types of sinuous modes partly reflecting the characteristics of the secondary instability. The scaling with wavenumber B2 is provided below:

$$\frac{A(U_z)}{\omega_i(\alpha_{s,opt})} = \begin{cases} 0.88 \pm 0.06 & \text{M0, sinuous mode type I} \\ 0.84 \pm 0.04 & \text{M1, sinuous mode type I} \\ 0.75 \pm 0.06 & \text{M2, sinuous mode type I} \\ 0.57 \pm 0.03 & \text{M0, sinuous mode type II} \\ 0.58 \pm 0.02 & \text{M1, sinuous mode type II} \\ 0.62 \pm 0.03 & \text{M2, sinuous mode type II} \end{cases} \tag{4.4}$$

The values here for the incompressible case are less than 1.2 as given by [13]. One reason is that different initial amplitudes and different $x$ coordinates are considered. Here, the relationship derived is based on the seven positions at $Re \approx 700, 713, 725, 738, 750, 762, 773$ (in the saturated regime) where $A(U_z)$ reaches a quasi-constant state (see Fig. 4.5c). In fact, we find $A(U_z)/\omega_i(\alpha_{s,opt})$ decreases slowly with $Re$. Therefore, this ratio must be given together with the parameters ($Re$, $Ma$, initial condition) provided.

In hypersonic cases (M3 and M4), no such a simple relation can be found. Recalling Fig. 4.5c, d, one observes that $A(T_z)$ becomes the dominant spanwise gradient when $Ma \geq 3$. This is most probably due to the emerging influence of the temperature/density gradients when Mach numbers is increased (see also Sect. 4.1).

Table 4.3 summaries the most dangerous modes (with regard to the integrated secondary growth rates in the (quasi-) saturated regime) of the fundamental secondary

**Table 4.3** The dominating (fundamental) secondary instability modes. The letter 'V', 'S-I' and 'S-II' indicate the varicose mode, sinuous mode type I and sinuous mode type II

| CASE | M0 | M1 | M2 | M3 | M4 |
|---|---|---|---|---|---|
| B1 | V | V | S-I | S-I | S-I |
| B2 | S-II | S-II | S-I | S-I | S-I |
| B3 | S-II | S-I | S-I | / | / |

**Table 4.4** Neutral conditions of the secondary instability modes measured by the streak amplitude $A(u)$. Spanwise wavenumber $B = 1 \times 10^{-3}$

| Mach number | Sinuous-I | Sinuous-II | Varicose |
|---|---|---|---|
| $Ma = 0.015$ (M0) | 28% | 59% | 41% |
| $Ma = 1.5$ (M1) | 31% | 63% | 45% |
| $Ma = 3.0$ (M2) | 31% | 63% | 44% |
| $Ma = 4.5$ (M3) | 9% | / | / |
| $Ma = 6.0$ (M4) | 5% | / | / |

instabilities for the $Ma$ number and wavenumber investigated. The letter V indicates the varicose mode. S-I and S-II are for the sinuous mode types I and II, respectively. The relationship between the dominant modes (sinuous or varicose) and the spanwise wavenumber put forward by [3] therefore holds only when the Mach number is not large even if the sinuous mode type II is ignored. For high-speed flows (in this study $Ma > 3$), the sinuous mode always has a larger growth rate.

Neutral conditions for the five Mach numbers are obtained in Table 4.4. Results are based on the spanwise wavenumber $B = 1 \times 10^{-3}$. The critical streak amplitude $A(u) \approx 28\%$, 59% and 41% for the sinuous mode type I, II and the varicose mode respectively in the incompressible case (M0). This is close to but larger than the values given by [12] (26% and 37% for sinuous and varicose modes respectively). The reason for this inconsistency could be the followings. (1) The primary state of the streak is not exactly the same. The Görtler mode and the Klebanoff mode, though similar, never possess an identical profile. Initial conditions are not the same either. Differences accumulate and feature the spatial development of the streaks. (2) Though $A(u)$ is a commendable measure of the streak amplitude, it does not tell the whole story through which the shape of the streak is hidden.

In the moderate supersonic cases considered (M1, M2), the critical amplitude $A(u)$ is increased compared with the M0 case. Interestingly, the amplitude is almost identical for the M1 and M2 cases showing that it is the *kinetic streak* that governs the neutral condition in moderate supersonic flows. On the other hand, in hypersonic cases, the critical amplitude is reduced to 9% and 5% for M3 and M4, respectively. Recall Sect. 4.1, a primary feature in hypersonic cases is the significant increase in $A(T)$ and decrease in $A(u)$ highlighting the importance of the *thermal streak*.

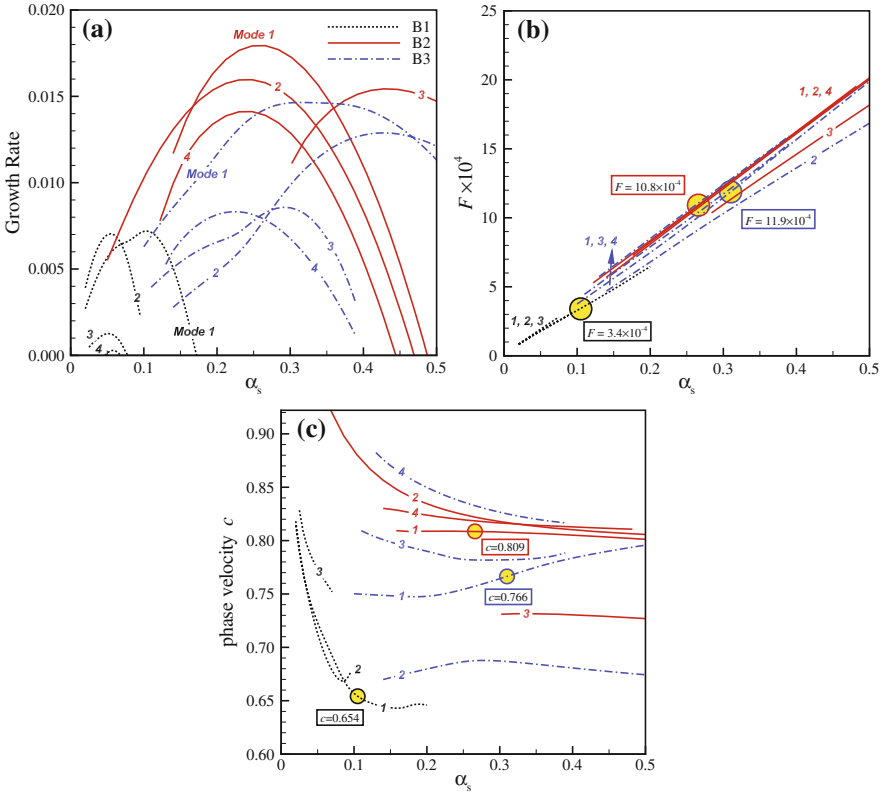


**Fig. 4.10** **a** Growth rate of the subharmonic secondary disturbances as a function of the streamwise wavenumber $\alpha_s$ at $Re = 700$. Case M1-S-B1, M1-S-B2 and M1-S-B3 are shown. Say, $Ma = 1.5$, $\gamma_i = 0.5$, B=0.5, 1.0 and $2.0 \times 10^{-3}$. The labels "Mode 1, 2, ... " indicate the ranking of maximum growth rate. The most amplified four modes (if exist) are provided. **b** Dimensionless frequency $F$. The dominant frequencies $F = 3.4,\ 10.8$ and $11.9 \times 10^{-4}$ (belong to the largest growth rates) are circled for the three cases. **c** Phase velocity $c$ of the corresponding disturbances. The dominant phase velocity $c = 0.654,\ 0.809$ and 0.766 are circled

The subharmonic and the detuned secondary instabilities of Görtler vortices in high-speed flows also require better understanding. To the authors' knowledge, this topic has not been well investigated. Here, we focus on the effect of the Floquet parameter $\gamma$. The streamwise location is fixed at $Re = 700$.

Considering the subharmonic type with $\gamma_i/\beta = 0.5$, the perturbations experience a 180° phase change between the *mushrooms*. The growth rate of disturbances for case M1-S-B1, M1-S-B2 and M1-S-B3 are given in Fig. 4.10a as a function of the streamwise wavenumber $\alpha_s$. The curves are similar to the fundamental counterparts shown in Fig. 4.6a. The sinuous mode type II appears as mode 3 in M1-S-B2 and mode 2 in M1-S-B3. The growth rate for each of the mode is in the same amplitude as its fundamental counterpart. Concerning the peak growth rate of the most dangerous

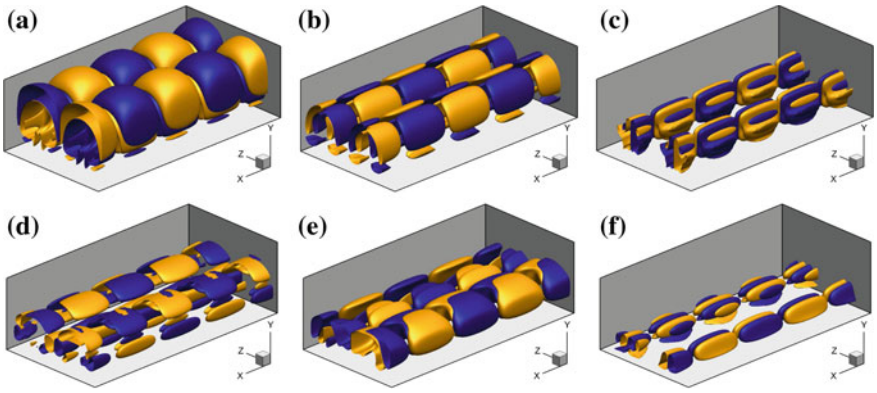


**Fig. 4.11** Contour surfaces of the normalized streamwise velocity perturbations $u_s$ at $Ma = 1.5$, $Re = 700$. The surfaces colored yellow and blue indicate $u_s = 0.1$ and $-0.1$, respectively. One period in spanwise and two periods in streamwise directions are shown. **a** Subharmonic varicose mode, $B = 1.0 \times 10^{-3}$, $\alpha_s = 0.266$; **b** Subharmonic sinuous mode type I, $B = 1.0 \times 10^{-3}$, $\alpha_s = 0.248$; **c** Subharmonic sinuous mode type II, $B = 1.0 \times 10^{-3}$, $\alpha_s = 0.428$; **d** Detuned varicose mode, $B = 2.0 \times 10^{-3}$, $\gamma_i = 0.24$, $\alpha_s = 0.320$; **e** Detuned sinuous mode type I, $B = 2.0 \times 10^{-3}$, $\gamma_i = 0.24$, $\alpha_s = 0.320$; **f** Detuned sinuous mode type II, $B = 2.0 \times 10^{-3}$, $\gamma_i = 0.24$, $\alpha_s = 0.320$

mode, it can be smaller (case M1-S-B3) or larger (case M1-S-B2) compared with the fundamental case. Therefore, the subharmonic secondary instability can have the largest growth rate leading to flow transition. The frequency and phase velocity shown in Fig. 4.10b, c are quite similar to the fundamental case. The sinuous mode type II again stands out. A slight difference in the most dangerous frequency and velocity is observed in Fig. 4.10b, c.

A global view of the normalized disturbance $u_s$ (under subharmonic and detuned conditions) of the varicose mode, sinuous mode type I and sinuous mode type II is provided in Fig. 4.11. Contour surfaces corresponding to $u_s = \pm 0.1$ are colored blue and yellow respectively. The plot includes one period in the spanwise and two in the streamwise directions. The disturbance repeats itself in both directions. The detuned mode exhibit a phase change of angle $\psi$ ($0° < \psi < 180°$, depending on the Floquet parameter $\gamma$) from its neighboring disturbances. In addition to modifications to the steady state (*mushrooms* or *bells*), subharmonic and detuned disturbances result in a disruption of the original spanwise periodicity of the primary state.

Figure 4.12a shows the growth rate of secondary disturbances as a function of the Floquet parameter $\gamma$ for M1-D-B1, M1-D-B2 and M1-D-B3. The streamwise wavenumber $\alpha_s$ is specified to the value at which the fundamental disturbance has the maximum growth rate. When $\gamma_i/\beta$ increases from 0 all the way to 0.5, the growth rate of the mode increases or decreases monotonically. Some modes (*e.g.* the mode 2 in M1-D-B3) are actually insensitive to the Floquet parameter. Detuned modes, hence, are not dominating in these cases. Computations have been carried out for all the five Mach numbers and three wavenumbers in Table 4.1. We demonstrate that detuned modes generally have smaller growth rates compared with their fundamental or

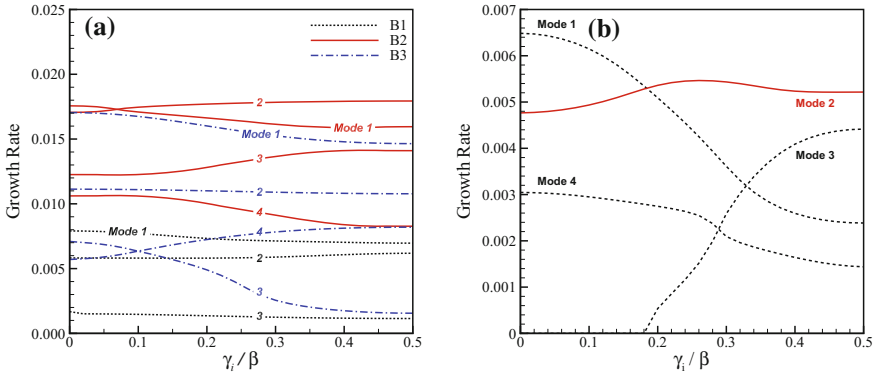


**Fig. 4.12** Growth rate of the secondary disturbances versus the Floquet parameter $\gamma$ at $Re = 700$. "Mode 1, 2···" are named after the maximum growth rate of the fundamental disturbances (see Fig. 4.6a). **a** case M1-D-B1, M1-D-B2 and M1-D-B3. **b** case M2-D-B1.Growth rate of the secondary disturbances versus the Floquet parameter $\gamma$ at $Re = 700$. "Mode 1, 2···" are named after the maximum growth rate of the fundamental disturbances (see Fig. 4.6a). **a** case M1-D-B1, M1-D-B2 and M1-D-B3. **b** case M2-D-B1

subharmonic counterparts except case M2-D-B1 ($Ma = 3.0$) and M3-D-B1 ($Ma = 4.5$). The case M2-D-B1 is highlighted in Fig. 4.12b. Again, the modes are named after their maximum growth rate as mode 1, mode 2... The 2nd amplified mode reaches its maximum growth at a detuned state. This phenomenon was not observed in the incompressible case. Within the cases studied in this chapter, these two exceptions are both the second amplified mode which would not create a primary influence on the transition process.

In the above analysis, we have shown that Floquet parameter can indeed alter the growth rate of disturbances. This is true for both the streak type flows [3, 12, 20] and the secondary instability of T-S waves [21] for which the growth rate of subharmonic mode can have a distinct difference, larger or smaller than the fundamental type. One notable exception is the crossflow vortices. It was shown that the detuned eigensolution can be regarded as a superposition of the eigenfunctions with identical eigenvalues [22, 23], thus, having the same growth rate. This is also validated in a recent Floquet analysis [24].

## 4.3 Conclusions

The spatial development and fundamental, subharmonic and detuned secondary instabilities of Görtler vortices in high-speed boundary layer flows are numerically investigated in this chapter. Five groups of $Ma$ numbers ($Ma = 0.015, Ma = 1.5, 3.0$, 4.5 and 6.0) are studied to illustrate the compressibility effect. The Görtler vortices

with three groups of representative global spanwise wavenumbers ($B = 0.5$, 1.0 and $2.0 \times 10^{-3}$) are considered to reveal the effect of primary spanwise wavelength.

The development of Görtler vortices acts to strengthen the boundary layer streaks regardless of the Mach number. In the current study, the streak amplitude $A(u)$ keeps growing downstream (before the right-branch regime is reached). The sinuous mode type I becomes unstable first, followed by the varicose mode and then the sinuous mode type II.

Mach number affects Görtler vortices in two aspects. (1) The growth rate of primary Görtler mode decreases with Mach number. The streaks are thus weakened. (2) Increase in $Ma$ gives rise to the trapped-layer mode (mode T) for the primary instability. This mode has its disturbances detached from the wall. As a result of the above changes, conventional *mushroom* structures are replaced by *bell*-shaped structures leaving the near-wall region an unperturbed area. The difference in the primary instability leads to a deserved and remarkable change on the secondary instability. In subsonic and moderate supersonic flows, varicose and sinuous (type I and type II) modes can both be responsible for the transition process. The sinuous mode type II, whose disturbances concentrate near the *stem* of the *mushroom*, is demonstrated to have the largest growth rate when the streak amplitude is large. However, it is missing in existing studies. The relationship between the dominance of sinuous or varicose modes and the primary wavelength in incompressible flow [3] is no longer valid in hypersonic flows. The sinuous mode becomes the most dangerous regardless of the spanwise wavelength when $Ma > 3$. The effect of the Floquet parameter $\gamma$ on the growth rate of the secondary instability is clarified. The subharmonic type can become the most dangerous mode, *e.g.* in the case M2-S-B3. The detuned type, however, is not responsible for the flow transition though in case M2-D-B1 and M3-D-B1, one of the sub-dominant modes reaches its maximum growth rate under detuned state.

The boundary layer transition promoted with concave curvature (Görtler instability), roughness elements or the FST (Klebanoff mode) can follow a similar path utilizing the *lift up* mechanism. As a matter of fact, streamwise curvature acts as an unsophisticated influence, providing a chance to conduct this comprehensive study. The introduction of roughness elements not only brings in discernable wakes which support sinuous and varicose modes but also creates new mechanisms relating to receptivity, flow separation and shock wave boundary layer interactions. All these phenomena, of course, are closely related to the geometry of the roughness elements. In moderate supersonic flows [19, 25], the varicose mode is demonstrated to be the most dangerous in the wake of diamond ($Ma = 3.5$) and square ($Ma = 2.5$) shape roughness elements. In a subsequent study by [26], the Mach number is increased to 5.9 and sinuous perturbations become dominant. In the study of [27, 28], the Mach number is 4.8 and 3.5 respectively, both two types of perturbations emerge. In brief, the various parameters, $Re$, $Ma$, shape, hight and arrangement of the roughness elements, on the roughness induced transition are far from fully clear. The role of sinuous mode type II in this flow also needs clarification. Future studies is thus required on this topic.

Recalling the discussions in Sect. 4.1, with an initial amplitude of $A(u) = 2 \times 10^{-3}$ which is typically the order of practical environment, it takes a long distance for the streaks to be *matured* for the secondary instabilities to set in (see Fig. 4.4). Increase in the $Ma$ number hampers the development of the streaks further and thus may cause failure in flow transition. In some practical situations, for example, before the entrance of the scramjet combustor, this flow behavior is undesirable. An open question remains as how to achieve optimal control of hypersonic flow transition based on the secondary instability of Görtler vortices.

## References


1. Swearingen, J.D., Blackwelder, R.F.: The growth and breakdown of streamwise vortices in the presence of a wall. J. Fluid Mech. **182**, 255–290 (1987). doi:10.1017/S0022112087002337
2. Mitsudharmadi, H., Winoto, S.H., Shah, D.A.: Secondary instability in forced wavelength görtler vortices. Phys. Fluids **17**(7), 074104 (2005). doi:10.1063/1.1941367, http://scitation.aip.org/content/aip/journal/pof2/17/7/10.1063/1.1941367
3. Li, F., Malik, M.R.: Fundamental and subharmonic secondary instabilities of Görtler vortices. J. Fluid Mech. **297**, 77–100 (1995). doi:10.1017/S0022112095003016
4. Ren, J., Fu, S.: Study of the discrete spectrum in a Mach 4.5 Görtler flow. Flow Turbul. Combust. **94**(2), 339–357 (2015). doi:10.1007/s10494-014-9575-z
5. Wu, X., Zhao, D., Luo, J.: Excitation of steady and unsteady Görtler vortices by free-stream vortical disturbances. J. Fluid Mech. **682**, 66–100 (2011). doi:10.1017/jfm.2011.224
6. Dando, A.H., Seddougui, S.O.: The compressible Görtler problem in two-dimensional boundary layers. IMA J. Appl. Math. **51**(1), 27–67 (1993). doi:10.1093/imamat/51.1.27
7. Ren, J., Fu, S.: Competition of the multiple Görtler modes in hypersonic boundary layer flows. Sci. China Phys. Mech. Astron. **57**(6), 1178–1193 (2014). doi:10.1007/s11433-014-5454-9
8. Lee, K., Liu, J.T.C.: On the growth of mushroomlike structures in nonlinear spatially developing Goertler vortex flow. Phys. Fluids A Fluid Dyn. **4**(1), 95–103 (1992). doi:10.1063/1.858506
9. Girgis, I.G., Liu, J.T.C.: Nonlinear mechanics of wavy instability of steady longitudinal vortices and its effect on skin friction rise in boundary layer flow. Phys. Fluids **18**(2), 024,102 (2006). doi:10.1063/1.2158430
10. Ricco, P., Wu, X.: Response of a compressible laminar boundary layer to free-stream vortical disturbances. J. Fluid Mech. **587**, 97–138 (2007). doi:10.1017/S0022112007007070, http://journals.cambridge.org/article_S0022112007007070
11. Li, F., Choudhari, M., Chang, C.L., Wu, M., Greene, P.: Development and breakdown of Görtler vortices in high speed boundary layers. In: 50th Aerospace Sciences Meeting Including the New Horizons Forum and Aerospace Exposition (2010), AIAA-2010-0705. doi:10.2514/6.2010-705
12. Andersson, P., Brandt, L., Bottaro, A., Henningson, D.S.: On the breakdown of boundary layer streaks. J. Fluid Mech. **428**, 29–60 (2001). doi:10.1017/S0022112000002421, http://journals.cambridge.org/article_S0022112000002421
13. Bottaro, A., Klingmann, B.: On the linear breakdown of Görtler vortices. Eur. J. Mech. B Fluids **15**(3), 301–330 (1996)
14. Mack, L.M.: Linear stability theory and the problem of supersonic boundary-layer transition. AIAA J. **13**(3), 278–289 (1975)
15. Mack, L.M.: Boundary-layer linear stability theory. AGARD Report 709, Special Course on Stability and Transition of Laminar Flows (1984)
16. Federov, A., Tumin, A.: High-speed boundary-layer instability: old terminology and a new framework. AIAA J. **49**(8), 1647–1657 (2011)

17. Ma, Y., Zhong, X.: Receptivity of a supersonic boundary layer over a flat plate. part 1. wave structures and interactions. J. Fluid Mech. **488**, 31–78 (2003). doi:10.1017/S0022112003004786, http://journals.cambridge.org/article_S0022112003004786
18. Ren, J., Fu, S.: Floquet analysis of fundamental, subharmonic and detuned secondary instabilities of Görtler vortices. Sci. China Phys. Mech. Astron. **57**(3), 555–561 (2014). doi:10.1007/s11433-014-5396-2
19. De Tullio, N., Paredes, P., Sandham, N.D., Theofilis, V.: Laminar-turbulent transition induced by a discrete roughness element in a supersonic boundary layer. J. Fluid Mech. **735**, 613–646 (2013). doi:10.1017/jfm.2013.520
20. Ricco, P., Luo, J., Wu, X.: Evolution and instability of unsteady nonlinear streaks generated by free-stream vortical disturbances. J. Fluid Mech. **677**, 1–38 (2011). doi:10.1017/jfm.2011.41, http://journals.cambridge.org/article_S0022112011000413
21. Herbert, T.: Secondary instability of boundary layers. Ann. Rev. Fluid Mech. **20**(1), 487–526 (1988). doi:10.1146/annurev.fl.20.010188.002415
22. Wassermann, P., Kloker, M.: Transition mechanisms in a three-dimensional boundary-layer flow with pressure-gradient changeover. J. Fluid Mech. **530**, 265–293 (2005). doi:10.1017/S0022112005003708, http://journals.cambridge.org/article_S0022112005003708
23. Bonfigli, G., Kloker, M.: Secondary instability of crossflow vortices: validation of the stability theory by direct numerical simulation. J. Fluid Mech. **583**, 229–272 (2007). doi:10.1017/S0022112007006179, http://journals.cambridge.org/article_S0022112007006179
24. Xu, G., Liu, G., Jiang, X.: The nonlinear instability of the supersonic crossflow vortex. In: 44th AIAA Fluid Dynamics Conference, AIAA-2014-2637 (2014)
25. Choudhari, M., Li, F., Chang, C.L., Edwards, J., Kegerise, M., King, R.: Laminar-turbulent transition behind discrete roughness elements in a high-speed boundary layer. In: 48th AIAA Aerospace Sciences Meeting Including the New Horizons Forum and Aerospace Exposition, AIAA-2010-1575 (2010)
26. Choudhari, M., Li, F., Chang, C.L., Norris, A., Edwards, J.: Wake instabilities behind discrete roughness elements in high speed boundary layers. In: 51st AIAA Aerospace Sciences Meeting including the New Horizons Forum and Aerospace Exposition, AIAA-2013-0081 (2013)
27. Groskopf, G., Kloker, M., Marxen, O.: Bi-global crossplane stability analysis of high-speed boundary-layer flows with discrete roughness. In: Schlatter, P., Henningson, D.S. (eds.) Seventh IUTAM Symposium on Laminar-Turbulent Transition, IUTAM Bookseries, vol. 18, pp. 171–176. Springer, Netherlands (2010). doi:10.1007/978-90-481-3723-7_26
28. Kegerise, M.A., King, R.A., Owens, L.R., Choudhari, M.M., Norris, A.T., Li, F., Chang, C.L.: An experimental and numerical study of roughness-induced instabilities in a mach 3.5 boundary layer. In: RTO AVT-200 RSM-030 Specialists' Meeting on Hypersonic Laminar-Turbulent Transition, NF1676L-14423 (2012)

# Chapter 5
# Stabilization of the Hypersonic Boundary Layer

## 5.1 Perturbations in Hypersonic Boundary Layers

In hypersonic boundary layers, the Mack's second mode [1] becomes the dominant disturbances. Employing the terminology suggested by [2], this mode becomes unstable when the fast mode (mode F) and slow mode (mode S) synchronize with each other [3, 4]. The second mode can be mode F or mode S depending on the branching of the discrete spectrum [5]. In fact, the amplification of the second mode is related to both mode F and mode S, *i.e.* a *double-mode* activity.

The neutral curves of the 2-D disturbance in $Re - \omega$ plane for $Ma = 4.5$ and 6.0 are shown in Fig. 5.1. In the range of the parameters considered here, the unstable regions of the first and second modes are well separated for $Ma = 4.5$ while they overlap for $Ma = 6.0$. The current study considers the perturbations with frequencies $F_1 = 2.2 \times 10^{-4}$, $F_2 = 1.2 \times 10^{-4}$ and $F_3 = 0.6 \times 10^{-4}$ where $F = \omega/Re$. The parameters of the four cases studied here are listed in Table 5.1. Perturbations considered in Case 1 and 2 are the second and first modes, respectively. Note that in the $Ma = 6.0$ flow (Case 3 and 4) perturbations with $F_2$ and $F_3$ manifest both the first and second modes. All the cases share the following parameters: stagnation temperature $T_s^* = 333K$, Prandtl number $Pr = 0.7$, Reynolds number $Re_0 = 300$. Adiabatic wall boundary condition is specified for the mean flow.

In Fig. 5.2, the evolution of the discrete spectrum at $Ma = 4.5$ and 6.0 for all the three frequencies are presented. At low Reynolds numbers, the mode S and mode F synchronize with the slow ($c_r = 1 - 1/Ma$) and fast acoustic waves ($c_r = 1 + 1/Ma$), respectively. Further downstream, the phase velocity of mode S increases and mode S may become unstable once passing through branch-I of the neutral curve of the first mode. Accordingly, the phase velocity of mode F decreases. The synchronization between the mode F and the entropy/vorticity wave takes place when $c_r = 1$[6]. Finally, the synchronization between mode S and mode F starts when they have the same phase velocity. This process remains for a range of $Re$ and is responsible for the instability of the second mode as well as the branching of the spectrum.



J. Ren, *Secondary Instabilities of Görtler Vortices in High-Speed Boundary Layers*, Springer Theses, https://doi.org/10.1007/978-981-10-6832-4_5

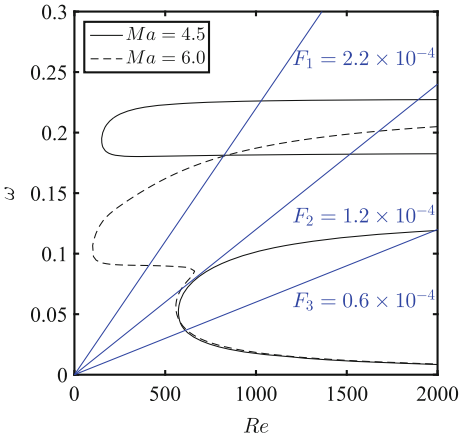


**Fig. 5.1** Neutral curves of two-dimensional disturbances in hypersonic boundary layers with $Ma = 4.5$ and 6.0

**Table 5.1** The flow and disturbance parameters for 2-D perturbations studied in the current work

| Flow case | Flow parameters | Perturbations |
|---|---|---|
| Case 1 | $Ma = 4.5$, $F = F_1$ | Second mode |
| Case 2 | $Ma = 4.5$, $F = F_3$ | First mode |
| Case 3 | $Ma = 6.0$, $F = F_2$ | First & second mode |
| Case 4 | $Ma = 6.0$, $F = F_3$ | First & second mode |

## 5.2 The Streaks

As introduced in Sect. 1.3, the Görtler modes or Klebanoff modes are natural and straightforward streak generators. They both manifest as counter-rotating streamwise vortices and give rise to the streaks through *lift-up* mechanism [7–9]. The primary differences between the two are as follows: (i) The Görtler modes are non-modal in small *Re* regime and approach exponential modal growth when the *Re* is asymptotically large [10]. Whereas the Klebanoff modes are fundamentally non-modal and can be recovered with a linear combination of the eigenmodes, or with the adjoint equations iteratively accounting for the non-parallel effects. (ii) The Görtler modes are driven by the centrifugal instability and can keep growing before entering the right branch regime [10]. On the other hand, the Klebanoff modes would be amplified in a rather limited range and therefore their growth is termed as *transient growth*.

The optimal disturbances can be computed using an eigenfunction expansion or a marching approach (including adjoint equations). In compressible boundary layers, they are described in work by Hanifi *et.al.* [11] and Tumin and Reshotko [12, 13]. The readers may refer to these papers for the formulation and relevant computational methods. Here, we utilize the local approach to compute the optimal perturbations. Figure 5.3 shows the maximum energy growth $G(x)$ versus the streamwise coordinate $x$ from local analysis. In the $Ma = 3.0$ case, shown in Fig. 5.3a, the results are

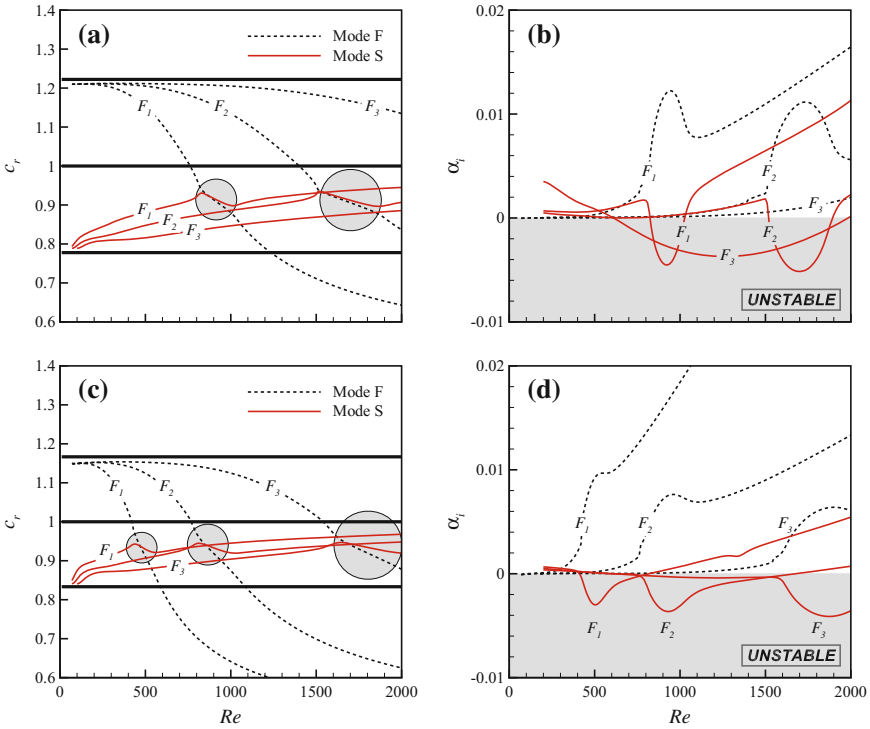


**Fig. 5.2** Evolution of the discrete spectrum of perturbations with frequency $F_1$, $F_2$ and $F_3$. Phase velocity $c_r$ and growth rate $\alpha_i$ are provided for $Ma = 4.5$ **a**, **b** and $Ma = 6.0$ **c**, **d** respectively. The regions of synchronization between mode F and mode S are circled in the diagram of the phase velocity. The thick straight line in **a**, **c** indicate the phase velocity of the fast acoustic wave ($c_r = 1 + 1/Ma$), entropy/vorticity wave ($c_r = 1$) and slow acoustic wave ($c_r = 1 - 1/Ma$) respectively. The growth rate $-\alpha_i$ of the mode S with $F = F_3$ at $Ma = 4.5$ is multiplied with 10 for a clear demonstration in **b**

compared with Tumin and Reshotko [12]. The local boundary layer is given by a self-similar solution with $Re_0 = 300$. Within the range of spanwise wavenumber considered here, $\beta = 0.2$ gives the largest energy growth $G_{max}$. This amplification ratio also depends on the streamwise coordinate of the inlet $x_0$ and outlet $x_1$. As shown in Fig. 5.3b, c, increasing the Mach number to 4.5 and 6.0 causes the transient growth of perturbation with larger wavenumber (*e.g.*$\beta > 0.1$) to decrease and fort those with smaller $\beta$ to increase. The optimal wavenumber $\beta_{opt}$ thus decreases. For the three Mach numbers considered here, streaks with $\beta = 0.1$ experience a sufficient transient growth. Therefore, they are employed in this study to stabilize the boundary layer.

When a large enough concave curvature is present, Görtler instability becomes the leading mechanism for the amplification of streaks as shown in Fig. 5.4. We define the global curvature $K$ as $K = k/Re = -\nu^*_\infty/(U^*_\infty R^*)$ where $R^*$ is the local radius

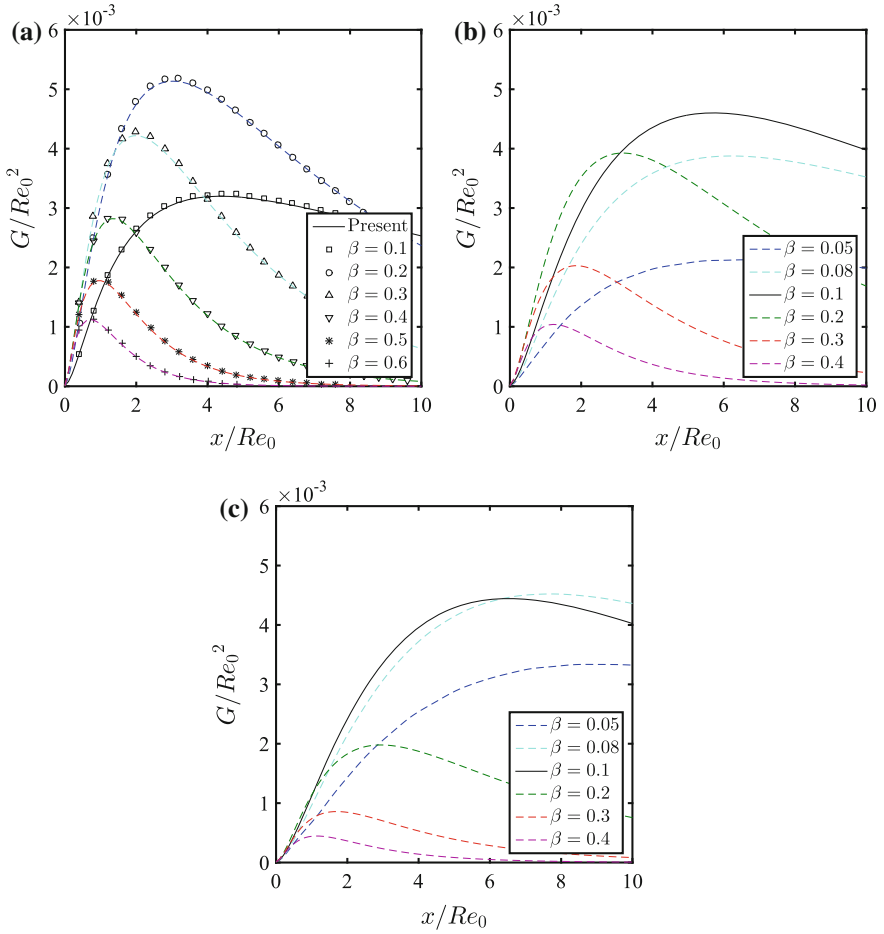


**Fig. 5.3** Maximum energy growth $G(x)$ of the optimal disturbances. $Re_0 = 300$, $T_s^* = 333K$. **a** $Ma = 3.0$, symbols denote the results from Tumin and Reshotko [12]; **b** $Ma = 4.5$; **c** $Ma = 6.0$

of curvature and $k$ is local curvature. A flat plate as well as concave plates (with three different curvatures) are compared. The spatial amplification of streaks attributes to the transient growth over a flat ($K = 0$) or weakly-curved ($K = -10^{-10}$ for example) plat. This is finally replaced with exponential growth for larger curvatures ($K = -10^{-8}$ and $-10^{-6}$). The influence of curvature on the streak profiles is shown in Fig. 5.5. Normalized streamwise velocity profiles $|\hat{u}|$ contributed by streaks are plotted uniformly-distributed within $477 \leq Re \leq 1498$. By increasing the curvature, differences become evident downstream where the Görtler modes tend to attach the wall while Klebanoff modes appear to detach. It should be noted that, a continuous transformation from Klebanoff modes to Görtler modes can be achieved by gradually

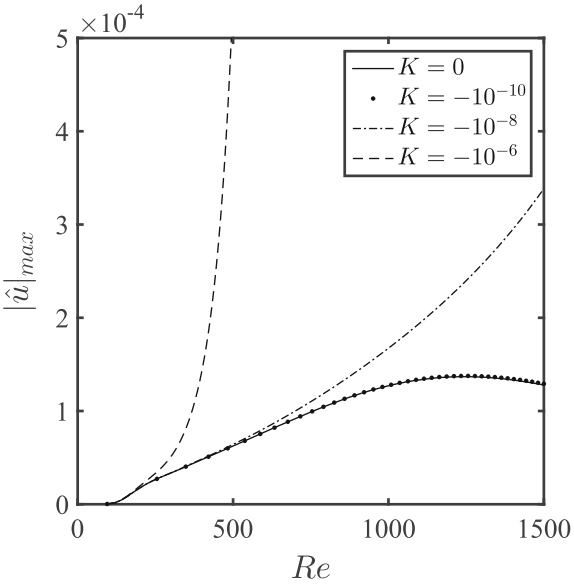


**Fig. 5.4** Effect of concave curvature on the linear spatial development of streaks: from Klebanoff-type to Görtler-type. Maximum value of streamwise velocity component $|\hat{u}|_{max}$ is plotted as a function of $Re$. $T_s^* = 333K$, $Ma = 4.5$

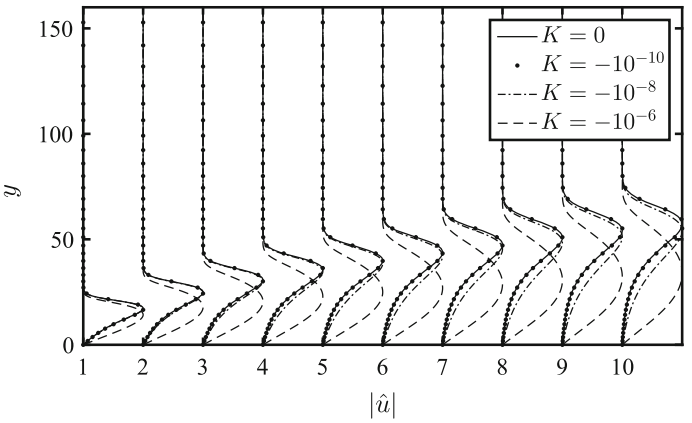


**Fig. 5.5** Profiles of the streamwise velocity component $|\hat{u}|$ distributed within $477 \leq Re \leq 1498$. They are normalized to have unit maximum value. $T_s^* = 333K$, $Ma = 4.5$

increasing the curvature. To investigate these two type of modes, we study streaks in cases with $K = 0$ and $K = -10^{-6}$. These are termed here Klebanoff-type and Görtler-type streaks, respectively.

## 5.3 The Stabilization

The steady Görtler and Klebanoff modes with spanwise wavenumber $\beta = 0.1$ are superimposed to mean flow either near the leading edge (for Klebanoff mode) or at a given Reynolds number $Re = Re_0$ (for Görtler mode). The initial T-S waves are obtained from the local stability calculation. The Klebanoff mode has been optimized for $Re = 1200$ with the inlet corresponding to $Re = Re_0 = 300$.

The stabilizing effects on the first- and second modes are investigated first at $Ma = 4.5$. The disturbances with frequencies $F_1$ and $F_3$ become unstable as the second and first mode respectively as shown in Fig. 5.2. The interaction between the streak and first/second mode is computed through the following procedure. The Klebanoff mode (mode$(0, \pm 1)$) is introduced into the boundary layer near the leading edge. Initially this perturbation is integrated linearly up to a given position. The amplitude of the Klebanoff mode is then prescribed and nonlinear calculation begins. The 2-D disturbance (mode$(1, 0)$) is then initialized at $Re = 500$ with a sufficient low amplitude thus ensuring linearity. The number of Fourier components kept in the calculation is $-12$ to 12 in the spanwise wavenumber and 0–3 in the frequency which has been tested to be sufficient to characterize the nonlinear interactions.

Four sets of streaks of different amplitudes are denoted as $K1$, $K2$, $K3$ and $K4$. The spatial development of the streaks as a function of the local Reynolds number $Re$ is presented in Fig. 5.6. The maximum amplitudes are $A(u) = 1.1\%,\ 2.2\%,\ 3.4\%$ and $4.7\%$ respectively. The amplitude is defined as:

$$A(u) = 0.5\left(\max_{y,z}(\tilde{u}) - \min_{y,z}(\tilde{u})\right) \tag{5.1}$$

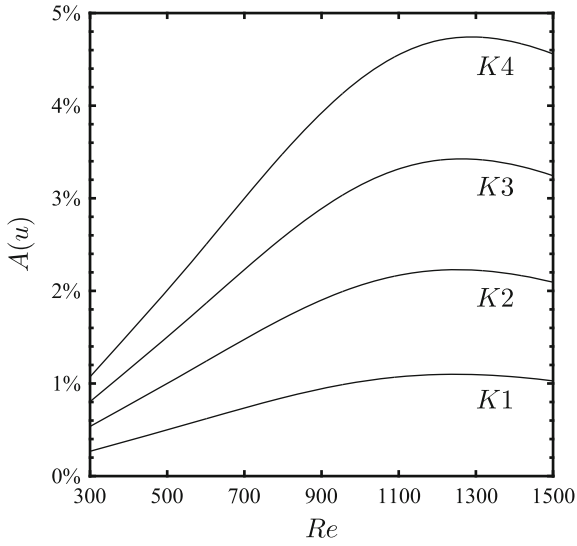


**Fig. 5.6** Spatial development of the streak amplitude. The maximum amplitudes are $A(u; K1) = 1.1\%$, $A(u; K2) = 2.2\%$, $A(u; K3) = 3.4\%$ and $A(u; K4) = 4.7\%$ respectively

The amplitude of the T-S waves measured in terms of temperature and streamwise velocity perturbations are given in Fig. 5.7. The temperature perturbation $T'$ has the largest amplitude in current hypersonic flows and can be regarded as a measure of $|q'|_{max}$. The dashed lines indicate the amplitude of the 2-D perturbations in the absence of streaks. It is therefore obvious that the streaks can stabilize both the first- and second modes. An increase of the streak amplitude resulted in a stronger stabilization. This is demonstrated as decreased amplitude of the 2-D perturbations in Fig. 5.7a, b. It is worth noting that the effect of streaks on the component of $u'$ is not always stabilizing, *e.g.*the first mode shown in Fig. 5.7b ii. Since $|u'|$ is one order of magnitude smaller than $|T'|$, the general stabilizing effect should not be influenced.

In hypersonic boundary layers, perturbations can be co-modulated by the first- and second modes, *e.g.*the $Ma = 6.0$ boundary layer (Case 3 and 4). Here, we consider perturbations with frequency $F = F2$ and $F = F3$. With the increase of $Re$, they behave as the first- and second mode successively. The second mode exerts relatively more influence on Case 3 ($F = F2$). The streaks included here are of Klebanoff-type. The maximum amplitudes are $A(u) = 0.75\%(K1),\ 1.2\%(K2),\ 1.6\%(K3)$ and $2.1\%(K4)$ in Case 3. In Case 4, they are 0.71, 1.1, 1.5 and 1.9%. The stabilization is revealed in Fig. 5.7c, d indicating that the combined first/second mode can be effectively stabilized with finite amplitude streaks as well.

When concave curvature is present, Görtler instability can play a dominant role. On concave walls, the first/second modes become more unstable as well (see also [14]). The streamwise curvature ($K = -10^{-6}$) included here stands for the most commonly investigated case and represents typical Görtler instability (see Sect. 3.2). Figure 5.8 shows the interactions between Görtler instability and the first/second mode. The dash-dotted lines (without curvature) and dashed lines (with curvature) in Fig. 5.8a, b indicate the flow without streaks. Both the first- and second modes are enhanced by concave curvature. Görtler vortices with different amplitudes are considered (G1, G2,..., G7). The initial amplitudes are prescribed as $A(u; G1) = 2 \times 10^{-11}$, $A(u; G2) = 2 \times 10^{-10}$,..., $A(u; G7) = 2 \times 10^{-5}$. In the current Görtler flow, the threshold amplitude [15] for the sinuous secondary instability is close to $A(u) = 9\%$ and is shown with a dashed line in Fig. 5.8c. The streak amplitude increases rather fast and exceeds this critical value regardless of the initial amplitude. Figure 5.8a, b shows the evolution of the second/first mode in the presence of Görtler-type streaks. The perturbations though, can be stabilized by a certain extent, they finally become more unstable due to the secondary instability of the streaks. The circle and square symbols indicate the sudden uplift of the amplitude $|T'|_{max}$ caused by secondary instabilities.

## 5.4 Mechanisms of Stabilization

In hypersonic boundary layers, both the first- and second modes (as well as combined first/second mode) can be effectively stabilized by finite amplitude streaks. The key mechanism behind lies in the modification of the base flow by the nonlinear

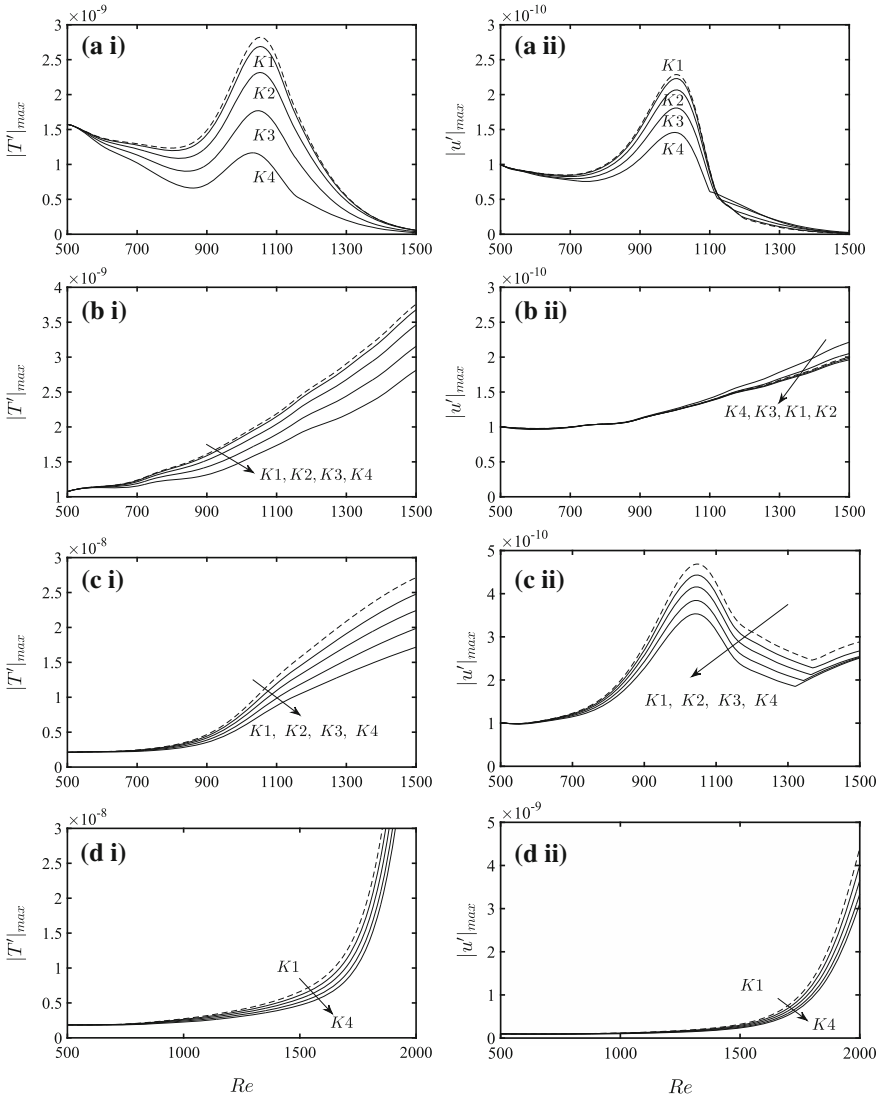


**Fig. 5.7** Evolution of the 2-D perturbations in a streaky (Klebanoff-type) flow with $Ma = 4.5$ and $Ma = 6.0$. The initial amplitude of the 2-D perturbation is $|u'|_{max} = 10^{-10}$. The amplitude of the temperature and streamwise velocity perturbations $|T'|_{max}$ and $|u'|_{max}$ are shown here. $K1$, $K2$, $K3$ and $K4$ indicate the streaks of different amplitudes. Development of the 2-D perturbations without streaks are shown with dashed lines. **a** The second mode (Case 1, $F = F1$). **b** The first mode (Case 2, $F = F3$). **c** The first/second mode (Case 3, $F = F2$). **d** The first/second mode (Case 4, $F = F2$)

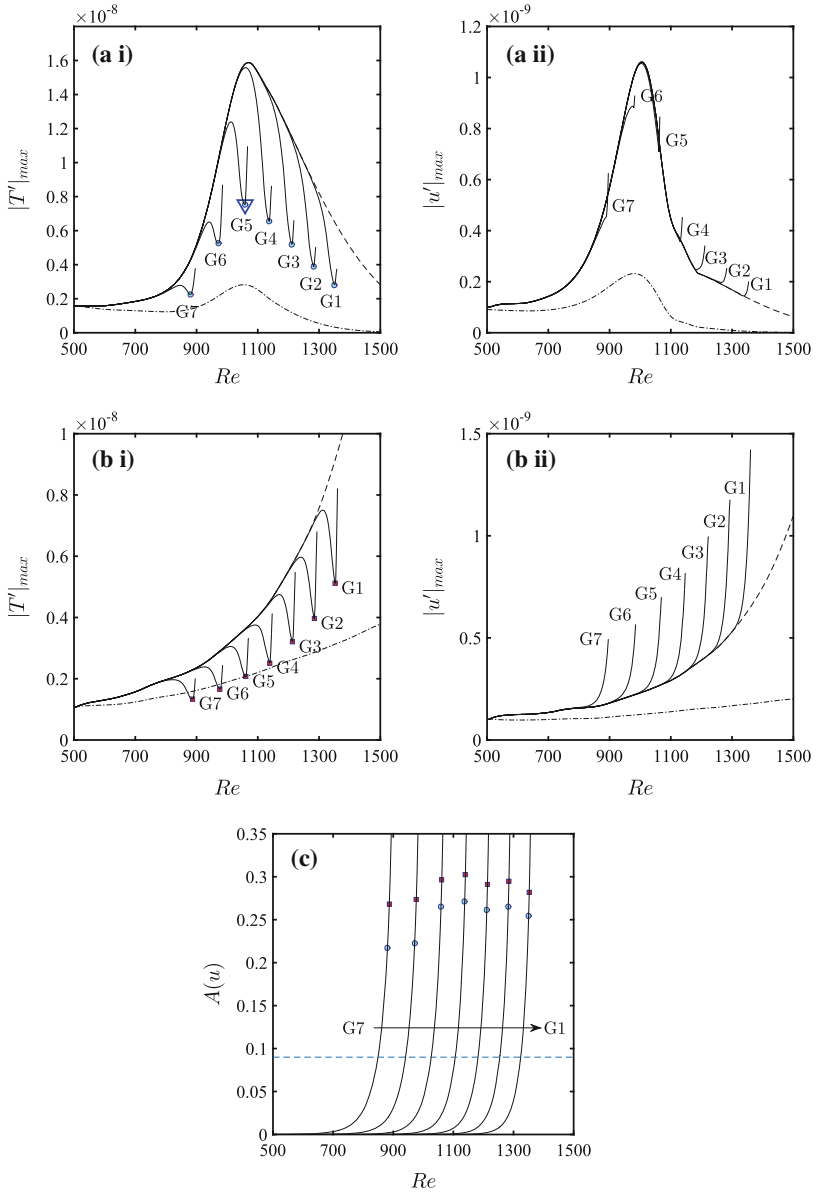


**Fig. 5.8** Evolution of the 2-D perturbations in a streaky (Görtler-type) flow with $Ma = 4.5$. The initial amplitude of the 2-D perturbation is $|u'|_{max} = 10^{-10}$. The amplitude of the temperature and streamwise velocity perturbation $|T'|_{max}$ and $|u'|_{max}$ are shown here. $G1$, $G2$,..., $G7$ indicate the streaks of different initial amplitudes. Development of the 2-D perturbations without streaks are shown with dashed lines. Dash-dotted lines correspond to the result without curvature (same as the dashed lines in Fig. 5.7a, b). The circle and square symbols indicate the onset of secondary instability. The profiles for G5 near the onset of secondary instability (denoted with a triangle) are given in Fig. 5.9c, d. **a** The second mode (Case 1, $F = F1$). **b** The first mode (Case 2, $F = F3$)

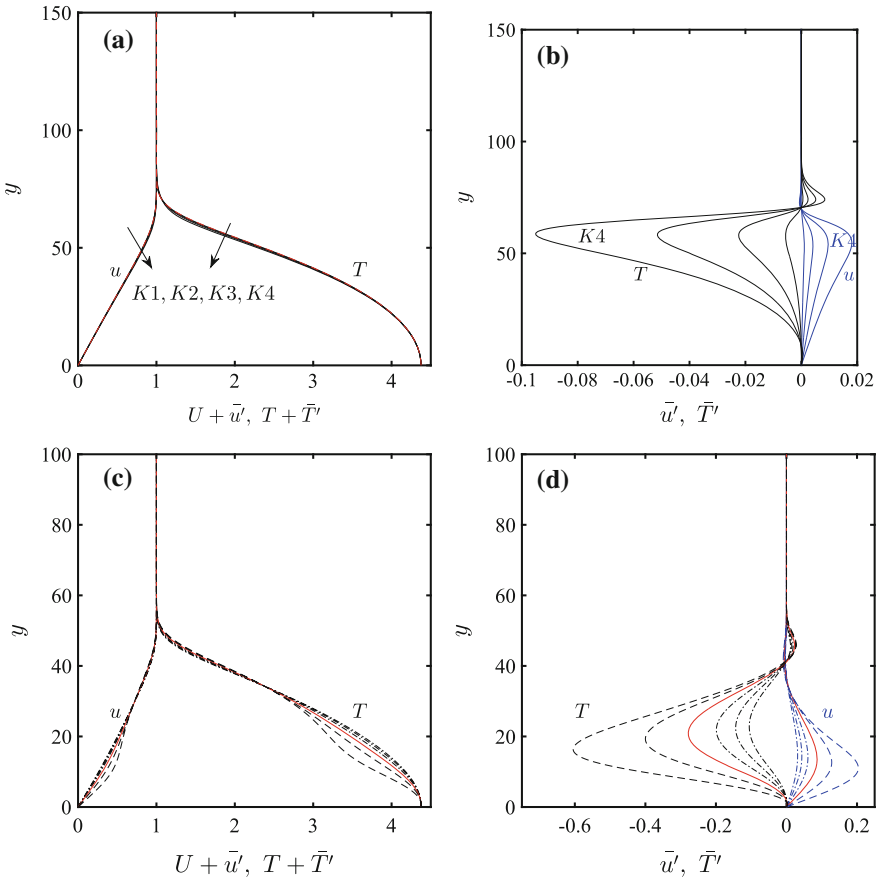


**Fig. 5.9** Spanwise averaged total (**a**, **c**) and perturbation (**b**, **d**) velocity and temperature profiles at $Ma = 4.5$ (Case 1 and 2). Klebanoff-type streaks are shown at $Re = 1500$ in **a**, **b**. The red dashed lines correspond to the boundary layer without streaks. Görtler-type streaks are shown in **c**, **d** with an initial amplitude of $A(u) = 2 \times 10^{-7}$ (G7). The red solid lines indicate the profile at $Re = 1059$ according to the triangle symbol (onset of secondary instability) in Fig. 5.8a. Inflection points arise from this position and become more obvious downstream (see dashed lines at $Re = 1064$ and 1069). Dash-dotted lines in **c**, **d** shows the profiles at $Re = 1044,\ 1049$ and 1054 which are before the onset of secondary instability

interaction with streaks. Figure 5.9 shows the spanwise averaged total (a,c) and perturbation (b,d) velocity and temperature profiles at $Ma = 4.5$. The Klebanoff-type streaks at $Re = 1500$ are shown in Fig. 5.9a, b. The base flow is modified into a fuller profile. This modification becomes more obvious when the streak amplitude is increased. In Fig. 5.9c, d similar data are presented for the Görtler-type streaks with the initial amplitude of $A(u) = 2 \times 10^{-7}$ (G5). The solid red lines indicate the profile at $Re = 1059$ which corresponds to the triangle symbol in Fig. 5.8(a). The dash-dotted lines show the profiles at $Re = 1054,\ 1049$ and 1044 where the

2D perturbations are stabilized. The dashed lines show the profiles at $Re = 1064$ and 1069 where the flow becomes secondary unstable. It is obvious that inflection points are present in both the velocity and temperature profiles. This coincide with the onset of the secondary instability.

## 5.5 Nonlinear Effects

In the study above, we have considered 2-D perturbations of small amplitudes. When their amplitudes are increased, *e.g.*to the same order of streaks, fully nonlinear interactions both in the spanwise wavenumber and frequency spaces can result in a multifold influence on the perturbations.

To examine the interaction of streaks with the nonlinear 2-D perturbations, calculations are performed for four different amplitudes of these waves. Here, the initial amplitude of streaks are the same as K4 ($A(u)_{max} = 4.7\%$) in Sec. 5.3. The results are presented in Fig. 5.10. The infinitesimal amplitude $|\hat{u}(1,0)|_{max} = 10^{-8}$ represents the linear case. In nonlinear cases, the exponential growth of mode $(1,0)$ (the perturbation of main interest) is damped due to redistribution of energy to its super-harmonics. A stronger stabilization effect is thus shown in Fig. 5.10a, c both for the first- and second mode. Comparison with the *linear* case shows that the nonlinear interactions become noticeable when the initial amplitude is rather large, *e.g.*$\hat{u}_{1,0} > 0.001$.

It is obvious here the most important interaction is between mode $(0, 1)$ & $(0, -1)$ in current streaky flows. In the fully nonlinear cases interaction of mode $(1,0)$ & $(-1,0)$ becomes dominating as well. Both interactions give rise to mode $(0,0)$ modifying the mean flow. Figure 5.10b, d shows a larger amplitude of mode $(0,0)$ with increasing the amplitude of mode $(1,0)$. The mean flow is modified to a larger degree as a result. The secondary instability will have a chance to set-in, *e.g.*in Fig. 5.10a, c where $|\hat{u}_{1,0}| = 0.01$ and 0.02 respectively. Therefore, it should be underlined that this passive control may fail with a too large amplitude of either streaks or 2-D perturbations.

Here, we investigate the mechanism on the failure of stabilization in a fully nonlinear framework. The fundamental 2-D wave has an initial amplitude of $|\hat{u}_{1,0}| = 0.005$ and the initial amplitudes of streaks correspond to K4 ($A(u)_{max} = 4.7\%$) and $A(u)_{max} = 6.0\%$ (termed K5), respectively. Both amplitudes $A(u)_{max}$ are measured with infinitesimal 2-D perturbation. The actual amplitudes are thus larger. The results are shown in Fig. 5.11 where the amplitude of modes with $m = 0, \cdots, 3$ and $n = 0, \cdots, 5$ are plotted. In the case of with K4 streak, the perturbations can still be successfully stabilized as shown in Fig. 5.11a where fully nonlinear interactions are present. With stronger streaks in Fig. 5.11b, though modes $(1, n)$ can be suppressed at some point, they finally become unstable along with their super-harmonics (*e.g.*mode $(2, n)$ and $(3, n)$) and get amplified rather quickly. A secondary instability analysis is thus given for the time-averaged mean flow at $Re = 1222$ (see dashed lines in Fig. 5.11a, b). Secondary perturbations of streamwise velocity together with the

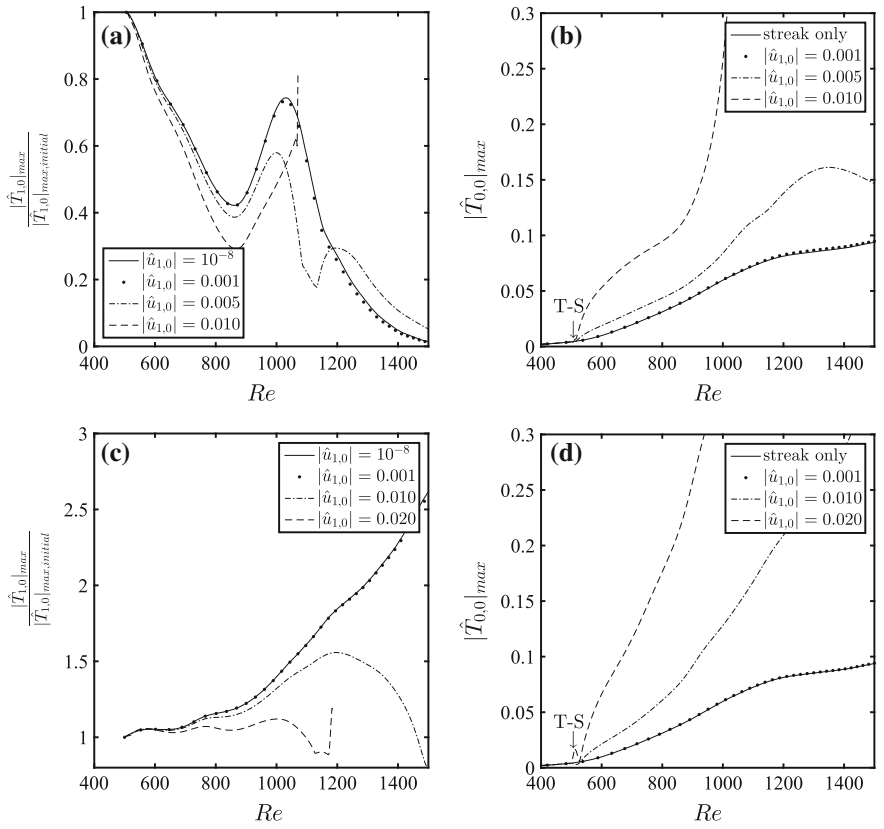


**Fig. 5.10** Nonlinear development of 2-D perturbation in streaky flat-plate flows at $Ma = 4.5$. Streak amplitude corresponds to K4 with a maximum $A(u) = 4.7\%$. **a** Amplitude of the second mode (Case 1) measured with $|\hat{T}_{1,0}|_{max}$. The initial amplitude is prescribed as $|\hat{u}_{1,0}| = 10^{-8},\ 0.001,\ 0.005$ and 0.01 respectively. The curves are scaled with the initial value at $Re = 500$. **b** Modification to the mean flow measured with $|\hat{T}_{0,0}|_{max}$ with the presence of streaks and second mode (Case 1). (**c**, **d**) Same as (**a**, **b**) but for the first mode (Case 2). The initial amplitude is $|\hat{u}_{1,0}| = 10^{-8},\ 0.001,\ 0.01$ and 0.02 respectively

mean flow are shown in Fig. 5.11c, d for the two cases. The frequency correspond to the most unstable point in Fig. 5.11e. The streak amplitudes at this position are 6.5% and 8.7% respectively. It is obvious that the secondary perturbation become unstable in both cases. They are of sinuous type and have a lower frequency compared to the 2-D perturbation. It is important to note the differences: (i) the growth rate of secondary perturbation with larger amplitude of streak is certainly larger. (ii) the unstable band of frequency in Fig. 5.11c is outside the 2-D perturbation while in (d) a larger band covers this frequency. This is responsible for the failure of stabilization in (b).

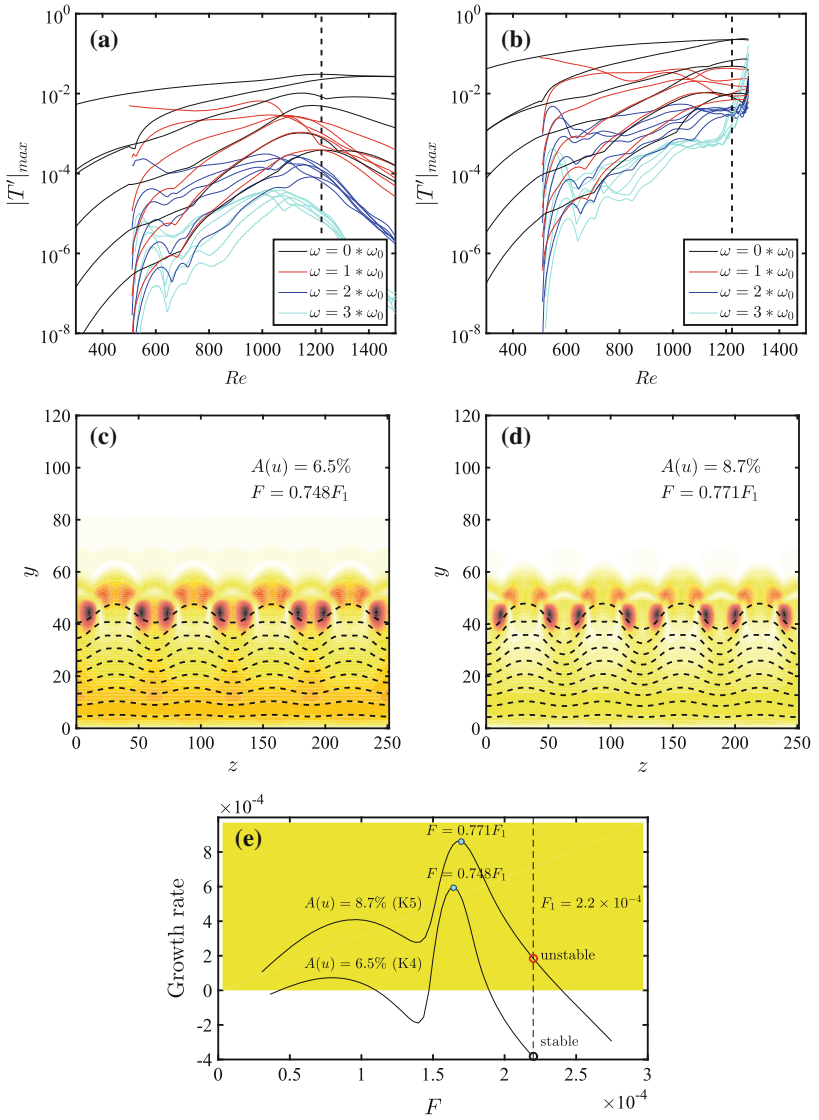


**Fig. 5.11** **a**, **b** Nonlinear development of 2-D perturbation in streaky flat-plate flows at $Ma = 4.5$. Amplitude of the mode (m,n) with $m = 0,\ 1,\ 2,\ 3$ and $n = 0,\ 1,\ 2, ..., 5$. $F = F_1$ (second mode). Initial amplitude of 2-D perturbation $|\hat{u}_{1,0}| = 0.005$. The dashed lines show the position at $Re = 1222$ where secondary instability analysis is performed. Initial streak amplitude corresponds to K4 (**a**) and K5 (**b**). **c**, **d** Secondary instability of the time-averaged streaky flows (four periods shown in spanwise). Contour lines show the streamwise velocity of the base flow. Nine equally spaced contour levels are from 0.1 to 0.9. The corresponding secondary perturbations (of the most unstable frequency) are shown with colored contours. **e** Growth rate of the secondary perturbation as a function of the dimensionless frequency $F$. The colored area shows the unstable half-plane. The solid (blue) circles indicate the most unstable frequency. The dashed line shows the frequency $F_1 = 2.2 \times 10^{-4}$ of the 2-D perturbation

## 5.6 Conclusion

From the above analysis, it can be concluded that the mechanism behind the stabilization in hypersonic boundary-layer flows is similar to that in incompressible flows, a favorable modification to the mean flow. Although the two modes are different in nature, this study shows that both the first- and second modes can be effectively stabilized with finite amplitude streaks. Klebanoff-type streaks are more interesting as they have a mild spatial growth and their amplitude is more controllable. With regard to the Görtler-type streaks, where curvature is large enough, the secondary instability becomes more inevitable due to exponential growth. The concave curvature, *per se*, destabilizes the perturbations. On the other hand, curvature can be regarded as an effective controller on streak amplitude offering further potential improvement and optimization of the control methodology.

## References

1. Mack, L.M.: Boundary-layer linear stability theory. AGARD Report 709, Special Course on Stability and Transition of Laminar Flows (1984)
2. Fedorov, A., Anatoli, T.: High-speed boundary-layer instability: old terminology and a new framework. AIAA J. **49**(8), 1647–1657 (2011)
3. Fedorov, A.: Transition and stability of high-speed boundary layers. Annu. Rev. Fluid Mech. **43**, 79–95 (2011). doi:10.1146/annurev-fluid-122109-160750
4. Zhong, X., Wang, X.: Direct numerical simulation on the receptivity, instability, and transition of hypersonic boundary layers. Annu. Rev. Fluid Mech. **44**, 527–561 (2012). doi:10.1146/annurev-fluid-120710-101208
5. Gushchin, V., Fedorov, A.: Excitation and development of unstable disturbances in a supersonic boundary layer. Fluid Dyn. **25**(3), 344–352 (1990). doi:10.1007/BF01049814
6. Fedorov, A.V., Khokhlov, A.P.: Prehistory of instability in a hypersonic boundary layer. Theor. Comput. Fluid Dyn. **14**(6), 359–375 (2001). doi:10.1007/s001620100038
7. Landahl, M.T.: Wave breakdown and turbulence. SIAM J. Appl. Math. **28**(4), 735–756 (1975). doi:10.1137/0128061
8. Ellingsen, T., Palm, E.: Stability of linear flow. Phys. Fluids (1958–1988) **18**(4), 487–488 (1975). doi:10.1063/1.861156, http://scitation.aip.org/content/aip/journal/pof1/18/4/10.1063/1.861156
9. Hultgren, L.S., Gustavsson, L.H.: Algebraic growth of disturbances in a laminar boundary layer. Phys. Fluids (1958–1988) **24**(6), 1000–1004 (1981). doi:10.1063/1.863490, http://scitation.aip.org/content/aip/journal/pof1/24/6/10.1063/1.863490
10. Hall, P.: The linear development of Görtler vortices in growing boundary layers. J. Fluid Mech. **130**, 41–58 (1983). doi:10.1017/S0022112083000968
11. Hanifi, A., Schmid, P.J., Henningson, D.S.: Transient growth in compressible boundary layer flow. Phys. Fluids **8**(3), 826–837 (1996). doi:10.1063/1.868864, http://scitation.aip.org/content/aip/journal/pof2/8/3/10.1063/1.868864
12. Tumin, A., Reshotko, E.: Spatial theory of optimal disturbances in boundary layers. Phys. Fluids **13**(7), 2097–2104 (2001)
13. Tumin, A., Reshotko, E.: Optimal disturbances in compressible boundary layers. AIAA J. **41**(12), 2357–2363 (2003)
14. Ren, J., Fu, S.: Study of the discrete spectrum in a Mach 4.5 Görtler flow. Flow Turbul. Combust. **94**(2), 339–357 (2015). doi:10.1007/s10494-014-9575-z
15. Ren, J., Fu, S.: Secondary instabilities of Görtler vortices in high-speed boundary layer flows. J. Fluid Mech. **781**, 388–421 (2015). doi:10.1017/jfm.2015.490

# Chapter 6
# Conclusions and Outlook

Görtler vortices as well as the stabilization/destabilization of 2-D disturbances in high-speed boundary layer flows are numerically investigated.

In the framework of linear stability theory, evolution of the discrete spectrum in a $Ma = 4.5$ boundary layer is studied first. Both two-dimensional (2-D) and three-dimensional (3-D) disturbances are considered with streamwise curvature effects. The concave curvature shows a destabilizing effect on the 2-D second/third mode when the fast mode (mode $F^{(1)}$, mode $F^{(2)}$...) synchronizes with the slow mode (mode S). The spectrum branching in the synchronization between the mode $F^{(2)}$ and mode S is also observed. The increase in the spanwise wavenumber(3-D disturbances), on the other hand, suppresses the synchronization between mode F and mode S and reduces the growth rate of the unstable mode. With regard to the 3-D disturbances subjecting to the concave curvature, the mode S originating from the slow acoustic wave amounts to the unsteady Görtler mode while the quasi-steady Görtler mode emanates from the continuous spectrum of the vorticity/entropy wave.

The secondary instabilities of Görtler vortices in high-speed boundary layer flows are then investigated. To uncover the compressibility effects, five *Ma* numbers, covering incompressible to hypersonic flows, at $Ma = 0.015,\ 1.5,\ 3.0,\ 4.5$ and 6.0 are specified. Görtler vortices in subsonic and moderate supersonic flows ($Ma = 0.015,\ 1.5,\ 3.0$) are governed by the conventional wall-layer mode (mode W). In hypersonic flows ($Ma = 4.5,\ 6.0$), the trapped-layer mode (mode T) becomes dominant. This difference maintains and intensifies downstream leading to different scenarios of secondary instabilities. In fact, when *Re* is large enough (*Re* is based on local boundary layer thickness), competition between mode W and mode T occurs in hypersonic cases. The linear and nonlinear development of Görtler vortices which are governed by dominant modal disturbances are investigated with direct marching of the nonlinear parabolic equations. The secondary instabilities of Görtler vortices set in when the resulting streaks are adequately developed. They are studied with Floquet theory at multiple streamwise locations. The secondary perturbations become unstable downstream following the sequence of sinuous mode type I, varicose mode and



J. Ren, *Secondary Instabilities of Görtler Vortices in High-Speed Boundary Layers*, Springer Theses, https://doi.org/10.1007/978-981-10-6832-4_6

sinuous mode type II indicating an increasing threshold amplitude. Onset conditions are determined for these modes. The above three modes each can have the largest growth rate under proper conditions. In hypersonic cases, the threshold amplitude $A(u)$ is dramatically reduced showing a great impact of the *thermal streaks*. To investigate the parametric effect of the spanwise wavenumber, three global wavenumbers ($B = 0.5,\ 1.0$ and $2.0 \times 10^{-3}$) are specified. The relationship between the dominant mode (sinuous or varicose) and the spanwise wavenumber of Görtler vortices found in incompressible flows is shown not fully applicable in high-speed cases. The sinuous mode becomes the most dangerous regardless of the spanwise wavelength when $Ma > 3.0$. The subharmonic type can be the most dangerous mode while the detuned type can be neglected although some of the sub-dominant secondary modes reach their peak growth rates under detuned states.

We make use of the streaks developed from Klebanoff (optimal perturbations) modes to stabilize the flow. The boundary-layer flows at Mach numbers 4.5 and 6.0 are studied in which both the first- and second modes are supported. When the streak amplitude is in an appropriate range, *i.e.* large enough to modulate the laminar boundary layer but low enough to not trigger secondary instability, both the first- and second modes can effectively be suppressed. On the other hand, Görtler modes can be utilized to develop a criterion on the geometry/arrangement of roughness elements to achieve flow transition—which remains to be an open question. In addition, some recommendations for future studies are provided below.

- Nonlinear adjoint equations, nonlinear receptivity
- Adjoint equations for global stability
- Interactions between the cross-flow mode and Mode F/S
- Real-gas effects in hypersonic boundary layer transition
- Stability and transition in highly non-ideal fluid flows
- Secondary instabilities of Klebanoff modes in high-speed flows
- Transition modeling considering receptivity

# Appendix A
# Expressions for the Operators in the Stability Equation

$$
\left.
\begin{aligned}
\mathbf{A}(1,1) &= \frac{1}{h_1}\frac{\partial u}{\partial x} + \frac{\partial v}{\partial y} + k\frac{v}{h_1} - im\omega \\
\mathbf{A}(1,2) &= \frac{1}{h_1}\frac{\partial \rho}{\partial x} \\
\mathbf{A}(1,3) &= \frac{\partial \rho}{\partial y} + k\frac{\rho}{h_1} \\
\mathbf{A}(1,4) &= in\beta\rho \\
\mathbf{A}(1,5) &= 0
\end{aligned}
\right\} \tag{A.1}
$$

$$
\left.
\begin{aligned}
\mathbf{A}(2,1) &= \frac{u}{h_1}\frac{\partial u}{\partial x} + v\frac{\partial u}{\partial y} + k\frac{uv}{h_1} + \frac{1}{\gamma \mathrm{Ma}^2}\frac{1}{h_1}\frac{\partial T}{\partial x} \\
\mathbf{A}(2,2) &= \frac{\rho}{h_1}\frac{\partial u}{\partial x} + k\frac{\rho v}{h_1} + \frac{k}{h_1}\frac{d\mu}{dT}\frac{\partial T}{\partial y}\frac{1}{\mathrm{Re}_0} + 27\frac{k^2}{h_1^2}\frac{\mu}{Re_0} \\
&\quad - im\omega\rho - n^2\beta^2\frac{\mu}{Re_0} \\
\mathbf{A}(2,3) &= \rho\frac{\partial u}{\partial y} + k\frac{\rho u}{h_1} - \frac{4}{3}\frac{k}{h_1^2}\frac{d\mu}{dT}\frac{\partial T}{\partial x}\frac{1}{Re_0} \\
\mathbf{A}(2,4) &= (in\beta)\frac{2}{3}\frac{1}{h_1}\frac{d\mu}{dT}\frac{\partial T}{\partial x}\frac{1}{Re_0} \\
\mathbf{A}(2,5) &= -\frac{1}{h_1}\frac{d^2\mu}{dT^2}\frac{\partial T}{\partial x}\frac{1}{Re_0}\left(\frac{4}{3}\frac{1}{h_1}\frac{\partial u}{\partial x} + \frac{4}{3}\frac{v}{h_1}k - \frac{2}{3}\frac{\partial v}{\partial y}\right) \\
&\quad - \frac{1}{h_1}\frac{d^2\mu}{dT^2}\frac{\partial T}{\partial y}\frac{1}{Re_0}\left(h_1\frac{\partial u}{\partial y} + \frac{\partial v}{\partial x} - uk\right) \\
&\quad - \frac{d\mu}{dT}\frac{1}{Re_0}\frac{k}{h_1}\left(\frac{\partial u}{\partial y} + \frac{1}{h_1}\frac{\partial v}{\partial x} - k\frac{u}{h_1}\right) - \frac{1}{h_1}\frac{d\mu}{dT}\frac{1}{Re_0}\left(h_1\frac{\partial^2 u}{\partial y^2} + \frac{\partial^2 v}{\partial x \partial y}\right) \\
&\quad + \frac{1}{\gamma Ma^2}\frac{1}{h_1}\frac{\partial \rho}{\partial x} - \frac{1}{h_1}\frac{d\mu}{dT}\frac{1}{Re_0}\left(\frac{4}{3}\frac{1}{h_1}\frac{\partial^2 u}{\partial x^2} + \frac{4}{3}\frac{\partial v}{\partial x}\frac{k}{h_1} - \frac{2}{3}\frac{\partial^2 v}{\partial x \partial y}\right)
\end{aligned}
\right\} \tag{A.2}
$$



J. Ren, *Secondary Instabilities of Görtler Vortices in High-Speed Boundary Layers*, Springer Theses, https://doi.org/10.1007/978-981-10-6832-4

$$
\left.
\begin{aligned}
\mathbf{A}(3,1) &= \frac{u}{h_1}\frac{\partial v}{\partial x} + v\frac{\partial v}{\partial y} - k\frac{uu}{h_1} + \frac{1}{\gamma Ma^2}\frac{\partial T}{\partial y} \\
\mathbf{A}(3,2) &= \frac{\rho}{h_1}\frac{\partial v}{\partial x} - 2k\rho\frac{u}{h_1} + \frac{k}{{h_1}^2}\frac{1}{Re_0}\frac{d\mu}{dT}\frac{\partial T}{\partial x} \\
\mathbf{A}(3,3) &= \rho\frac{\partial v}{\partial y} + \frac{2k^2}{{h_1}^2}\frac{\mu}{Re_0} + \frac{2}{3}\frac{1}{Re_0}\frac{d\mu}{dT}\frac{\partial T}{\partial y}\frac{k}{h_1} - \frac{2}{3}\frac{1}{Re_0}\mu\frac{k^2}{h_1^2} \\
&\quad - im\omega\rho - n^2\beta^2\frac{\mu}{Re_0} \\
\mathbf{A}(3,4) &= (in\beta)\frac{2}{3}\frac{1}{Re_0}\frac{d\mu}{dT}\frac{\partial T}{\partial y} \\
\mathbf{A}(3,5) &= \frac{1}{\gamma Ma^2}\frac{\partial \rho}{\partial y} - \frac{1}{h_1}\frac{1}{Re_0}\frac{d^2\mu}{dT^2}\frac{\partial T}{\partial x}\left(\frac{\partial u}{\partial y} + \frac{1}{h_1}\frac{\partial v}{\partial x} - k\frac{u}{h_1}\right) \\
&\quad - \frac{1}{h_1}\frac{1}{Re_0}\frac{d\mu}{dT}\left(\frac{\partial^2 u}{\partial x \partial y} + \frac{1}{h_1}\frac{\partial^2 v}{\partial x^2} - \frac{\partial u}{\partial x}\frac{k}{h_1}\right) \\
&\quad - \frac{2k}{h_1}\frac{1}{Re_0}\frac{d\mu}{dT}\left(\frac{\partial v}{\partial y} - \frac{1}{h_1}\frac{\partial u}{\partial x} - k\frac{v}{h_1}\right) \\
&\quad + \frac{1}{Re_0}\frac{d^2\mu}{dT^2}\frac{\partial T}{\partial y}\left(\frac{2}{3}\frac{1}{h_1}\frac{\partial u}{\partial x} + \frac{2k}{3}\frac{v}{h_1} - \frac{4}{3}\frac{\partial v}{\partial y}\right) \\
&\quad - \frac{1}{Re_0}\frac{d\mu}{dT}\left(-\frac{2}{3}\frac{1}{h_1}\frac{\partial^2 u}{\partial x \partial y} - \frac{2}{3}\frac{k}{h_1}\frac{\partial v}{\partial y}\right) \\
&\quad - \frac{1}{Re_0}\frac{d\mu}{dT}\left(\frac{4}{3}\frac{\partial^2 v}{\partial y^2} + \frac{2}{3}\frac{k}{{h_1}^2}\frac{\partial u}{\partial x} + \frac{2}{3}\frac{k^2 v}{h_1^2}\right)
\end{aligned}
\right\} \tag{A.3}
$$

$$
\left.
\begin{aligned}
\mathbf{A}(4,1) &= in\beta\frac{T}{\gamma Ma^2} \\
\mathbf{A}(4,2) &= -in\beta\frac{1}{h_1}\frac{d\mu}{dT}\frac{\partial T}{\partial x}\frac{1}{Re_0} \\
\mathbf{A}(4,3) &= in\beta\left(-\frac{1}{3}\mu\frac{1}{Re_0}\frac{1}{h_1}k - \frac{1}{Re_0}\frac{d\mu}{dT}\frac{\partial T}{\partial y}\right) \\
\mathbf{A}(4,4) &= -im\omega\rho - (n^2\beta^2)\frac{3}{4}\frac{\mu}{Re_0} \\
\mathbf{A}(4,5) &= in\beta\frac{1}{\gamma Ma^2}\rho \\
&\quad - in\beta\frac{\partial \mu}{\partial T}\left(-\frac{2}{3}\frac{1}{Re_0}\frac{1}{h_1}\frac{\partial u}{\partial x} - \frac{2}{3}\frac{1}{Re_0}\frac{vk}{h_1} - \frac{2}{3}\frac{1}{Re_0}\frac{\partial v}{\partial y}\right)
\end{aligned}
\right\} \tag{A.4}
$$

$$
\left.
\begin{aligned}
\mathbf{A}(5,1) &= \frac{u}{h_1}\frac{\partial T}{\partial x} + v\frac{\partial T}{\partial y} - \frac{\gamma-1}{\gamma}\frac{u}{h_1}\frac{\partial T}{\partial x} - \frac{\gamma-1}{\gamma}v\frac{\partial T}{\partial y} + im\omega\frac{\gamma-1}{\gamma}T \\
\mathbf{A}(5,2) &= \frac{\rho}{h_1}\frac{\partial T}{\partial x} - \frac{\gamma-1}{\gamma}\left(\frac{1}{h_1}\rho\frac{\partial T}{\partial x} + \frac{1}{h_1}T\frac{\partial \rho}{\partial x}\right) \\
&\quad + 2\frac{(\gamma-1)\,Ma^2}{Re_0}\mu\left(-\frac{k^2}{{h_1}^2}u + \frac{k}{{h_1}^2}\frac{\partial v}{\partial x} + \frac{\partial u}{\partial y}\frac{k}{h_1}\right) \\
\mathbf{A}(5,3) &= \rho\frac{\partial T}{\partial y} - \frac{\gamma-1}{\gamma}\left(\rho\frac{\partial T}{\partial y} + T\frac{\partial \rho}{\partial y}\right) \\
&\quad - 2\frac{(\gamma-1)Ma^2}{Re_0}\mu\left(\frac{4}{3}\frac{k}{{h_1}^2}\frac{\partial u}{\partial x} + \frac{4}{3}\frac{k^2 v}{{h_1}^2} - \frac{2}{3}\frac{k}{h_1}\frac{\partial v}{\partial y}\right) \\
\mathbf{A}(5,4) &= (in\beta)\frac{4}{3}\frac{(\gamma-1)\,Ma^2}{Re_0}\mu\left(\frac{1}{h_1}\frac{\partial u}{\partial x} + \frac{vk}{h_1} + \frac{\partial v}{\partial y}\right) \\
\mathbf{A}(5,5) &= -\frac{\gamma-1}{\gamma}\frac{u}{h_1}\frac{\partial \rho}{\partial x} - \frac{\gamma-1}{\gamma}v\frac{\partial \rho}{\partial y} - \frac{1}{Re_0\,\mathrm{Pr}}\frac{1}{{h_1}^2}\frac{d^2\kappa}{dT^2}\frac{\partial T}{\partial x}\frac{\partial T}{\partial x} \\
&\quad - \frac{1}{Re_0\,\mathrm{Pr}}\frac{1}{{h_1}^2}\frac{d\kappa}{dT}\frac{\partial^2 T}{\partial x^2} - \frac{1}{Re_0\,\mathrm{Pr}}\frac{d^2\kappa}{dT^2}\frac{\partial T}{\partial y}\frac{\partial T}{\partial y} \\
&\quad - \frac{1}{Re_0\,\mathrm{Pr}}\frac{k}{h_1}\frac{d\kappa}{dT}\frac{\partial T}{\partial y} - \frac{1}{Re_0\,\mathrm{Pr}}\frac{d\kappa}{dT}\frac{\partial^2 T}{\partial y^2} \\
&\quad - \frac{(\gamma-1)\,Ma^2}{Re_0}\frac{d\mu}{dT}\left(\frac{4}{3}\left(\frac{1}{h_1}\frac{\partial u}{\partial x} + \frac{vk}{h_1}\right)^2 + \frac{4}{3}\frac{\partial v}{\partial y}\frac{\partial v}{\partial y}\right) \\
&\quad + \frac{4}{3}\frac{(\gamma-1)\,Ma^2}{Re_0}\frac{d\mu}{dT}\left(\frac{1}{h_1}\frac{\partial u}{\partial x} + \frac{vk}{h_1}\right)\left(\frac{\partial v}{\partial y}\right) \\
&\quad - \frac{(\gamma-1)\,Ma^2}{Re_0}\frac{d\mu}{dT}\left(\frac{1}{h_1}\frac{\partial v}{\partial x} + \frac{\partial u}{\partial y} - \frac{uk}{h_1}\right)^2 \\
&\quad - im\omega\left(\frac{\rho}{\gamma}\right) - n^2\beta^2\frac{\kappa}{Re_0\,\mathrm{Pr}}
\end{aligned}
\right\} \tag{A.5}
$$

$$
\left.
\begin{aligned}
\mathbf{B}(1,1) &= v \\
\mathbf{B}(1,2) &= 0 \\
\mathbf{B}(1,3) &= \rho \\
\mathbf{B}(1,4) &= 0 \\
\mathbf{B}(1,5) &= 0
\end{aligned}
\right\} \tag{A.6}
$$

$$\left.\begin{aligned}
&\mathbf{B}(2,1) = 0\\
&\mathbf{B}(2,2) = \rho v - \frac{d\mu}{dT}\frac{\partial T}{\partial y}\frac{1}{Re_0} - \frac{\mu}{Re_0}\frac{k}{h_1}\\
&\mathbf{B}(2,3) = \frac{2}{3}\frac{d\mu}{dT}\frac{\partial T}{\partial x}\frac{1}{Re_0}\frac{1}{h_1}\\
&\mathbf{B}(2,4) = 0\\
&\mathbf{B}(2,5) = -\frac{1}{h_1}\frac{d\mu}{dT}\frac{1}{Re_0}\left(h_1\frac{\partial u}{\partial y} + \frac{\partial v}{\partial x} - uk\right)
\end{aligned}\right\} \tag{A.7}$$

$$\left.\begin{aligned}
&\mathbf{B}(3,1) = \frac{T}{\gamma Ma^2}\\
&\mathbf{B}(3,2) = -\frac{1}{h_1}\frac{1}{Re_0}\frac{d\mu}{dT}\frac{\partial T}{\partial x}\\
&\mathbf{B}(3,3) = \rho v - \frac{2k}{h_1}\frac{\mu}{Re_0} - \frac{4}{3}\frac{1}{Re_0}\frac{d\mu}{dT}\frac{\partial T}{\partial y} + \frac{2}{3}\frac{\mu}{Re_0}\frac{k}{h_1}\\
&\mathbf{B}(3,4) = -in\beta\frac{1}{3}\frac{\mu}{Re_0}\\
&\mathbf{B}(3,5) = \frac{\rho}{\gamma Ma^2} + \frac{1}{Re_0}\frac{d\mu}{dT}\left(\frac{2}{3}\frac{1}{h_1}\frac{\partial u}{\partial x} + \frac{2}{3}\frac{vk}{h_1} - \frac{4}{3}\frac{\partial v}{\partial y}\right)
\end{aligned}\right\} \tag{A.8}$$

$$\left.\begin{aligned}
&\mathbf{B}(4,1) = 0\\
&\mathbf{B}(4,2) = 0\\
&\mathbf{B}(4,3) = -in\beta\frac{1}{3}\frac{\mu}{Re_0}\\
&\mathbf{B}(4,4) = \rho v - \frac{k}{h_1}\frac{\mu}{Re_0} - \frac{1}{Re_0}\frac{d\mu}{dT}\frac{\partial T}{\partial y}\\
&\mathbf{B}(4,5) = 0
\end{aligned}\right\} \tag{A.9}$$

$$\left.\begin{aligned}
&\mathbf{B}(5,1) = -\frac{\gamma-1}{\gamma}Tv\\
&\mathbf{B}(5,2) = -2\frac{(\gamma-1)\,Ma^2}{Re_0}\mu\left(\frac{\partial u}{\partial y} + \frac{1}{h_1}\frac{\partial v}{\partial x} - \frac{uk}{h_1}\right)\\
&\mathbf{B}(5,3) = \frac{4}{3}\frac{(\gamma-1)\,Ma^2}{Re_0}\mu\left(-2\frac{\partial v}{\partial y} + \frac{1}{h_1}\frac{\partial u}{\partial x} + \frac{vk}{h_1}\right)\\
&\mathbf{B}(5,4) = 0\\
&\mathbf{B}(5,5) = \frac{\rho v}{\gamma} - \frac{2}{Re_0\,\mathrm{Pr}}\frac{d\kappa}{dT}\frac{\partial T}{\partial y} - \frac{1}{Re_0\,\mathrm{Pr}}\frac{k}{h_1}\kappa
\end{aligned}\right\} \tag{A.10}$$

$$\left.\begin{aligned}
\mathbf{C}(2,2) &= \mathcal{L}_5(4,4) = -\frac{\mu}{Re_0} \\
\mathbf{C}(3,3) &= -\frac{4}{3}\frac{\mu}{Re_0} \\
\mathbf{C}(5,5) &= -\frac{\kappa}{Re_0 \,\mathrm{Pr}}
\end{aligned}\right\} \text{only none-zeros elemetns in } \mathbf{C} \text{ are shown} \tag{A.11}$$

$$\left.\begin{aligned}
\mathbf{D}(1,1) &= \frac{u}{h_1} \\
\mathbf{D}(1,2) &= \frac{\rho}{h_1} \\
\mathbf{D}(1,3) &= 0 \\
\mathbf{D}(1,4) &= 0 \\
\mathbf{D}(1,5) &= 0
\end{aligned}\right\} \tag{A.12}$$

$$\left.\begin{aligned}
\mathbf{D}(2,1) &= \frac{1}{\gamma Ma^2}\frac{1}{h_1}T \\
\mathbf{D}(2,2) &= \rho\frac{u}{h_1} - \frac{1}{{h_1}^2}\frac{4}{3}\frac{d\mu}{dT}\frac{\partial T}{\partial x}\frac{1}{Re_0} \\
\mathbf{D}(2,3) &= -\frac{4}{3}\frac{k}{{h_1}^2}\frac{\mu}{Re_0} - \frac{1}{h_1}\frac{d\mu}{dT}\frac{\partial T}{\partial y}\frac{1}{Re_0} - \frac{k}{{h_1}^2}\frac{\mu}{Re_0} \\
\mathbf{D}(2,4) &= -(in\beta)\frac{1}{3}\frac{1}{h_1}\frac{\mu}{Re_0} \\
\mathbf{D}(2,5) &= -\frac{1}{h_1}\frac{d\mu}{dT}\frac{1}{Re_0}\left(\frac{4}{3}\frac{1}{h_1}\frac{\partial u}{\partial x} + \frac{4}{3}\frac{vk}{h_1} - \frac{2}{3}\frac{\partial v}{\partial y}\right) + \frac{1}{\gamma Ma^2}\frac{\rho}{h_1}
\end{aligned}\right\} \tag{A.13}$$

$$\left.\begin{aligned}
\mathbf{D}(3,1) &= 0 \\
\mathbf{D}(3,2) &= \frac{3}{{h_1}^2}k\frac{1}{Re_0}\mu + \frac{2}{3}\frac{1}{Re_0}\frac{d\mu}{dT}\frac{\partial T}{\partial y}\frac{1}{h_1} - \frac{2}{3}k\frac{\mu}{Re_0}\frac{1}{{h_1}^2} \\
\mathbf{D}(3,3) &= \rho\frac{u}{h_1} - \frac{1}{{h_1}^2}\frac{1}{Re_0}\frac{d\mu}{dT}\frac{\partial T}{\partial x} \\
\mathbf{D}(3,4) &= 0 \\
\mathbf{D}(3,5) &= -\frac{1}{h_1}\frac{1}{Re_0}\frac{d\mu}{dT}\left(\frac{\partial u}{\partial y} + \frac{1}{h_1}\frac{\partial v}{\partial x} - \frac{u}{h_1}k\right)
\end{aligned}\right\} \tag{A.14}$$

$$\left.\begin{aligned}
&\mathbf{D}(4,1) = 0\\
&\mathbf{D}(4,2) = -(in\beta)\frac{1}{3}\frac{1}{h_1}\frac{\mu}{Re_0}\\
&\mathbf{D}(4,3) = 0\\
&\mathbf{D}(4,4) = \rho\frac{u}{{h_1}^2} - \frac{1}{h_1}\frac{d\mu}{dT}\frac{\partial T}{\partial x}\frac{1}{Re_0}\\
&\mathbf{D}(4,5) = 0
\end{aligned}\right\} \tag{A.15}$$

$$\left.\begin{aligned}
&\mathbf{D}(5,1) = -\frac{\gamma-1}{\gamma}T\frac{u}{h_1}\\
&\mathbf{D}(5,2) = \frac{4}{3}\frac{(\gamma-1)\,Ma^2}{Re_0}\mu\left(\frac{1}{h_1}\frac{\partial v}{\partial y} - \frac{2}{{h_1}^2}\frac{\partial u}{\partial x} - \frac{2vk}{{h_1}^2}\right)\\
&\mathbf{D}(5,3) = -2\frac{(\gamma-1)\,Ma^2}{Re_0}\mu\left(\frac{1}{{h_1}^2}\frac{\partial v}{\partial x} + \frac{1}{h_1}\frac{\partial u}{\partial y} - \frac{uk}{{h_1}^2}\right)\\
&\mathbf{D}(5,4) = 0\\
&\mathbf{D}(5,5) = \frac{\rho}{\gamma}\frac{u}{h_1} - \frac{2}{\mathrm{Re}_0\,\mathrm{Pr}}\frac{1}{{h_1}^2}\frac{d\kappa}{dT}\frac{\partial T}{\partial x}
\end{aligned}\right\} \tag{A.16}$$